April 2016

Tibia Fracture Walking Boot: A Strain Controlling Device

Emily Stephanie Potter
Worcester Polytechnic Institute

Julie Anne Tevenan
Worcester Polytechnic Institute

Nathaniel Guild Sauer
Worcester Polytechnic Institute

Samuel Donlon Jacobs
Worcester Polytechnic Institute

WPI

Tibia Fracture Walking Boot: A Strain Controlling Device

A Major Qualifying Project Report
submitted to the Faculty of
WORCSETER POLYTECHNIC INSTITUTE
in partial fulfillment of the requirements for the
Degree of Bachelor of Science

Submitted By:

Samuel Jacobs (ME)

Emily Potter (ME)

Nathaniel Sauer (ME)

Julie Tevenan (BME)

Project Advisor:

Professor Brian Savilonis

Project Number: SI15

April 27, 2016

Abstract

Traditional tibia fracture healing methods take extensive amounts of time to heal and can be met with malalignments or nonunions. The group designed a non-invasive strain application device that improved upon existing fracture healing devices such as external fixators, casts, and functional braces. The design included combining an AirCast walking boot and patellar tendon bearing (PTB) brace, with the ability to create a gap beneath the heel. Three tests were used to verify the mechanical properties of the analogue bones, the strains at the fracture site produced by various forces, and the forces experienced at different locations on the foot while wearing the device. Together, the tests showed that an ideal gap size of 8 mm could reduce the control force and strain of 1700 N and 7250 microstrain by 70% to 510 N force and 2300 microstrain. Through proof of concept, the testing showed that introducing a gap size in the device correlates to a dampened force and strain at the fracture site for optimal healing conditions.

Acknowledgements

We would like to thank a few individuals for their help and support throughout this project. Thank you to Dr. Adriana Hera, Peter Hefti, and Christopher Scarpino for their guidance and willingness to assist us with our project. A special thank you to our advisor, Professor Brian Savilonis, for his continued support, motivation, and expertise over the last year.

Table of Contents

Table of Figures:

List of Tables:

Chapter 1: Introduction

Bone fractures are common injuries that can take months to heal completely. Medical trials have shown that healing time and imperfections in the healing of a fracture can be reduced by controlled force application to the fracture site. Current methods that allow micromovements at the fracture are predominantly external fixators. However, external fixators are an invasive approach to fracture healing with a surgery required to implant and remove the fixation plate and screws. External fixators also require the patient to remain immobile for months. Another option is casting the leg, which also immobilizes the patient and can lead to nonunion or malalignments. Internal fixators are another invasive procedure used to heal fractures. Problems that can arise from internal fixators include infection and allergic reactions. Internal and external fixators both put devices such as plates and screws into the bone. If these screws or plates are much stronger than the surrounding bone, they can lead to stress shielding. An alternative to external fixators, internal fixators, and casts are modified functional braces, such as patella tendon bearing (PTB) braces and walking boots, to be applicable earlier in the healing process. The functional brace would allow the person to be mobile and use the walking forces to simultaneously heal at a faster rate.

The group designed a non-invasive strain application device that improved upon existing fracture healing devices such as external fixators, casts, and functional braces. Based on research, we identified that increasing the gap size between the heel and bottom of the boot could reduce force. The group accomplished this by combining a patellar tendon bearing (PTB) brace with a traditional walking boot. We simulated the mechanical conditions associated with successful bone regeneration by a three test process: proving the mechanical properties of bone

analogues, proving the brace reduced the ground reaction force aptly, and proving the dampened force translated to the optimal strain range at the fracture site.

Chapter 2: Background

2.1 Athletic Injuries

The United States has approximately 42 million emergency room visits each year according to the Center for Disease Control (CDC) and Prevention's National Hospital Ambulatory Medical Care Survey. The CDC estimates that between 3.5 and 4.4 million of these emergency department visits result in the diagnosis of a broken bone ("National Hospital Ambulatory," 2010).

In 2012, over 1.3 million children visited the emergency room for sports related injuries. Of these, 249,000 visits were for bone fractures, second only to strains and sprains. Not surprisingly, football is the most common sport for injury, with basketball a close second. Overuse injuries are included in these statistics with football, basketball, and soccer being the most prone to overuse injuries because of the high amounts of running. In children, up to 25% of overuse injuries result in a fracture, which can lead to a lifetime of recurring injuries ("Game Changers," 2013).

Stress fractures are one of the most common injuries affecting 21% of athletes (Lassus, Tulikoura, Konttinen, Salo, & Santavirta, 2002). A study from the University of British Columbia states that stress fractures may comprise up to 10% of all sports injuries, with the tibia being the most commonly injured bone (49.1%). Stress fracture injuries are growing in frequency as the popularity of running increases. One study followed 320 athletes with stress fractures through their recovery periods, noting that the average time to diagnosis was 13.4 weeks and the average recovery time was 12.8 weeks (Matheson et al., 1987). For a professional athlete, stress fractures alone can be a career ending injury. The increasing involvement in sports

and year round training creates a need for quicker healing times in fractures. With the average diagnosis and recovery time following a fracture being currently long, a professional athlete could be out an entire season and possibly a career.

2.2 Bone Composition and Fractures

2.2.1 Bone Structure

Bone, as a component of the musculoskeletal system, performs various important functions within the body. Mechanically, bone protects, supports, and moves the body; physiologically, bone produces and stores blood cells. Vital organs, such as the brain and heart, are protected by their surrounding bones. Support and movement allow bone to react to forces placed on and by the body. The physical shape of the body is maintained because the bone and surrounding tissues oppose external forces. Bone and muscle attachments transfer forces to create body movement. (Nigg & Herzog, 2007; Seeley, Stephens, & Tate, 2006).

At the macroscopic level, bone is composed of two different structural types identified in Figure 1: cortical bone and cancellous bone. Cortical bone is known as compact bone due to the high density and low porosities of 5-10%. In comparison, cancellous or trabecular bone has a higher porosity of approximately 50-95%; trabecular bone is named after the trabeculae, plates or rods that construct the spongy structure (Doblaré, Garcia, & Gómez, 2004). There are different classifications of the bones in the body. Long bones, as shown in Figure 1, are composed of cancellous bone at the ends and cortical bone as the outside layer and in the shaft of bone. Long bones, such as the tibia, radius, and femur, use this structure to transfer forces of movement. Short bones, including the carpals and tarsals, are similar to long bones in their ability to transmit forces. On the other hand, flat bones, including the sternum, ribs, and skull bones, serve as

protection within the body. Bone structures of the flat and short bones are cancellous bone surrounded by cortical bone (Nigg et al., 2007).

Figure 1 Bone Structure Types in Femur (Willems, Langenbah, Everts, & Zentner, 2014)

At a microscopic level, the three main cells found in bones are osteoblasts, osteoclasts, and osteocytes that correspond to formation, resorption, and maintenance, respectively (Nigg et al., 2007). Osteoblasts form bone through the process of ossification, which forms the bone matrix and mineralized bone with hydroxyapatite. In contrast, osteoclasts initiate the resorption of mineralized bone, specifically damaged mineralized bone, and trigger the osteoblasts to replace the damaged bone with healthy tissues. Osteocytes are considered mature, inactive osteoblasts within the mineralized bone matrix (Seeley et al., 2006). Bone cells are discussed further in regards to their contribution to the process of bone remodeling.

2.2.2 Bone Remodeling

Bone remodeling occurs during fracture healing as well as during everyday activities; bone is constantly being remodeled and replaced. Wolff's Law states that bone alters itself in

response to the forces experienced (Lanham, 2009). Based on Wolff's Law, Turner developed three rules for how bones adapt to mechanical forces. The driving force behind bone remodeling is dynamic loading. A minimum strain is needed to start the adaptation process and an increasing strain enhances the strain stimulus. The second rule states that as the loading duration increases, the bone response becomes weaker. A longer loading does not lead to an increase in bone mass. The third rule says that bone cells become accustomed to routine loading (Figure 2), and abnormal loading stimulates remodeling of bone (Turner, 1998).

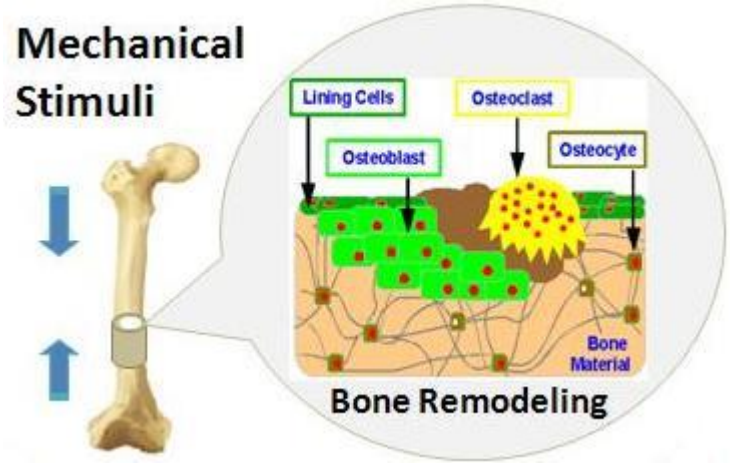

Figure 2 Bone remodeling with mechanical stimuli ("Systems Theory and Automatic Control", n.d.)

2.2.3 Fractures

Bone is expected to withstand a variety of applied and transmitted forces. However, the failure of bone to withstand cyclic loading over time or an unanticipated and excessive load leads to a fracture. The main causes of fractures vary from pathological to accidental loading (Doblaré et al., 2004). The pathological causes of bone failure focus on the bone's functional inability to withstand common loads or maintain a healthy structure. These fractures, known as pathologic, are caused by the weakening of the bone structure over time with normal movement because of increasing age or existence of disease (Doblaré et al., 2004). Osteoporosis, a common disease in

elderly, degrades the structure of bone tissue over time and leads to a higher fracture risk (Nigg et al., 2007). Bone fractures therefore depend on the bone's structural health, but can be created by a combination of other factors.

The other major cause of fractures is an undesired or accidental load applied to the bones that exceed their structural limit. Examples of accidental loads are falls, traumatic accidents, or high impacts on the body, which all transmit a high rate of force through the bone. The magnitude, rate, and direction of the force influence the bone fracture severity (Nyary et al., 2015). Overall, the application of excessive load to a bone will result in a fracture, and the fracture classifications are described below.

2.2.3.1 Fracture Classification

In general, the classification of fractures is described based on the following categories: classification of bone, location of fracture on segment, intensity of damage, and fracture pattern (Nyary et al., 2015). The AO (Arbeitsgemeinschaft für Osteosynthesefragen) classification system was created by the Association for the Study of Internal Fixation to break down the various characteristic features of long bone fractures into corresponding descriptive numbers and letter combinations (AO Foundation, 2014). The focus of this classification system and our research was on long bones. In long bones, the location of a bone fracture can occur in either the diaphysis or epiphysis. The shaft of the bone is referred to as the diaphysis, and the ends of long bones are the epiphysis, which form areas of articulation with other bones (Nigg et al., 2007). Location in the bone is an important component of classification because it influences the type of fracture.

The intensity of the fracture varies from simple to complex and indicates different levels of injury as described in the AO classification system for diaphysis long bone fractures (AO Foundation, 2014). Additional considerations in regards to assessing the amount of damage include whether the skin was penetrated and if the fracture propagated fully through the bone. An open fracture is an injury that involves the skin surrounding the fractured area being broken as a result of the injury, exposing the inner biological tissue or bone. In comparison, a closed fracture has a lower chance of contamination with the skin around the fracture remaining intact (Nyary et al., 2015). Another set of descriptive terms is complete or incomplete relating to what degree the fracture severed the bone. A complete fracture is when damage results in the original bone creating a complete break into two segments (Seeley et al., 2006). An example of a complete fracture is a comminuted fracture for bone that shatters into more than two pieces ("Tibia (Shinbone) Shaft Fractures," 2013). Incomplete fractures are those that only propagate partially through the bone. An example of this type of fracture is a hairline fracture (Seeley et al., 2006).

Using the descriptors above, fractures are classified by their overall breakage pattern. The different fracture patterns are determined by the different forces, compression, tension or shear that cause predictable patterns (Nyary et al., 2015). In Figure 3 below, the common range of shaft fracture types are illustrated.

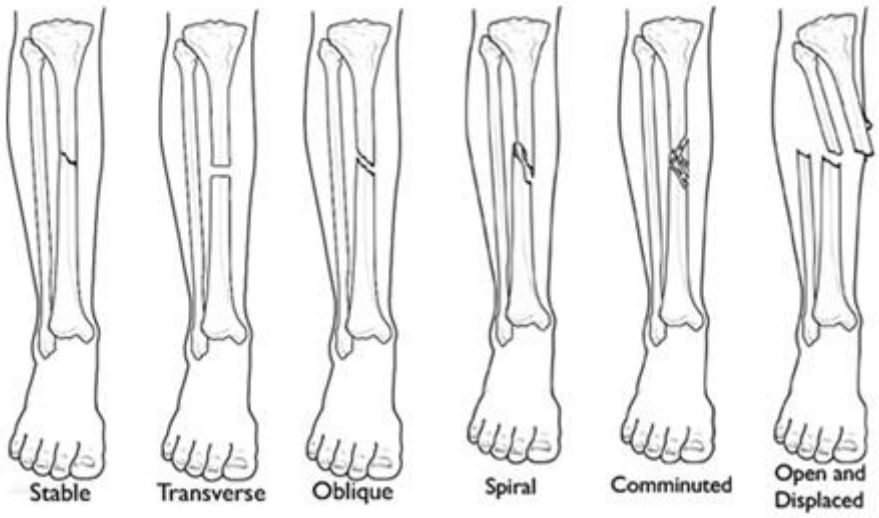

Figure 3 Common Types of Fractures ("Tibia (Shinbone) Shaft Fractures," 2013)

The simple fracture patterns of stable, transverse, oblique, and spiral are classified according to their direction and only result in two bone segments. Transverse fractures, caused by forces in tension, are horizontal fractures completely through the bone. Fractures that are slanted through the bone are oblique fractures. Spiral fractures have levels of complexity depending upon the number of segments created by the break. However, in general this classification is created by twisting forces and results in a helical pattern. Other complex types of fractures involve patterns that form more than two segments, such as a comminuted fracture, or bone segments that are no longer aligned, such as displaced fractures (AO Foundation, 2014; "Tibia (Shinbone) Shaft Fractures," 2013).

In long bones, fractures can occur at the proximal or distal ends of the bone in the epiphysis. The epiphysis fractures are described based on how the pattern through the bone impacts the area of articulation. For example, extra articular, partial articular, or complete articular are the descriptive terms based on the fracture location in relation to the articulation area of the epiphysis (AO Foundations, 2014). Overall fracture classification terminology

incorporates the information needed to understand the pattern, cause, and locations of the bone breakage, which is important in treating the injury.

2.2.4 Tibia Structure and Fractures

The tibia (Figure 4) is a major weight bearing long bone located in the lower leg and articulates with the smaller fibula ("Tibia (Shinbone) Shaft Fractures," 2013).

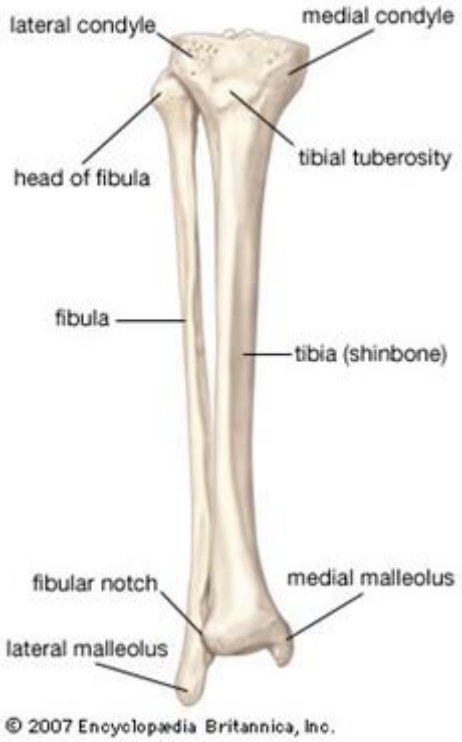

Figure 4 Lower Leg: Tibia and Fibula ("Tibia," 2015)

Fractures in the tibia are categorized based on the location of the fractures in the bone and the fracture pattern; the AO classification system identifies twenty-seven possible fracture patterns (AO Foundation, 2014). This research focuses on the fracture types located in the diaphysis of the tibia (Figure 3), specifically the simple transverse fracture through the center of the shaft. The tibial shaft for men has a cross sectional area of approximately 4.4 cm^2 compared to that of women at 3.44 cm^2 (Schiessl, Willnecker & Niemeyer, 1999).

2.3 Bone Regeneration

Bone fractures begin at the material level and occur when the load experienced by the bone is higher than the strength of the bone (Bouxsein, 2003). The composition of the extracellular matrix determines the strength of bone. The non-mineralized portion of the extracellular matrix controls the tensile strength, and the mineralized portion controls the compressive strength (Bono & Einhorn, 2003). The overall composition of bone, physical and biochemical characteristics, morphology, and amount of pre-existing damage all effect how resistant bones are to fractures (Bouxsein, 2003).

2.3.1 Bone Healing

When a bone does fracture, there are four stages of repair: hematoma formation, callus formation, callus ossification, and remodeling of bone (Figure 5).

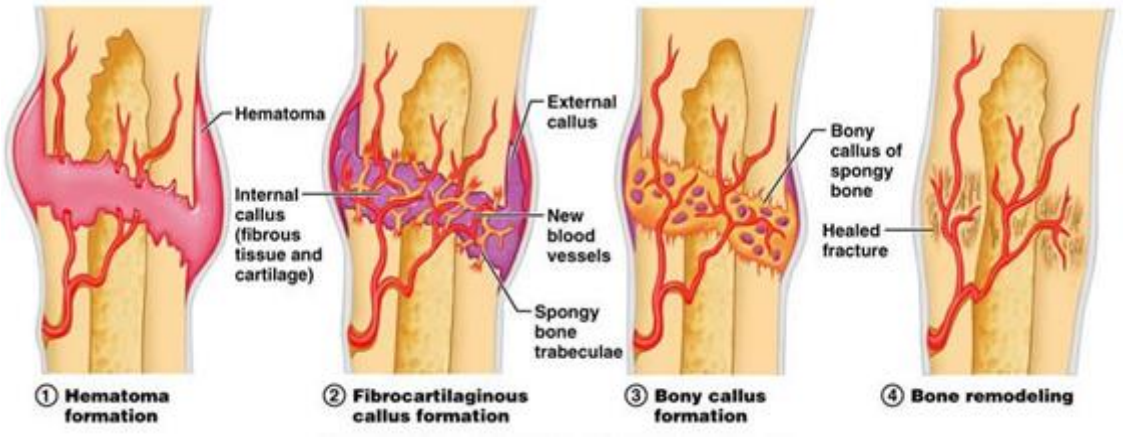

Figure 5 Four stages of bone healing ("Chapter 6: Bones and Skeletal Tissues", n.d.)

Following a fracture, blood platelets release proteins and growth factors that trigger the release of inflammatory cells (Marsh & Li, 1999). The tissue surrounding the fracture becomes inflamed, and the bone tissue adjacent to the fracture dies. Damaged blood vessels and periosteum result in a hematoma, which is a collection of blood in a confined space (Seeley et

al., 2006). Also during this phase, fibroblasts, endothelial cells, and osteoblasts are sent to the fracture (Marsh et al., 1999).

In the next stage, the internal and external callus form around the fracture. The internal callus is tissue that forms in between the broken parts of the bone. Macrophages and osteoclasts clean up the area around the fracture by cleaning it out and breaking down dead bone tissue (Seeley et al., 2006). The majority of this phase looks to form connective tissue and new capillaries (Marsh et al., 1999). Fibroblasts then form collagen to help make granulation tissue. Chondroblasts further enhance the granulation tissue by adding cartilage to the callus. Osteochondral progenitor cells from the endosteum become osteoblasts, which help produce new bone in the internal callus. The external callus forms around the outside of the fracture. Osteochondral progenitor cells from the periosteum contribute to the bone formation in the external callus. The external callus helps stabilize the fracture as the internal callus continues to form (Seeley et al., 2006).

Gradually, the external callus begins to ossify and becomes woven, cancellous bone. Osteoblasts can quickly form this woven bone. The internal callus starts forming bone through osteoblasts from the periosteum and endosteum, and this cartilage also becomes woven bone. By the end of this stage, clinically speaking, the fracture is united because woven bone replaces the callus (Seeley et al., 2006; Marsh et al., 1999).

The final stage in fracture healing is the remodeling phase. During this phase, osteoclasts begin to break down the external callus, and the internal callus becomes stronger through remodeling. The woven bone in the internal callus is replaced with compact bone (Seeley et al., 2006).

2.3.2 Bone Healing Complications

In some cases, the fracture does not heal properly. Woven bone is needed to create compact bone, but sometimes the internal callus cannot further develop into compact bone because of complications including: infection, bone movement, and the nature of the injury. This can result in nonunions and can lead to surgical treatments of the fracture (Seeley et al., 2006). Infections, more common in open fractures, occur because injured tissues are not cleared from the fracture site. The callus formed during healing can only withstand a certain amount of movement before the blood vessels and tissues are rebroken; stabilization during healing is very important. High-energy fractures sometimes have a fracture gap that is too large to self-heal, in which case surgical treatments are relied on to heal the bone (Marsh et al., 1999).

A fracture is in union when the bone can support weight-bearing activities without external support. If not healed properly, the fracture experiences malunion, delayed union, or nonunion (Figure 6) (Marsh et al., 1999). Malunion occurs when the bone heals in an abnormal position. Some deformities are functional, but others require surgery to properly fix the fracture. Based on the bone, each fracture has an estimated time needed for healing. If a bone does not heal in this time period, it could lead to a delayed union. In some cases of delayed unions, the bone does heal completely, but in others, the fracture remains as a nonunion. Delayed unions can be caused by inadequate reduction, inadequate immobilization, limited blood supply, or infection. A fracture is considered a nonunion when three months after the expected heal time

there is no further progress in the healing process (Nunamaker, Rhinelander, & Heppenstall, 1985).

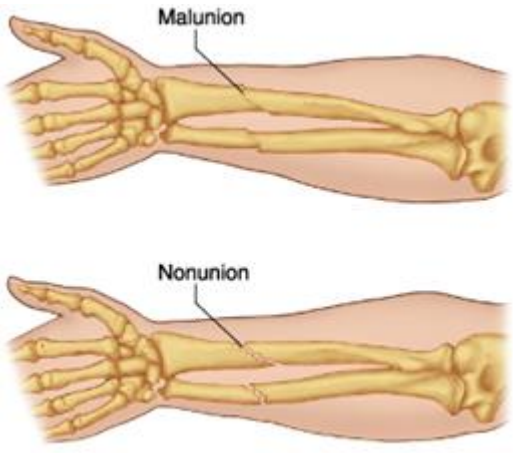

Figure 6 Complications with bone healing ("Malunion and Nonunion of Fracture," n.d.)

2.4 Current Methods of Fracture Healing

The three main methods of bone fracture healing are internal fixation, external fixation, and functional braces or casts. Different methods are more suitable for certain bones, fracture types, patient activity levels, gender, recovery time, and infection risk level. Each method has its own drawbacks and strengths.

2.4.1 External Fixators

External fixation, while by far the most tedious fracture fixation method to cope with as a patient, is currently the most effective way to heal severe fractures in an accelerated and safe manner. External bone fixation systems come in several varieties, including a unilateral, as seen in Figure 7, and circular frames. All of these designs utilize bone screws or wires to directly fixate the bone proximal and distal of the fracture. These pins run several inches out from the

body, where they are clamped to a rigid frame, which may be adjusted after an initial healing period. This frame provides increased stability around the fracture site, and can apply a compressive force to the bone. The stability may be increased by moving frame components closer to the bone.

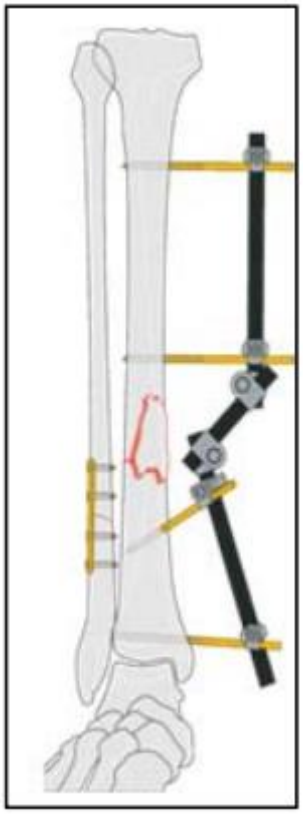

Figure 7 Unilateral external fixator frame and bone screws (Bizzarro & Rigazzoni, n.d.)

The benefits of external fixation are not as immediately evident as are drawbacks. However, external fixation excels at reducing infection rates, providing firm stabilization, allowing weight-bearing early in the healing process, and not disturbing vascular structures. Also, there is the minimized risk of a nonunion occurring during callus formation with external fixators. The decreased infection rate can be attributed to the minimized contact points between the fixator and bone along with surrounding tissue. The only contact points are the tips of the Schanz screws around the fracture site. This means that the fixator can, if applied correctly,

avoid any vasculature, tendons, or ligaments surrounding the fracture site, as well as minimizing the risk of compartment syndrome and disruption of soft tissues, osseous blood supply, and the periosteum. These frames are also useful for patients with rheumatoid arthritis, peripheral vascular disease, diabetes mellitus, and other conditions that could potentially affect the fracture site.

Drawbacks to external fixators include the need for surgeons to assemble highly precise frames, and the sites where pins enter cortical bone through the skin have a 30% chance of infection for modern fixators (Fragomen & Rozbruch, 2007). Furthermore, frames extend outwards from the body and in certain cases have a very large profile. This makes locomotion, everyday tasks, and wearing pants very difficult for many patients. This presents new risks to patients, as any impact with the fixator frame is transmitted to the bone. However, the resounding benefit is that external fixators help accelerate bone regeneration. For simple fractures, complete healing may be accomplished in as little as six weeks. A 2009 study showed that for a sample of 212 patients with external fixators, open fractures healed in an average of 25 weeks, and closed fractures healed in 21 weeks, on average (Beltsios, Savvidou, Kovanis, Alexandropoulos, & Papagelopoulos, 2009).

2.4.2 Internal Fixators

Internal fixation methods include the use of pins, plates, and nails in direct contact with bone to rejoin and stabilize at fracture locations. Before an internal fixation component can be applied, a surgeon must carefully align bone fragments to reconstruct the shape of the bone. Any misalignment in this fracture repositioning could result in a nonunion during bone healing. To hold smaller fragments in place, a surgeon utilizes wires or pins. Larger bone fragments can be

held by internal fixation screws. There exist two main types of internal fixators: intramedullary nails and plates and screws, as seen in Figure 8.

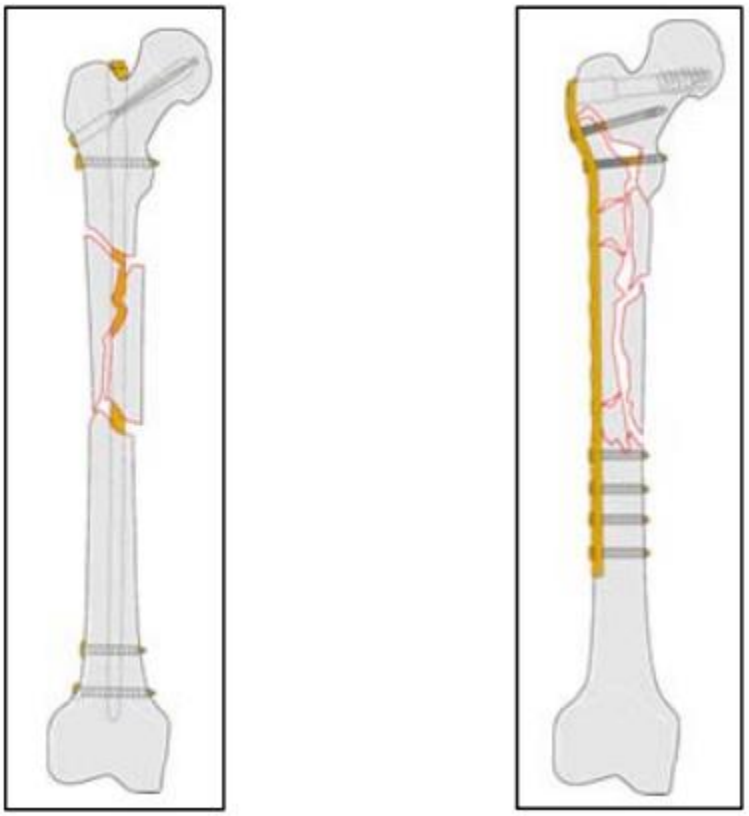

Figure 8 Intramedullary nail (left) and plates and screws (right) (Bizzarro & Regazzoni, n.d.)

An intramedullary nail is a metal rod of a length slightly shorter than the lateral length of the bone. This nail runs down the center channel of the bone that typically contains marrow. This nail is held in place by two or more screws that run through the cortical and cancellous bone around the ends of the nail. These screws prevent shortening, rotation, or other dislocation of the nail. Plates are used as internal fixation devices where an internal type of splint is deemed necessary by physicians. They run alongside the bone either in contact with the bone surface, or in close proximity. These plates contain pre-drilled holes to accommodate the screws holding them to the bone. Any of these internal fixation components may remain in the body permanently, or certain pins, wires, and screws may be removed.

A major issue with internal fixation is a patient's objection to permanent implants. Although these fixators do not obstruct movement like functional braces, they can often be felt under the skin by patients, and may inflict chronic pain. Furthermore, internal fixators present a higher risk of infection, which can then be more difficult to treat since infection sites may be internal or concealed by the fixator plate. Internal fixators may cause damage to vasculature around the fracture site, damage to muscles, and compartment syndrome arising from increased pressure within a confined bodily space. The benefits of internal fixation are its concealment beneath the skin, the ability to constrain a high number of floating bone fragments, and a second surgery is not necessary to remove the bone fixation apparatus.

2.4.3 Casts and Braces

Functional braces and casts are the most common devices used to assist bone healing. They are non-invasive, fit snugly around fracture sites, and require little effort on behalf of the physician. Casts are typically constructed from fiberglass or plaster, and function by simply holding both ends of the fractured bone in the proper physician-set position for the duration of the healing period. This is a fairly low impact solution used for less severe breaks. Casts are bulky and can hinder mobility, while occasionally being harmful to the skin underneath. However, they create relatively little pain, do not require a surgical operation to apply, and protect the bone underneath from most impacts.

Functional braces are specifically applicable in the following types of fractures located in the tibia, humerus, or ulna: stable reduced transverse and axially unstable (oblique, spiral, and comminuted). This therapeutic method of fracture healing is used a few weeks post injury to

replace the cast. These braces are based on the concept that applying motion at the fracture site stimulates bone remodeling and repair (Sarmiento & Latta, 1999).

Overall, braces are preferred over traditional casts because functional braces allow mobility on the leg by not fully immobilizing the knee and ankle joints. In addition, braces eliminate complications of infection, pain, and surgical intervention. Functional braces are easily removable and generally provide a comfortable fit. However, functional braces do little to protect bone from impact, and if not used correctly, it could result in the need for additional surgical intervention or even use of other bone healing devices such as the external or internal fixators (Sarmiento et al., 1999).

2.5 Stress Application at Fracture Sites

2.5.1 Effects of Strain Application

Adaptive fracture healing, a recent medical endeavor, relies on the concept that bone adapts and heals as a result of the strains placed on it. It is important to understand the driving forces behind bone healing with strain. Mechanotransduction is the body's process of converting mechanical strain into an electrochemical response that triggers bone healing. A popular theory for how mechanotransduction works is that the collagen and its minerals in the bone exhibit slightly piezoelectric properties (Whedon, 2014). Even the smallest strains can produce a charge in the bone, which can affect the electrochemical processes and trigger healing. (Mavčič & Antolič, 2012).

2.5.2 Tibia Structure and Fractures

The rate and frequency at which bone is loaded plays a significant role in bone healing. There is a limit to how much and how often a bone is loaded before the effects become detrimental to the bone healing process. As bone loading increases, bone formation and bone mass also increases, but at a certain point the formation response saturates. This upper limit is the point at which no matter how much higher the strain or frequency increases, no benefits are observed in bone healing (Turner, 1998).

In Table 1, strain data were compiled and organized from various fracture healing studies. It includes the source information, strain range, daily strain events, high strain events, loading cycles, frequency, and amplitude. As seen in the table, most studies used a strain range between 100-2000 microstrain, with a frequency most often between 0.5 and 2 Hz. These levels of microstrain and frequency are similar to those seen in daily activities such as walking or running.

Table 1: Complied research on necessary strain rates

Source:	Optimal Strain Range	Daily Strain Events	Occasional High Strain Events	Loading Cycles	Frequency	Amplitude
(Mavčič & Antolič, 2012)	100-2000 microstrains	1000 microstrain (Normal Walking)	3000 microstrain (Vigorous Activity)	Low at 24-100 cycles per day (Animal Experiment)	0.5-1Hz	
(Fritton, McLeod & Rubin, 1999)	<~200 microstrains	<10 mircostrain	>1000 microstrain		1-2Hz	
(Turner, 1998)	(a) 2000 microstrain, (b) 100 - 150 microstrain			Only shot duration of loading needed to initiate adaptive response	(a) 1 Hz, (b)20 Hz	
(Nyary & Scammell, 2014)	<10% strain cartilage callus formation; <1% strain woven bone forms					
(Kenwright et al., 1991)				20 minutes per day	0.5 Hz	
(González-Torres & et al., 2010)				Continuous cyclic compression during 15 minutes	Low Frequencies 1Hz High Frequencies 50-100Hz Range 1-100Hz	0.02mm (low) - 0.5mm (high)
(Claes & et al., 1998)	<5% intramembranous bone formation <15% endochondral ossification formation >15% connective tissue formation	~7% small interfragmentary strain applied	~31% large interfragmentary strain applied			

2.5.3 Recovery Time

The benefit to fracture fixation is the reduced healing time and increased stability during the healing period, especially in cases with severe fractures. In the early stages of healing, tibia fractures inhibit locomotion and almost all weight bearing. The reduction of healing time in instances of tibia fractures is of critical importance. Tibia fracture healing methods such as plaster casts, functional braces, internal fixators, and external fixators are suited to different types of fractures. External fixators, despite their size and weight may ultimately prove an attractive option for patients with severe fractures involving multiple bone fragments due to time reduction (Mallik, Covall, & Whitelaw, 1992). Despite the small sample size, this study provides a basis for external fixation and general load application in accelerating tibia bone healing. This study is followed by a synopsis of another in which similar external fixators were utilized, but in conjunction with a cyclical strain-inducing device to prove the efficacy of applied strain rate over a basic external fixator.

A study conducted by the USC School of Medicine involving 780 patients with mid-tibial shaft fractures analyzed time to application of a functional walking brace, and time to full fracture healing (Sarmiento et al., 1989). Researchers found that for this sample of 610 males and 170 females with a mean age of 30 years, prefabricated functional braces could be applied an average of 3.8 weeks post-injury for closed fractures, and 5.2 weeks post-injury for open fractures. Complete fracture healing was marked as the day that braces were removed from the patients, as doctors established that bone union had been achieved. In this study, closed fractures treated with initial immobilization healed on average in 17.4 weeks, while open fractures took 21.7 weeks on average to heal fully (Sarmiento et al., 1989).

Another method of bone healing, plaster casting, utilizes a stiff external cast that fully immobilizes the fracture site. This is a commonly used way to treat simple, or clean, mid-shaft tibia fractures. A 2001 study analyzing the treatment low-energy of tibia shaft fractures by plaster casting utilized a sample of 54 patients exhibiting similar fractures and established a mean healing time of 19 weeks (Toivanen et al., 2001). Other sources recognize that tibial-shaft healing via plaster casting generally takes between 12-16 weeks ("Broken Leg in Depth", n.d). Differences in healing time between tibia fractures may result from fracture location, whether the fracture is open or closed, and the number of bone splinters or fragments resulting from the break. Nonunions or delayed union can also prolong the healing period for tibia fractures.

Boston City Hospital conducted a study spanning from 1986 to 1991 in which their surgeons treated 60 tibia "bicondylar" plateau fractures in 59 patients (Mallik et al., 1992). Three of these patients were treated using external fixation frames, while the remaining patients were treated with internal fixation. Average healing or follow-up time for patients with internal fixation was 33.4 months. In contrast, the average healing time for external fixation patients was 16 months (Mallik et al., 1992). In addition to the average 17.4 month decrease in healing time, only three patients with external fixators contracted minor infections, while four out of five patients with internal fixators experienced much more dangerous infections which needed surgery to address (Mallik et al., 1992).

Armed with the knowledge of how external fixation frames can accelerate bone healing and minimize infection risks, a team of researchers conducted a study to research benefits of strain application in bone healing. These researchers conducted a prospective study to determine if highly controlled axial micromovements around a fracture site could enhance the healing of tibial fractures. This was accomplished with a test group of 80 patients divided into two groups.

While both were treated with unilateral external fixators, group one utilized cyclical loading to induce mechanotransduction, and group two patients were treated with fixators with a high stiffness intended to reduce as much micromovement around the fracture site as possible. All frames were applied within one week of injury. The micromovement program consisted of 1.0 mm axial compressive displacement at 0.5 Hz for 20 minutes each day. The maximum possible force applied by the pump was capped at 300 N to avoid damaging the bone and fixator. The application of these micromovements were continued until either the patient was ambulatory or until three weeks had passed (Kenwright et al., 1991).

The full, unsupported weight-bearing period was reached for group two after 29 weeks, compared to the mean healing time for group one which was 23 weeks. Both groups had no incidence of fracture infection, and pin tract infection rates were comparable between groups. However, in the fixed group, three patients experienced a refracture of the tibia, compared to zero from the other group. Similar numbers of patients from each group required a secondary surgery to achieve initial bone union (Kenwright et al., 1991).

In the group with micromovements, a long periosteal callus sheath formed around the bone adjacent to the fracture. This development did not occur with completely fixed zero micromovement frames (Kenwright et al., 1991).

2.5.4 Limitation and Variability of Application

The mechanical properties of tibia bone can vary between patients. Therefore, bone healing and regenerative methods must be highly personalized to each patient and fracture. The same applied force will not necessarily translate into equal tibia strain between patients because differences in bone density, structure, composition, and size impact the loading behavior and

elastic modulus. These values can be difficult to predict for patients due to the "Utah Paradigm" of skeletal physiology. Simply put, this says that early in bone formation, structural and chemical properties are determined by genetic predisposition and later in life, upon being subjected to different loading levels, bone experiences mechanotransduction in addition to formation and resorption drifts which results in changes in strength. Bone is constantly undergoing turnover by basic multicellular units that absorb and regenerate bone matter (Mavčič & Antolič, 2012). In addition to the continual resorption/regeneration processes within the bone, the patient's gender, age, nutrition, level of activity, ethnicity, stature, weight, and hormone levels influence the elastic modulus and tensile strength of cortical and cancellous bone (Gillet & Cescotto, n.d.).

After humans age to the point of physical maturity, their osteoblast/osteoclast balance gradually shifts to favor osteoclast activity, slowing the regenerative rate of bone. Along with this change comes a gradual reduction in mineral density within the bone and a 2% decrease in the cortical bone modulus and tensile yield strength for each decade after the age of 20 (Gillet & Cescotto, n.d.). The greatest drop in bone mineral density in the tibia is found in females as they age past 60, making this a demographic for orthopedic surgeons to be particularly aware of (Khodadadyan-Klostermann et al., 2004). Furthermore, despite having a comparable body size, males have larger skeletons than females, a higher bone mass on average, and greater cortical thickness in the tibia than females, as illustrated in Figure 9 (Nieves et al., 2004). These properties result in males having more robust bone structures and composition, which means greater bone strength. Female bones tend to be smaller and more brittle with less cortical bone content, making stress fractures far more common in females, as revealed in an American study on military cadets (Nieves et al., 2004). Bone disease such as osteoporosis may cause the loss of trabeculae, and as a result, loss of overall structural integrity of bone (Gillet & Cescotto, n.d.).

	Female	*Male*	p *Value*
Length (mm)*	405.0 ± 4.1	401.9 ± 3.4	NS
BMC (mg/mm)	298.0 ± 6.26	336.6 ± 6.3	0.001
BMD (mg/cm^3)	794.3 ± 12.8	850.1 ± 14.1	0.004
Total bone area (mm^2)	377.1 ± 8.1	398.1 ± 7.3	0.011
Cortical area (mm^2)	237.1 ± 5.1	273.6 ± 5.3	0.001
Cortical content (mg)	273.8 ± 6.04	313.6 ± 6.29	0.001
Cortical thickness (mm)	4.32 ± 0.09	5.02 ± 0.11	0.001
Periosteal circumference (mm)	68.7 ± 0.75	70.6 ± 0.67	0.011
Endosteal circumference (mm)	41.6 ± 0.96	39.1 ± 1.00	0.058
Fat mass area (mm^2)	2311.4 ± 80.7	1546.5 ± 60.9	0.001
Muscle mass area (mm^2)	2487.5 ± 60.6	2896.1 ± 68.1	0.001
Percent fat (%)	44.5 ± 0.9	31.6 ± 0.9	0.001

* Measured by investigator.
NS, not significant.

Figure 9 Proximal Tibia Analysis by pQCT (Nieves et al., 2004)

2.5.5 Strain/Load Inducing Method

The micromovement, mechanotransduction inducing pneumatic pump device detailed in the previous section is one of the few devices that applies a cyclic stress to a fractured bone to promote bone regeneration. Alternate devices incorporate walking forces, and similar to the springs on the unilateral fixators in Kenwright's study, diminish the patient's force from walking experienced by the tibia. It uses the walking force as a natural loading cycle to promote bone regeneration (Kenwright et al., 1991). There exist walking boots that fashion in a similar manner, but the biggest issue remaining with these devices is that they cannot apply a strain rate higher than the frequency at which a patient takes a step. This is highly dependent upon gait analysis, and for each patient it is highly individualized. Although lower strain rates can effectively mitigate viscoelastic effects on bone, strain rates for ideal healing conditions for mechanotransduction are higher than the roughly one second period it takes for the average human to complete one step.

An external fixator alternative, shown in Figure 10, known as a Braun frame, functions as a traction device, applying a tensile force to the tibia, but it utilizes a creative method of fixating to the tibia and has potential in cyclic loading applications. A Braun frame is applied by surgically fitting a calcaneal pin sideways through the central portion of the heel bone. A U-shaped stirrup is then attached to this pin at each end, allowing for the rotation of the stirrup around the pin while preventing the pin from rotating inside the bone and subsequently loosening. The calcaneal traction device portion is then attached to the rest of the Braun frame, which elevates the tibia and the foot, and provides counter support against the knee and thigh to enable the application of force on the tibia. Upon complete assembly of the frame, a pulley is affixed to the end of the stirrup, and a weight is hung on a line off the end of the pulley. This weighted traction system allows for the application of a static tensile force. Although it is currently used to apply tension, the stirrup could easily apply a compressive force in the same manner. Furthermore, this device could be adapted to apply a cyclical compressive force to the tibia by using an electric motor attached to an eccentric and geared to apply a tibia loading cycle at a predetermined rate (Demmer, 2012).

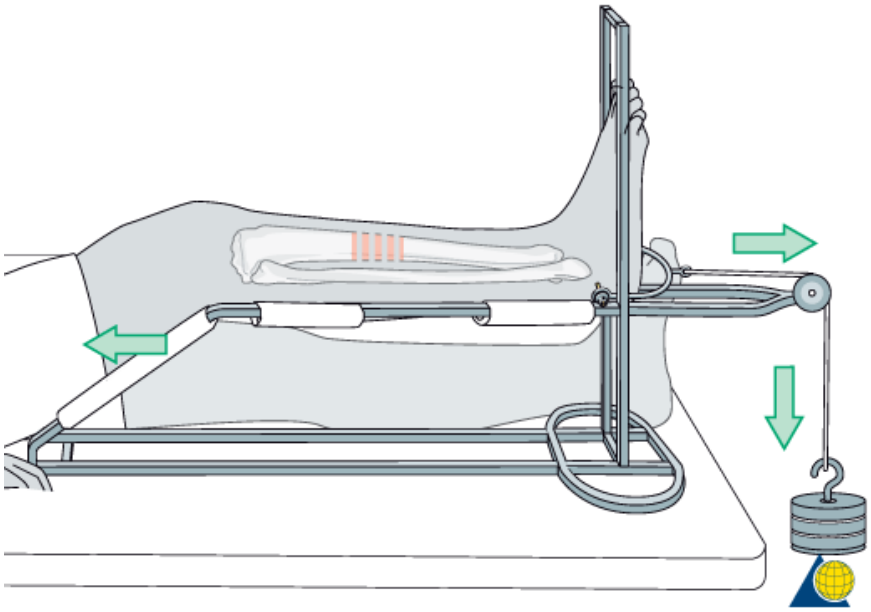

Figure 10 Modern Braun frame traction device (Demmer, 2012)

Another type of strain-inducing device has been proven effective and non-invasive, but only in rats, as of this date. This device consists of either two contoured pads that press axially in toward the tibia at the heel and at the knee or two ports that attach to connectors on an external fixator. The load applying device is oriented parallel to the tibia, in both scenarios. These two similar devices utilize clamp mechanisms driven by an electric step-motor to control the loading rate. Both devices were custom-built for studies in which researchers produced transverse fractures in lab rat tibias, applied a unilateral external fixator in Robert Brophy's study, and manually set the fracture straight in the Roshan-Ghias study. Researchers then applied cyclical compressive forces with a computer-controlled loading device (Figure 11). These studies were based on hypotheses regarding the optimization of specific loading parameters for tibia regeneration, so these rigs were custom built and have not been adapted to humans. They do, however, provide a basis for the design of tibial-load-application fixtures for humans, as well as proof of accelerated healing for such designs (Rosihn-Ghias et al., 2010; Brophy, 2011).

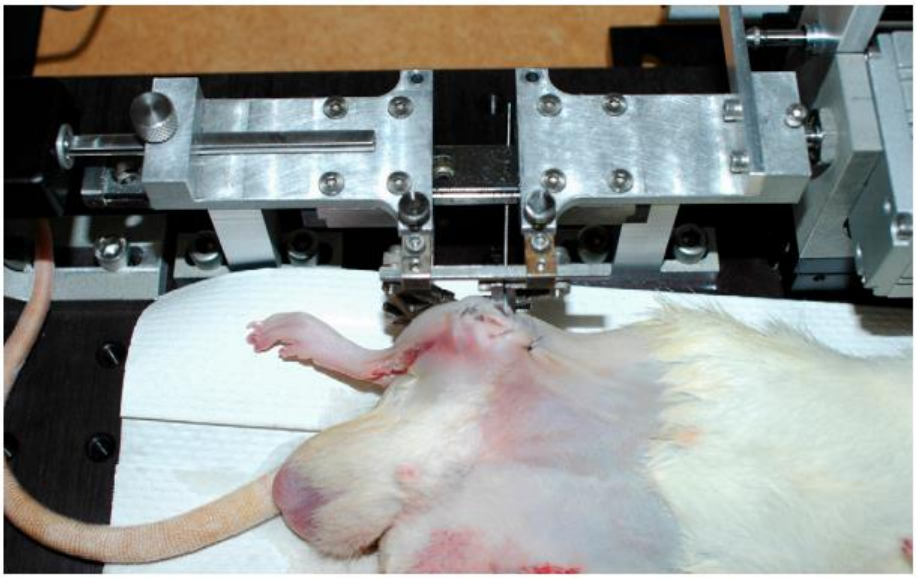

Figure 11 Rat with external tibia fixator (Brophy, 2011)

2.6 Ideal Mechanical Conditions for Bone Fracture Healing

Various studies and experiments have been conducted on the mechanical factors of bone healing. The purpose of these experiments was to identify the optimal conditions in regards to the rate and level of loading to induce effective bone healing. Mechanical conditions are important because of their influence on the bone healing process, specifically callus formation as described in a previous section. Further research indicates that the ideal mechanical conditions for applied strain, frequency, and stability of the fracture have not been identified, but a range of acceptable values can be concluded with taking into consideration contradicting data across experiments (Claes et al., 1998).

Strain is the main mechanical factor to be considered in identifying the ideal conditions. As seen in Table 1, ranges of strain have been identified as effective values to be applied to induce bone remodeling. According to a recent article from 2012, an optimal strain range is 100-2000 microstrains (Mavčič & Antolič, 2012). Another source was less specific in determining

that bone formation occurred at the fracture site with strains less than 5% or 50,000 microstrains (Claes et al., 1998). An exact optimal strain value is not possible to determine due to other characteristics that influence bone repair. An ideal strain rate required for a fracture is specific to the particular patient and points in the healing process (Mavčič & Antolič, 2012). The application of strain must be adaptable based on the variance of values necessary to promote the correct bone formation.

Other mechanical factors include gap size and frequency of loading. According to the research, it was shown that the size of the gap between bone fracture fragments affects the effectiveness of bone healing. If the size increases, then the healing is negatively impacted (Claes et al., 1998). For the best healing conditions, the gap size must be less than 2 mm (Vicenti et al., 2014). In regards to frequency, there are currently conflicting studies whether high frequency or low frequency should be used to obtain the best healing results. The range of frequencies, available in Table 1, is from 0.5 Hz to 100 Hz; an accurate representation of the frequency utilized in most fracture healing testing can be found on the lower end of the scale around 1 Hz. However, the lack of experimental data on fracture healing applied at higher frequencies implies the potential of these values being more ideal for bone formation (González-Torres, Gómez-Benito, Doblaré & García-Aznar, 2010). In relation to frequency, it has been determined that a dynamic cyclic loading of the strain stimulates a higher level of bone remodeling compared to a static or constant load on the bone (Turner, 1998).

In the case of the tibia, an additional ideal fracture healing condition is the ability for full or partial mobility of the bone during the healing period. The research on weight bearing of the fractured limb indicates the possibility of using the load supported between the brace or fixator and the bone to improve the healing. Weight-bearing is also used as an indicator of fracture

healing over time. A decrease in the load applied to the healing device indicates that effective bone regeneration has occurred as it has transferred load away from the device to the bone (Joslin, Wastuagh-Waring, Hardy & Cunningham, 2008; Vihayakumar, Makrs, Bremmer-Smith, Hardy & Gardner, 2006).

Overall the mechanical and additional conditions that are ideal for the most effective bone healing include a cyclically applied strain at a frequency which prompts the bone to remodel with potential functionality of the limb.

2.7 Current and Future Fracture Healing Technology

As mentioned, the three methods used to heal fractures include internal fixation, external fixation, and casting. Current research looked to improve more on the latter of the two methods. The group looked to improve on the current methods of fracture healing, specifically focusing on functional braces.

A specific type of functional braces used is the patellar tendon bearing (PTB) brace. This type of functional brace allows weight bearing and mobility. PTB braces allow load transferring to supportive splints and unrestricted ankle and knee movement (Alimerzaloo, Kashani, Saeedi, Farzi, & Fallahian, 2014). As with most functional braces, the drawback of this brace is utilization only at the end of the healing process which is 4 to 6 weeks after injury (Demmer, 2012).

Traditional fracture fixation systems use rigid compression plates that do not allow for any movement at the fracture site; this type of healing is known as primary bone healing. Common complications with this type of healing include stress shielding, delayed union, nonunion, refracture, and infection. While primary healing is necessary for certain fractures,

there are many that do not need absolute stability. Secondary bone healing can withstand strains between 2% and 10% and can withstand some motion. (Egol, Kubiak, Fulkerson, Kummer, & Koval, 2004). This type of healing focuses on movement of the fracture along the fracture axes to encourage soft callus formation. The size of the gap in the fracture and the movements should be small because if either is too large, the hard callus formation is negatively affected (Vicenti et al., 2014). Recent advancements focus on improving secondary bone healing.

An improvement to the traditional plate and screw method is the locking plate technique. A unique aspect of the locking plate is the single beam construct that does not allow any motion between the plate, screw, and bone. This enhances the strength of the plate and helps it perform better than a conventional plate. When ideal conditions such as proper screw torques, no major loading, and sufficient friction between the plate and bone cannot be met, typical plates fail. However, the newer methods remain as a single-beam construct and are able to uphold under non-ideal circumstances. The locking plate can also accommodate for situations where the fracture gap is not small enough because it is a fixed-angle device. Locking plates are extremely rigid external fixators that optimize secondary bone healing (Egol et al., 2004).

Recent researchers have further improved locking plates by incorporating locking nails into the locking plates. The combination of the nails and plates provide proper axial and rotational alignment around the fracture and also promote secondary bone healing (Figure 12). The screws used in this system are made of cobalt-chromium-molybdenum alloys and are composed of two sleeves. The inner piece locks to the plate, and the outer piece locks to the bone. The inner pin can move slightly within the outer pin shell, and together they modulate the rigidity of the locking plate system. Depending on the rigidity, bone healing is stimulated, and secondary bone healing quickens (Vicenti et al., 2014).

Figure 12 X-ray of locking plate and nail system one year after surgery (Vicenti et al., 2014)

Many advancements have been made in internal and external fixators in recent years, however the casting technique has essentially remained the same. The focus was on improving the casting technique in an effort to fill the gaps of the fixator systems without placing the system inside the body. Initial thoughts focus on the idea of a pneumatic pump in a functional brace. An external fixator that used a pneumatic pump was designed a couple decades ago, and the pneumatic pump design has recently been used in knee braces. The pump utilizes pneumatic air bladders as the unloader to dampen the knee flexion during walking (Cherian et al., 2015). The aim was to strive to adopt a similar idea in a brace to avoid using a fixation system to heal bone.

Chapter 3: Methodology

The goal of the project was to create a strain inducing device that produced the value for strain associated with successful bone healing in a simple transverse tibia fracture. Our primary focus was applying the correct amount of force to a tibia model with accurate material and mechanical properties. We designed and created a device to shield the tibia from damaging forces, while applying a controlled amount of force to the tibia inducing a strain at the fracture site; this compressive force would aid in the bone regeneration process. The various design concepts relied on strain application principles that either apply strain externally by the device or utilize and dampen the strain produced from walking.

3.1 Design

3.1.1 Preliminary Designs

3.1.1.1 Design #1: External Fixators

This device would be an external fixator installed directly into the bone using rods and pins. The force on the bone comes from a static system working with the external fixator. Springs that load one side of the fixator and ratchet devices were both simple mechanical strain inducing devices which could be used on this type of fixator. The advantage of this type of system was the materials used to construct an external fixator, 5 mm pins and aluminum alloy bars, were readily available. This system would allow for stabilization of the fracture and precise control over the location of the applied strain. However, since this system utilized static strain inducing devices, there would be a constant force but not a constant frequency or loading cycle. A loading cycle with force applied and released from the bone was critical for bone healing. This

device would be implanted directly into the bone, which requires a surgery for installation and removal. The patient would not be mobile while wearing the device.

The construction of the external fixator would connect rods and clamps to the bone with pins. The design of the device would vary based on how many pins were used, where the pins were located, and how close the bar was to the bone. A cyclic loading test used to simulate walking would be done on an Instron machine to see which combination of pins and distances work best. The construction of this device would be feasible, and the components would not be too expensive. A possible complication would be installing the pins in the bone. In current external fixators, the pins were carefully placed in the bone to prevent infection and ensure they do not interfere with the callus formation at the fracture. Modifications of this basic design would apply strain to the bone through a pneumatic pump or motor, as described in the below designs.

3.1.1.2 Design #2: External Fixator with Pneumatic Device

The pneumatic actuated force application device may be permanently affixed or temporarily attached to an external fixator frame. This device would apply a controlled, compressive force at a variable rate to the fixator clamps, which then translated into a compressive force at the fracture site. Advantages of this design include superior control of the location, rate, and magnitude of force applied to the fracture site and ease of manufacturing. The location of the force would be accurately controlled through the location of the pins because the force was applied through the device and directly into the screws and pins. A downfall of this device was the patient must have an external fixation device for the entire treatment period. A major drawback to this design was the need for an air compressor, which was large, immobile,

and required a power source. Figure 13 shows this device featuring the bone analogue, fracture site, and a unilateral external fixator attached to a pneumatic pump plugged into its compressor apparatus.

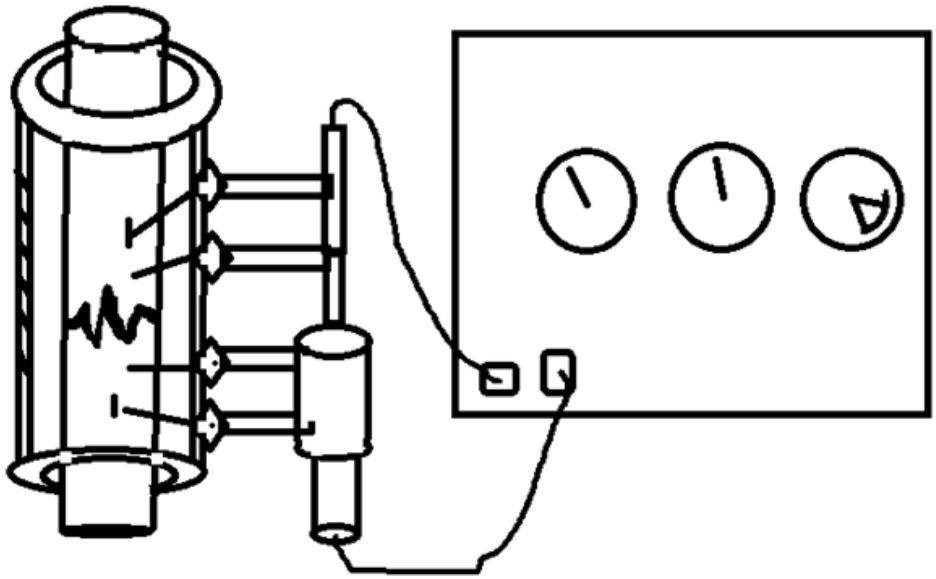

Figure 13 External fixator with pneumatic pump

3.1.1.3 Design #3: External Fixator with Strain Inducing Motor

The advantages and disadvantages of this device were similar to those for the pneumatic device. An electric step motor allows for a high level of control over the strain cycle and force applied. However, it is largely immobile and requires an external fixator. This step motor would either be permanently attached to the fixator at the cost of mobility and weight or manually attached to the Schanz screw clamps on the external fixator frame by the patient before beginning their strain inducing loading cycle treatment. The motor would be compatible with the standard 120 V outlet, making home use of the device feasible. One of the largest drawbacks to this device was the limited device actuation duration. The motor may only be run when the

patient was immobile, near a power source, and the tibia was not weight-bearing. Figure 14 presents a sketch of this device. It includes the bone analogue, a unilateral fixator, and a strain-inducing motor attached to the clamps on the motor and actuating to articulate two of them.

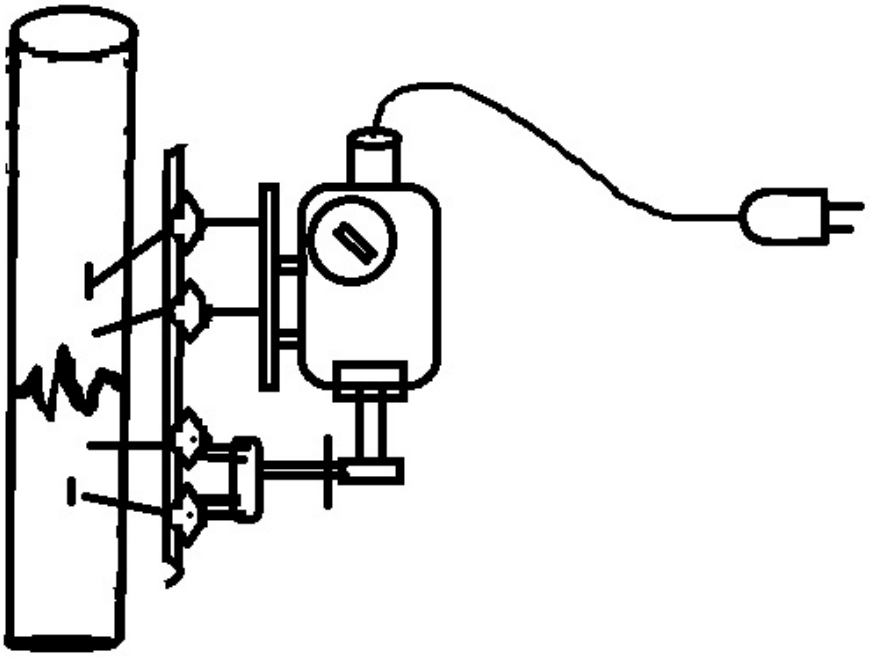

Figure 14 External fixator with an electrical motor

3.1.1.4 Design #4: Functional (Force Dampening) Walking Brace

Plaster Cast Idea:

Another idea improved upon a traditional plaster cast. This device would cast the knee and ankle joint to immobilize them, but leave the rest of the leg open. On the open part of the leg, force absorbing components would be added in order to dampen walking forces down to appropriate local forces on the tibia for healing. Another option was to install force inducing components on the open portion of the leg and immobilizing the patient during healing. This would allow the force placed on the leg to be more carefully controlled and applied.

Advantages of this design included the use of common casting materials; in theory, the force inducing or absorbing device could be produced and put into use in the current system. Other advantages are the ability to induce the correct strain on the bone and immobilization of the ankle and knee; hard plaster casting leaves a solid platform to push against and allows for better control of the forces on the tibia. However, the immobilization of the knee and ankle joint was a disadvantage to this design, and the patient would likely be in a wheelchair or on crutches during the recovery period.

Functional Type Brace Idea:

Another design approach would improve upon the patellar tendon bearing (PTB) brace. The PTB brace immobilizes the ankle and allowed some joint mobility. The PTB brace was typically used at the very end of the fracture healing process. Our improvements would aim to implement a similar device earlier in the healing period. Our device would dampen walking force down to a level where the resulting strain was conducive of tibial fracture healing. One method to control the amount of dampening produced by the PTB type walking brace was to control the gap underneath the heel in the PTB. A larger gap led to less force transferred through the foot and thus tibia during walking (Tanaka, 1999).

A study has shown the extent to which these PTB braces are capable of dampening forces to the tibia. The results in Table 2 show the percentage of body weight unloaded dependent upon the corresponding size of gap beneath the heel induced by a PTB brace (Tanaha, et al., 1999).

Table 2: PTB brace gap size and body weight percentage unloaded (Tanaha, et al., 1999).

Gap Size (cm)*	Body Weight
0	30%

1	60%
2	80%
3	98%

In Figure 15, a gap was induced beneath the foot in a PTB cast with a bellows bag with a Tekscan F-scan system sensor placed under the foot to determine the force (Tanaha, et al., 1999).

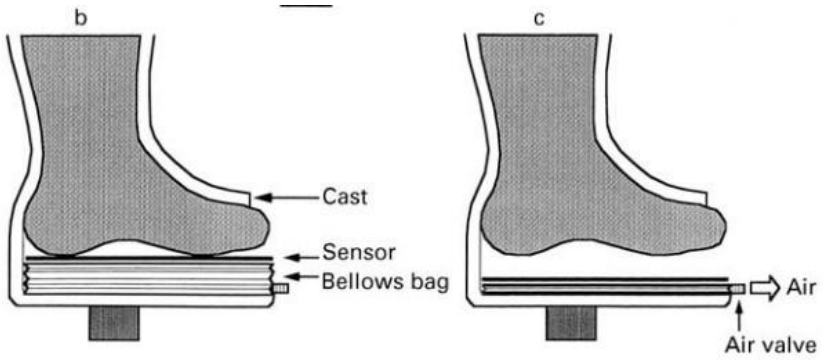

Figure 15 PTB cast showing induced gap beneath the foot (Tanaha, et al., 1999)

3.1.2 Design Evaluation

Design Parameters:

Design Parameters for Prototype Device

1. Ability to apply a 1000 - 2000 microstrain to transverse tibial shaft fractures at a cycle of 0.5 to 2 Hz
2. Dampen ground reaction force to 400- 800 N for the desired microstrain
3. Sustainable to at least 750,000 loading cycles
4. Laterally stable to protect fracture site and healing bone from shear forces
5. Stabilization of joint locations (knee and ankle) surrounding the fracture site
6. Total cost of prototype and subsequent iterations less than $600

Design Parameters for Commercial Device

1. Allows for patient mobility (slow walking)
2. Device must be small enough to refrain from impairing everyday activities any more than other marketed walking boots
3. Biocompatible materials for components in contact with biological tissue (would not cause immune response or infection)
4. Ability to be used after initial injury for sufficient bone regeneration
5. Lifetime durability of at least 1,000,000 cycles

Design Matrix:

The following design matrix (Table 3) was based on a grading system. Each of the designs in Section 3.1.1 was evaluated using the matrix to get a final score; theoretically, the design with the highest score would be the best option. In the second-to-left column, each category was given a weight, or a relative importance, and to the right of this column each design was ranked on a scale of 1 to 5 with 1 being least desirable and 5 being most desirable. These rankings were then multiplied by the weight of their category, and these values were summed up for each device to obtain a score for each design option.

Table 3: Design Matrix

Category*	**Weight (1-5)**	**External Fixator**	**External Fixator with Pneumatic Device**	**External Fixator with Strain Inducing Motor**	**Functional Walking Brace**
Cost	**2**	3	2	2	4
Force Control	**5**	2	3	4	3

Adjustable to Patient	**3**	4	4	4	5
Manufacturability	**4**	4	2	3	4
Strain Rate Control	**5**	1	5	5	2
Time to Implementation	**3**	5	4	4	2
User Experience	**3**	3	2	2	5
Mobility	**4**	1	1	1	5
Invasiveness	**3**	2	1	1	5
SCORE		**83**	**89**	**98**	**120**

*See Appendix A for descriptions of each category.

3.1.3 Final Design Chosen

Based on the weighted design matrix, the functional walking brace was chosen as the primary design to pursue based on the manufacturability, mobility, and invasiveness categories.

3.1.4 Design Intent

This section outlines and explains the design choices that we made and presents an understanding of how the device functions.

3.1.4.1 Design Iteration 1

The functional walking brace was made with components from a PTB brace (Figure 16a) and an AirCast walking plate (Figure 16b) with support components in the knee and ankle areas. The design combined the PTB brace's structural support components with the walking boot's foot plate, cushion, and tread. In order to transfer the walking force from the foot plate to the knee, bypassing the tibia, the foot plate was made adjustable by attaching a 7-inch threaded rod on each side of the PTB brace. The rods are affixed to the foot plate at the bottom that allowed the rods to rotate freely. The foot plate would then be vertically adjustable based on the movement of the threaded rods. Additional straps around the knee provided further support for the knee, tightening the front of the PTB brace below the tibia.

Figure 16 (a) PTB brace; (b) AirCast walking boot

The PTB brace was used with the original footplate detached. A PTB brace consisted of two halves: the back, which was affixed to the outer shell of the device, and the front half, which was then attached with Velcro to the rear half and secured up to the knee and down the front of the tibia, as seen in Figure 16. The outer shell consisted of the modified AirCast walking boot

used as a functional foot plate, as seen in Figure 16b. The walking boot featured fabric padding and Velcro straps around the foot plate to comfortably secure the foot in place without a need for the front shell. Furthermore, the Velcro straps used to attach the front plate to the walking boot were utilized to stabilize the front half of the PTB brace.

The rear half of the PTB brace was bolted to two threaded rods ⅜ inch offset wall mounts. These must be mounted at a height where the diameter of the PTB brace plus ⅜ inch on either side is equal to the diameter of the AirCast. This was necessary to have the bottom of the threaded rod rest on the bottom edge of the slot cut in the AirCast. These wall mounts were designed for ⅜ inch-16 threaded rods. We used black-oxide steel positioning rods of this diameter and thread. Positioning rods have a smooth, flat surface midway, allowing them to be adjusted with a wrench at that location. Rotating these rods moved them vertically through the threaded surface on the wall mount and shifted the foot plate and outer shell assembly up or down relative to the PTB brace. A slot was cut into the side of the walking boot, contoured at the top to accommodate the width of the wall mount and thinner at the bottom to allow our foot plate vertical bracing components to span the gap in the sidewall of the walking boot. The threaded rod rested against the bottom of this slot to add support to the structure and a hex nut fixed with Loctite will rest offset from the end of the rod, locked into position so that it rotates with the rod. Both the top and bottom of this nut were held in place vertically relative to the foot plate by two structural components: a $^{9}/_{16}$'' clamp half, and a 1 ½'' plate. Both of these span the slot in the walking boot and hold the nut in place vertically, as well as helping to position the threaded rod. The nut was supported between these two components and able to spin freely with the threaded rod, moving the foot plate up and down. This design can be seen in the Figure 17 below, on the right hand side of the brace assembly.

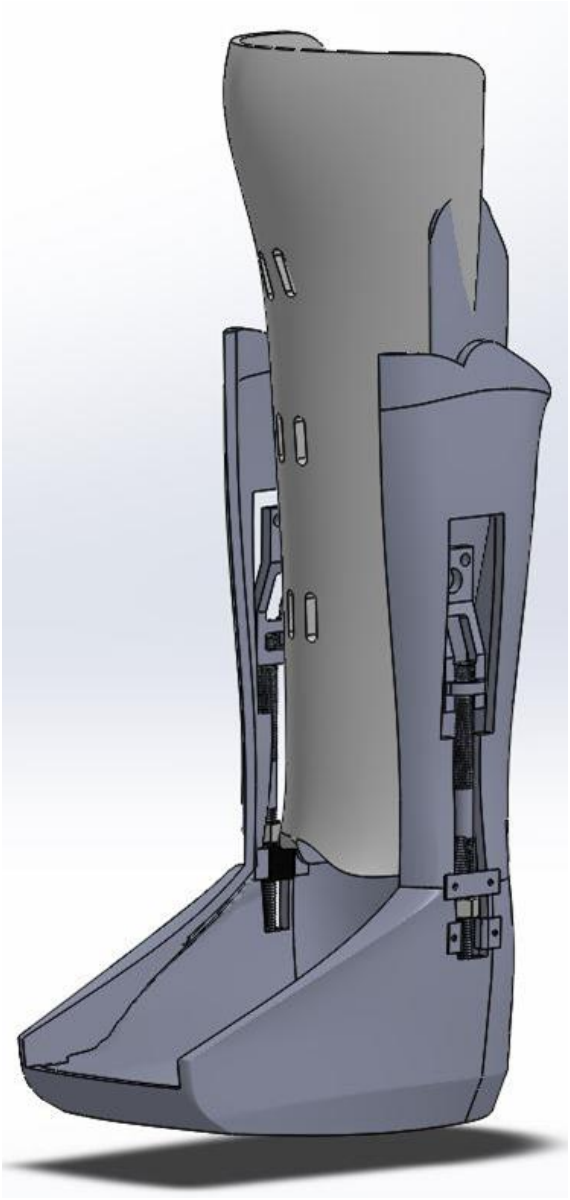

Figure 17 Bracket assembly drawing (right side)

The alternative to using the clamp half and the steel plate was a vibration-damping ⅜'' clamp half with a rubber insert, reducing the inner diameter to exactly ⅜ inch. To accommodate for this, the construction of the device was for a better fit and guide for the threaded rod, dampens some of the force felt on the knee through the PTB brace, and increased friction on the rubber-contacting thread, preventing the threaded rod from rotating inadvertently. This design alternative is visible in Figure 18.

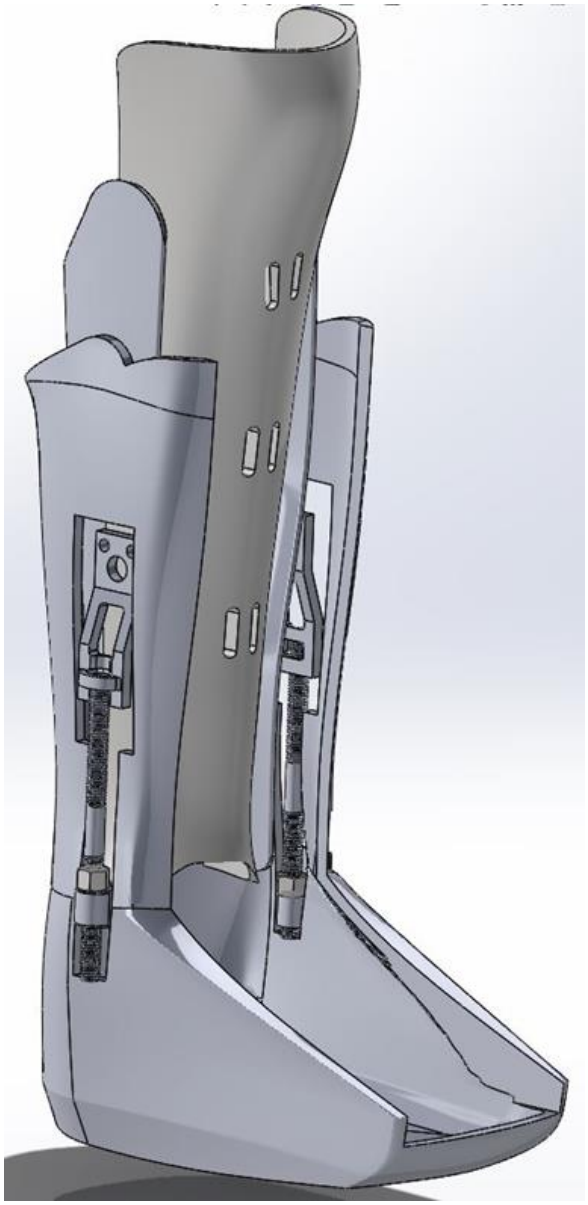

Figure 18 Brace assembly drawing (left side)

3.1.4.2 Design Iteration 2

The second design iteration was created based on feedback from the test subject trying on the device and on the results of force sensor walking test detailed in Section 3.4.3. The subject identified a need for a tighter fit and increased support and stability around the knee. We attempted to resolve these issues with the addition of padding beneath the patella on the PTB

brace front and slots in the PTB front half for another strap around the knee. When the subject felt minimal improvements, we removed both of the aforementioned changes, and utilized the air cushion from the original AirCast assembly. It was installed at the back face of the PTB brace and pushed the leg up against the front face of the PTB brace to provide a more secure fit in the boot.

Next, we provided a supporting structure behind the knee where the rear PTB brace half failed to provide adequate support since it does not extend as high as the front half. The front plate of the AirCast walking boot, which was removed to make the boot more accessible to the patient, was repurposed. This material now makes up the popliteal (back of the knee) stabilization component. This bracing component was bolted to the AirCast at two points, which allowed it to rotate and flex slightly while the subject was walking, and more importantly, kept the knee pressed against the front of the PTB brace. This was possible because the two slots cut in the top of the component on either side allowed us to run a strap around this component, behind the leg, across the front of the knee and over the PTB brace. This pulled the popliteal component forward against the back of the knee, pinched the popliteal component in around the sides of the knee, and pulled the front of the PTB brace firmly against the subject's knee. These new components made the subject more comfortable and confident in the boot.

3.2 Construction

This section outlines the construction process of the two components necessary for testing: fracture healing device and bone analogue.

3.2.1 Device Construction

3.2.1.1 Construction of the Functional Walking Brace

Design Iteration 1:

Modified XP Walker AirCast

1. Remove all padding from the interior and exterior of the boot with the exception of the padding below the foot, and the padded straps that run over the top of the foot. Remove the air bladders, taking care not to rip them when pulling off of glued sites, or breaking the valve when removing it from its seating in the plastic AirCast body.
2. Remove and save the AirCast front plate, and the foot protector plate to be used later as the popliteal brace component and the foot protector, respectively.
3. Cut identical slots in each side of the medium XP Walker AirCast, as shown in Figure 19. Although we angled the widening of the slot at 45° for aesthetic purposes, this cut is not critical to the design or functionality of the device, as long as the width of the hole varies adequately.
4. Drill two $^{1}/_{8}$'' through holes near the bottom of the slot, as shown in Figure 17.
5. Drill two ¼'' holes at a distance 1 ¼ '' above the previously drilled holes (Figure 17).

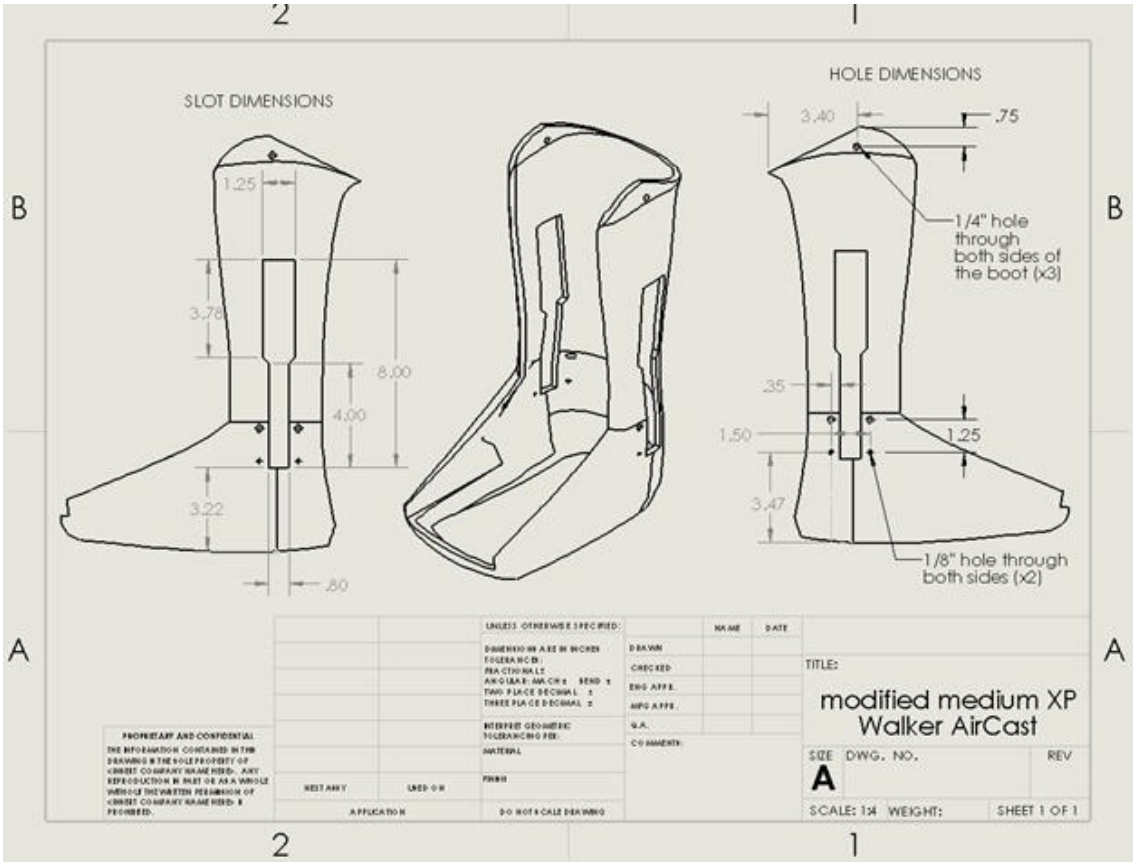

Figure 19 Medium XP Walker AirCast modifications

Modified AliMed Tibial Fracture Orthosis (TFO-PTB) with Shoe Insert, Left, Medium

1. Detach the foot plate and supports from the PTB brace back.
2. Remove and save the Velcro from the foot plate.
3. Drill four ¼" through holes in identical positions on each side of the PTB brace back (Figure 20).

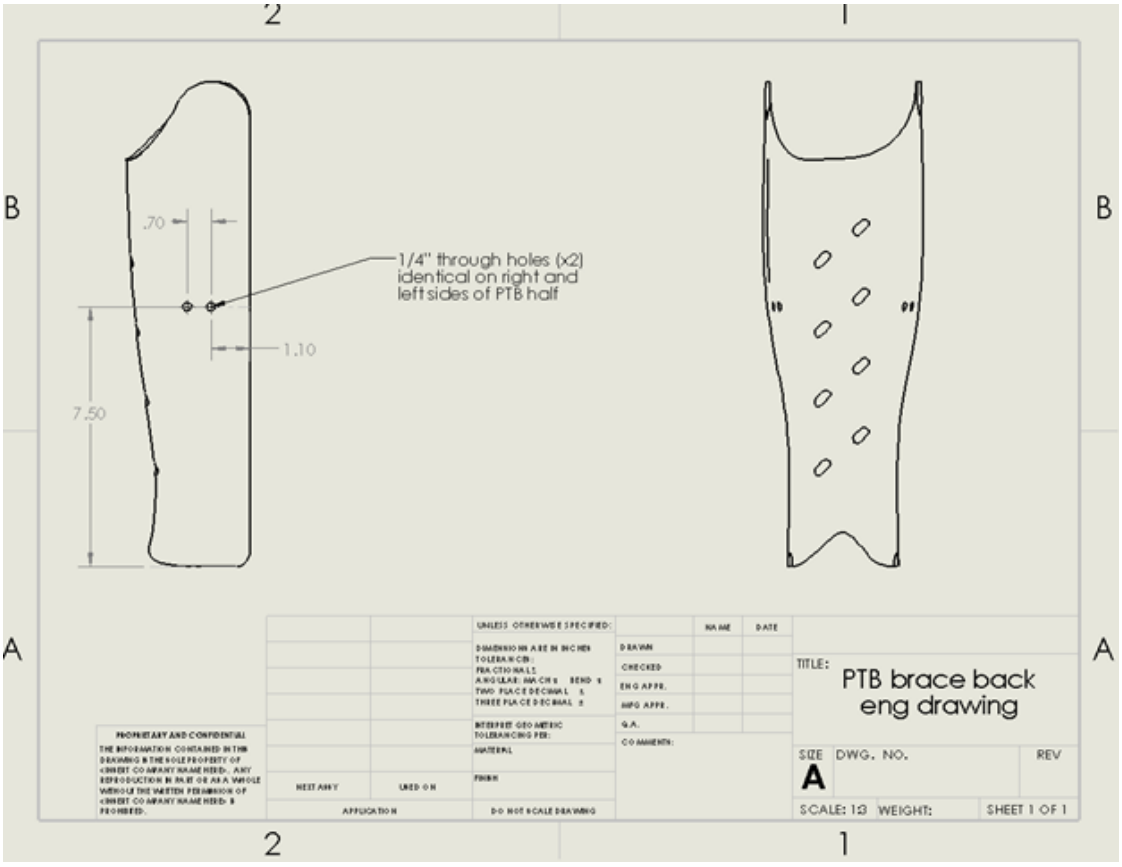

Figure 20 PTB brace back half modifications

Design Iteration 1 Assembly

1. Attach the threaded rod offset wall mounts to the PTB brace back half using four ¼-20 thread ½'' long hex head cap screws and four ¼-20 thread steel hex nuts (reference Figure 21 for their orientation).

2. Insert a $^{3}/_{8}$-16 thread 7'' long positioning studs into each threaded rod offset wall mount.

3. Thread each rod up through the wall mount so that they rest at equal heights relative to each wall mount.

4. Maneuver the PTB brace back half inside the modified AirCast, facing outwards. Position the threaded rods so that the wall mounts protrude through the wider portion of the slot, and the bottom of the rod rests upon the bottom of the AirCast slot.

5. Place one vibration damping bracket around the threaded rod, and position it so that the holes in the bracket align with the ¼'' holes drilled in the AirCast. The bottom of the threaded rod must still rest on the bottom of the slot as shown in Figure 21.

6. Twist a $^{3}/_{8}$-16 thread hex nut onto the threaded rod so that the bottom of the vibration damping bracket sits on top of the hex nut.

7. Place a $^{9}/_{16}$'' steel clamp so that it aligns with the $^{1}/_{8}$" holes in the AirCast, and so that its' indentation rests inside of the slot, and the hex nut rests atop the u-shaped indentation in the bracket.

8. Having seen the fit of the bracket, remove the bracket and bend with two pairs of pliers so that the two outer metal tabs (with through holes) are contoured to the curve on the outside of the AirCast, and so that the indentation can still fit around the threaded rod and into the slot.

9. Before replacing the $^{9}/_{16}$'' bracket, remove the $^{3}/_{8}$-16 thread hex nut, then coat the spot approximately ¾" up the threaded rod from the bottom with Loctite, where the hex nut will stay. Twist the hex nut back up to this point on the threaded rod, between the two brackets, and allow it to cure. Refrain from rotating the hex nut for the rest of the assembly process.

10. Using two ¼-20 thread ½'' long hex head screws and matching hex nuts, secure the vibration damping bracket to the AirCast through the ¼" diameter holes on either side of the slot

11. Using two 5-40 Phillips pan head ½'' length screws and 5-40 hex nuts, secure the $^{9}/_{16}$'' metal bracket to the AirCast through the $^{1}/_{8}$'' holes beside the slot.

12. If adjustments need to be made to ensure proper alignment of the threaded rod; so that it rests atop the bottom of the slot, the tabs of either bracket may be moved to the inside or outside of the AirCast wall, as long as one bracket secures the outer side of the threaded rod, and the other bracket secures the inner side of the threaded rod. Additional measures may be taken if

necessary, such as reversing the rubber insert in the vibration dampening clamp to provide a further offset from the metal component, or adding a 1 ½'' plate inside the AirCast wall with 5-40 thread screws to increase the area for the threaded rod to sit upon.

13. Mark a clearly visible line on the curved section of the threaded positioning stud, making it possible to count the number of rotations applied to the stud.

14. Repeat steps 5-13 for the other side of the assembly.

15. Use hot glue to affix the padding pulled from behind the heel in the AirCast to the inside of the PTB brace back half, covering the heads of the screws used to attach the wall mounts. This prevents the screw heads from rubbing against the leg of users of this device, and increases their comfort.

16. Using the Velcro straps provided, attach the PTB brace front half to the back half, and attach the footplate under the wide Velcro strap at the foot of the AirCast, as shown in Figure 21.

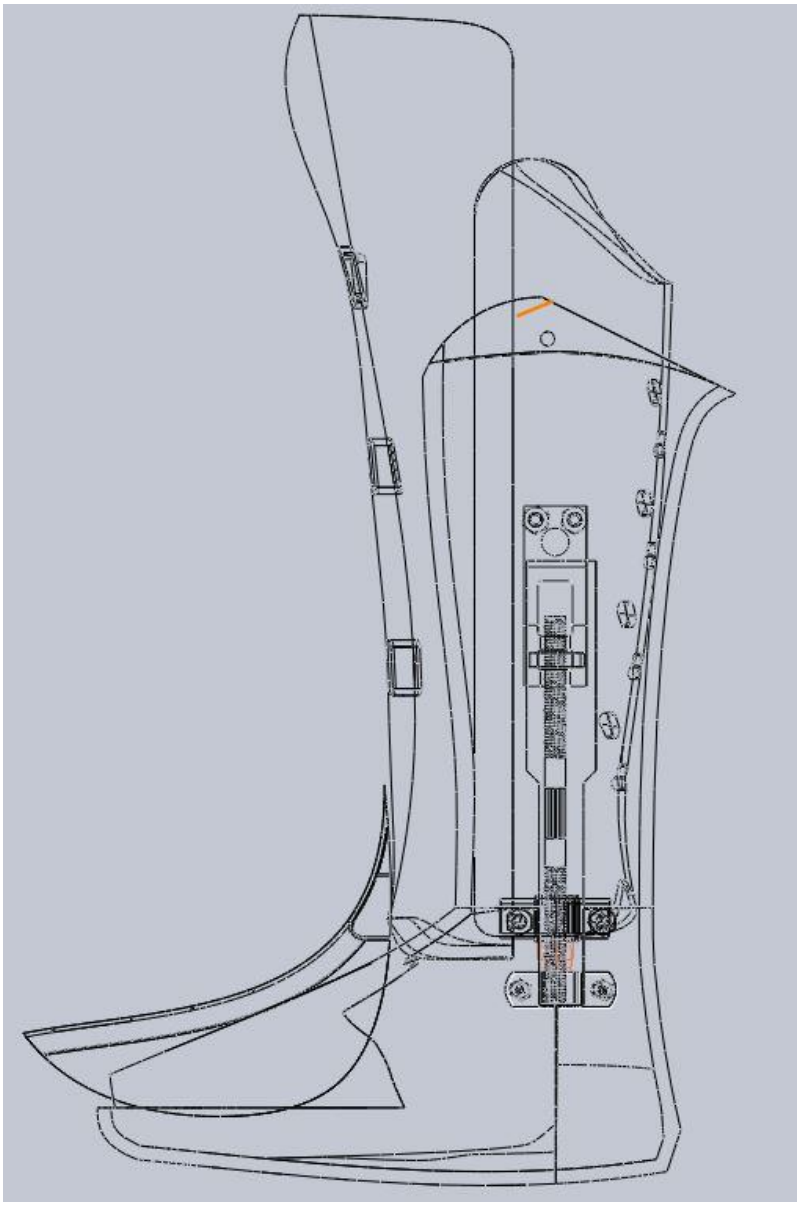

Figure 21 Design iteration 1 assembly

Design Iteration 2:

1. Drill ¼'' holes at the top of the modified AirCast body on both sides, as shown in Figure 19.

2. Use hot glue to attach the longest air bladder (behind the leg) from the original AirCast assembly to the interior back of the modified AirCast. The bottom of this bladder must reach the bottom of the interior of the boot when it is in its zero-position. Orient the bladder so that the valve is toward the top of the device.

Popliteal Brace Component and Repurposed AirCast Front Plate

1. Drill two ¼’’ holes 2 ½’’ from the bottom of the AirCast front plate as close to the edge as possible without compromising the structural integrity of the component. This separation should be at a minimum ¼’’ to the edge of the hole. These holes must be in identical positions on opposite sides of the component.

2. Cut a 0.3’’ slot through the back face of the boot with dimensions shown in Figure 22. Connect this slot to the nearest pre-existing vent in the plastic.

3. Cut two ¼’’ slots with on each side near the top of the component, using dimensions from Figure 22.

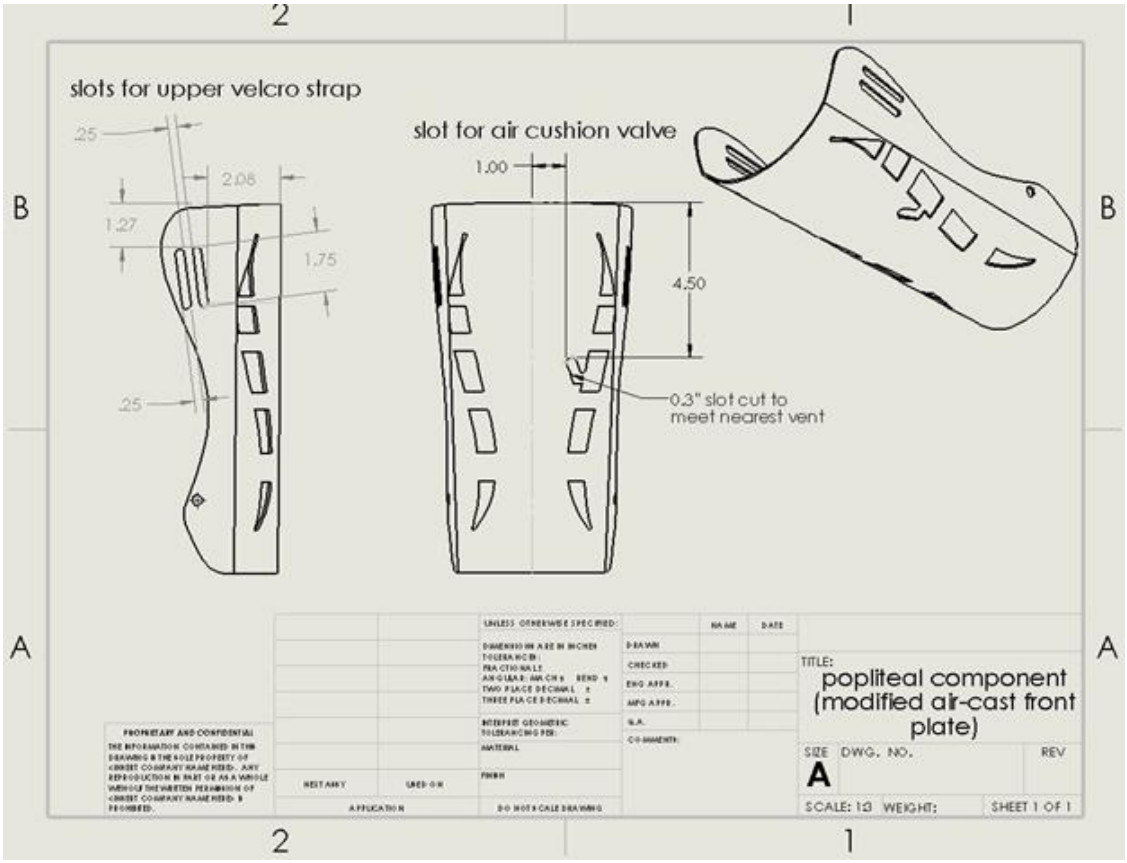

Figure 22 Popliteal (back of knee) brace component

Design Iteration 2 Assembly

1. Using two ¼-20 thread ½’’ steel hex head screws and matching nuts, secure the popliteal brace component to the AirCast body through the ¼’’ holes drilled near the top of the AirCast. The concave face of the popliteal brace component must be facing forwards (Figure 23).

2. Grab the air bladder valve, and run it from inside the brace, out through the large vent attached to the 0.3’’ slot, and then navigate the valve up into the slot so that the wider diameter portion rests outside of the device. This makes the valve accessible and prevents it from slipping back inside the boot.

3. Attach the foot protector plate and the PTB front half as in design iteration 1.

4. Using the Velcro from the removed PTB foot plate, run the Velcro around the back of the popliteal brace component, through all four slots, and then tightly around the PTB front half, securing it in the front.

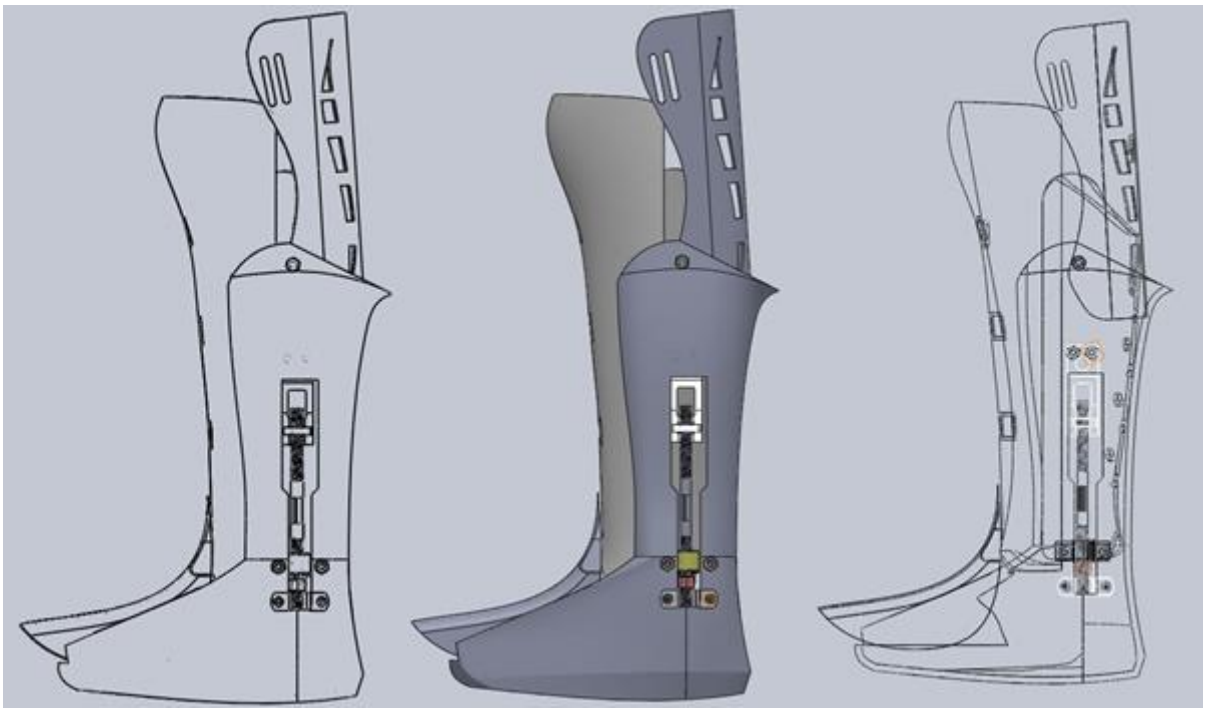

Figure 23 Three views of design iteration 2 assembly: line drawing, color render, and wireframe

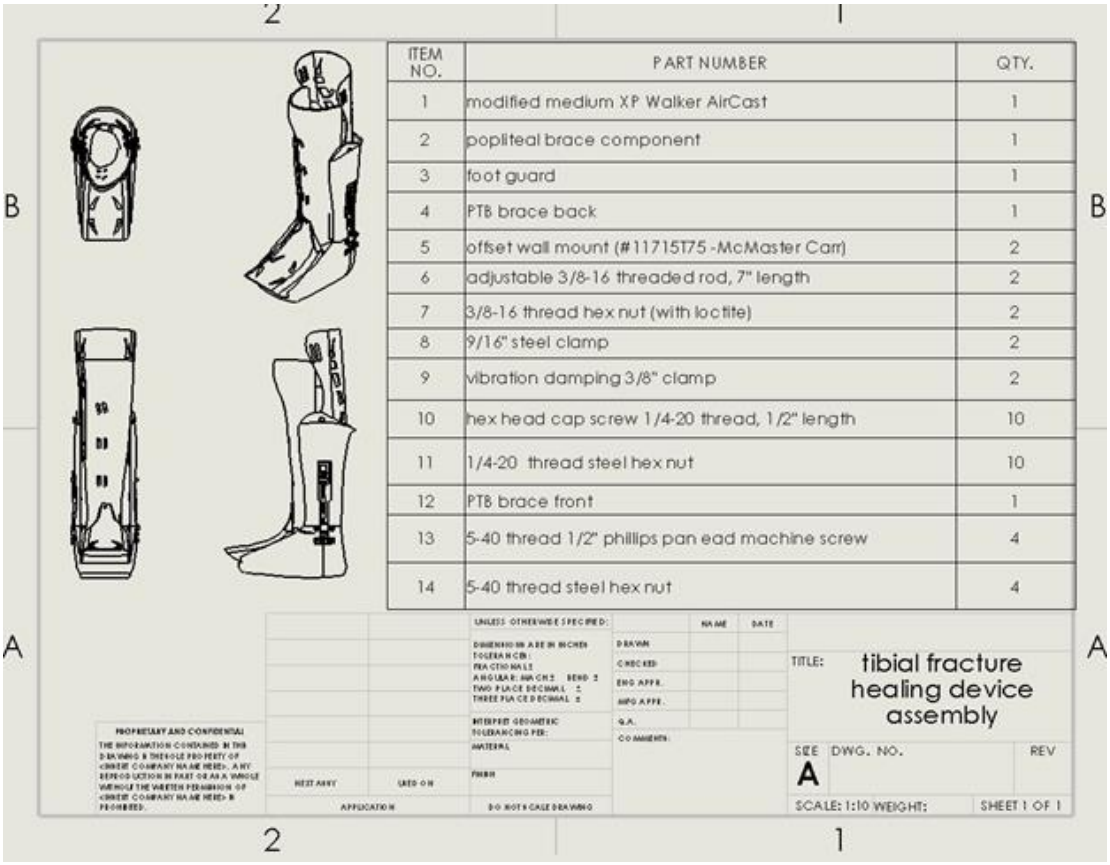

ITEM NO.	PART NUMBER	QTY.
1	modified medium XP Walker AirCast	1
2	popliteal brace component	1
3	foot guard	1
4	PTB brace back	1
5	offset wall mount (#11715T75 -McMaster Carr)	2
6	adjustable 3/8-16 threaded rod, 7" length	2
7	3/8-16 thread hex nut (with loctite)	2
8	9/16" steel clamp	2
9	vibration damping 3/8" clamp	2
10	hex head cap screw 1/4-20 thread, 1/2" length	10
11	1/4-20 thread steel hex nut	10
12	PTB brace front	1
13	5-40 thread 1/2" phillips pan ead machine screw	4
14	5-40 thread steel hex nut	4

Figure 24 Engineering drawing of the final design, accompanied by the bill of materials

3.2.1.2 Device Specifications

This section shows specifications important to the consumer of the finished device. This is general information necessary to understand the size of this device (Table 4).

Table 4: Finished Assembly Specifications

Left Foot PTB-Walking Brace Specifications	
Weight	4 lbs 1.1 oz
Overall Height	23.5''
Overall Width	5.25''
Overall Length (heel to toe)	11.5''
Adjustable Range	3 mm

3.2.2 Bone Analogue Material

The options for bone analogue material included purchasing a SawBone composite bone model, creating a polyurethane and epoxy molded bone, or utilizing animal bones obtained from a butcher shop. Table 5 identifies the mechanical properties and characteristics of the different materials for comparison with cortical and cancellous bone. Cortical and cancellous bones have a Young's modulus of approximately 20 GPa and 1 GPa respectively with a compressive strength of about 190 MPa. Based on cost and availability, we attempted to manufacture our own bones; the cancellous portion molded with polyurethane foam and the cortical portion formed by painting on epoxy resin. However, we choose to use a SawBone based on testing of the polyurethane bones created.

Table 5: Bone Analogue Matrix

Categories:	Cost	Modulus	Compressive Strength	Ductile/Brittle	Processing/Manufacturing	Cortical and Cancellous Characteristics	Comparison to Real Bone
Polyurethane		~12-1150 MPa based on the density of the foam	based on type range from ~1.5 – 50 MPa	N/A	supposedly easy to mold with a cortical bone analog like epoxy resin; also purchasable in a block form from Saw Bone	effective model for cancellous bone with either solid rigid PU foam or cellular rigid PU form	comparative to cancellous cadaver bone with providing a material with properties in same range but not able to replicate the structure
Epoxy/Fiberglass	~ $100 for basic supplies but bound to change based on quantity and quality required	~10 - 18 GPa based on the combination of materials	Varies between 150-190 MPa	Overly brittle, requires a correction factor	glass fibers and epoxy resin mixed then injection molded with silicone mold	model for cortical bone	similar to cortical bone with adjustable properties based on quantities of material
PEEK	Depends on where it is bought from, but roughly $100	3.5 GPa	120-300 MPa	close to cortical bone	tough to mold, might be commercially available	Cortical bone properties (not cancellous)	Similar to bone
BoneSim Products	Cortical: $120 (2-12 mm) -$360(40 mm) for packs of 3 Cancellous: Not listed	Cancellous: 42-425	Cortical: 110 MPa Cancellous: 3-25 MPa	Realistic to cortical and cancellous respectively	Come preformed in disks, no mold ability	Effective for cortical and cancellous bone	Very similar mechanical properties
Saw Bone Products	4th Generation Tibia Composite Bone: $174.0 each	Cortical Bone: 16.7 GPa Cancellous Bone: 155 MPa	Cortical: 157 MPa Cancellous: 6 MPa	N/A	Comes preformed in a realistic tibia shape with cortical and cancellous portions (injection molding manufacturing)	Cortical Bone composed glass fibers and epoxy resin, while cancellous bone solid rigid polyurethane foam	compares with mechanical behavior falling within range of human bone
Butcher Bone		Mechanical properties vary depending on the source of biological substitute bone. For comparison purposes bovine is mechanically similar to human bone.			N/A	Has both components	Cow bones have very similar properties compared to human bones

Process for Creating a Silicon Mold and Casting Bone Analogues:

Using a Por-a-Mold silicone material kit, we made a tibia mold negative with a basic SawBone tibia model for the correct shape. The tibia mold was created by pouring the mixed Por-a-Mold components into a PVC pipe containing a suspended Sawbone tibia model as seen in Figure 25. After the Por-a-Mold completely set, it was removed from the PVC pipe and cut to extract the tibia model. Appendix B contains the detailed procedure for the tibia negative Por-a-Mold. An alternative shape used to test the properties and abilities was a cylinder based on a tibia's cross sectional area size ("Procedure for Making a Silicone Molds," 1997).

Figure 25 Creating tibia mold with Por-a-Mold

The tibia bone analogue was created in two steps corresponding to the cancellous and cortical portion of the bone. First, the bone's cancellous portion was molded by pouring the mixed polyurethane foam with a funnel into the silicone mold. The total amount required to fill the mold cavity was calculated in pounds according to the manufacturer's conversion below:

$$\text{Total Pounds} = \text{Cavity Volume } (\text{ft}^3) * 2.5$$

Due to the irregular shape of the tibia bone, we had to approximate the cavity volume based on the PVC pipe securing the mold. Therefore, the cavity volume was estimated as 0.0726 cubic feet, half the PVC pipe's volume.

$$V_{cavity} = \frac{\pi r^2 h}{2} = \frac{\pi(2\text{ in})^2(20\text{ in})}{2} = 125.5\text{ in}^3 = 0.0726\text{ ft}^3$$

The manufacturer's conversion was then used:

$$\text{Total Pounds} = \text{Cavity Volume } (\text{ft}^3) * 2.5 = 0.0726\text{ ft}^3 * 2.5 = 0.01815\text{ lbs} = 82.3\text{ grams}$$

According to the manufacturer's recommendation, the total amount was divided equally between the two mixture parts (Part A and Part B), but with Part A obtaining slightly more than half. After the first bone analogue was created, the amount of polyurethane was decreased in future bone analogue creations to prevent overflowing of the mold.

The polyurethane foam was allowed to set for up to 30 minutes before removing the molded cancellous portion from the silicone mold (Figure 26). The removal process from the mold required spraying the inside of the model with a release agent prior to adding the polyurethane foam.

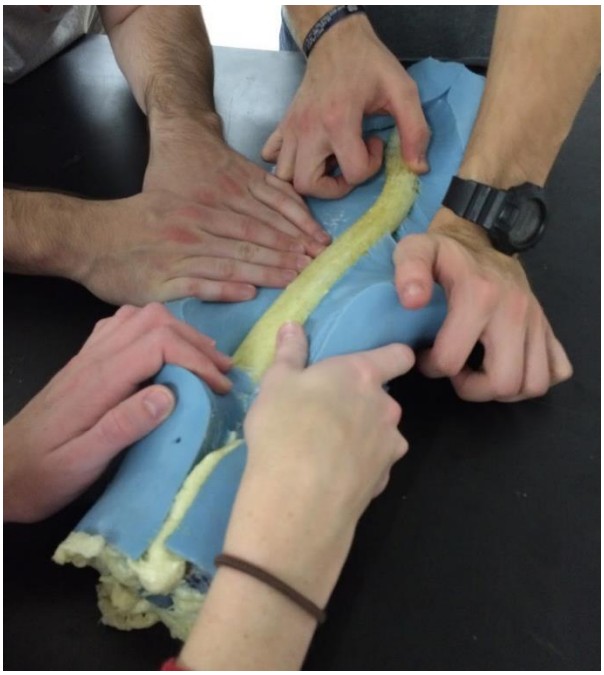

Figure 26 Polyurethane foam removal from mold

The second step was to apply the epoxy resin to simulate the cortical portion on the surface of the polyurethane foam. It was manually applied with a paintbrush in multiple coats to build thickness in the appropriate locations. After the final epoxy layer dried, the bone analogue was completed and ready to be tested for the mechanical properties according to the test in Section 3.4.1.

3.3 Numerical Analysis

The proof of concept for the final design and sequential design modifications was proven first with a numerical analysis utilizing ANSYS finite element modeling (FEM) software.

3.3.1 Pre-Analysis Calculations

Prior to a computer numerical analysis and physical testing, we quantified and calculated the required loads through force calculations and free body diagrams (FBD).

Force Required to Induce Strain Calculations

To find the force needed to induce a specific strain value, the following equations are modified and solved for force (F):

$$\sigma = \frac{F}{A} \text{ and } E = \frac{\sigma}{\epsilon}$$

$$\therefore F = E * \epsilon * A$$

The Young's modulus (E) for fracture callus was determined through research as 1GPa or 10^9 Pa (González-Torres et al., 2010). Based on the average tibia cross sectional area discussed in the background, 4 cm^2 or 0.0004 m^2 was used for the cross section.

To achieve a strain of 1000 microstrains or 0.001 strain, the required force was calculated as:

$$F = E * \epsilon * A = (10^9 \text{Pa}) * (0.001) * (0.0004 \text{m}^2) = 400 \text{N}$$

The corresponding force required to produce strain values ranging from 0 to 3000 microstrains were calculated and plotted in Figure 27 below.

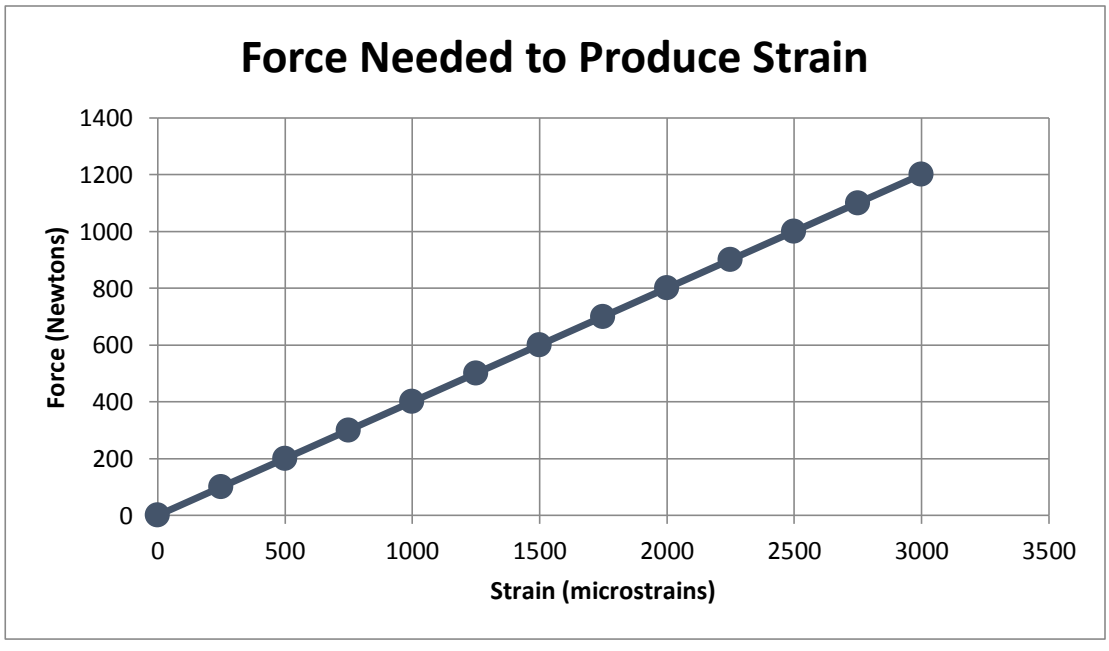

Figure 27 Forces required to induce strain value

Free Body Diagrams

In order to understand the forces and stresses applied on the tibia under varying conditions, we created and analyzed free body diagrams for the following instances during normal walking: heel strike, flat foot, and toe off.

For the scenarios, an average weight of 77 kg was assumed for the subject. The magnitude of the ground reaction force varies depending on the phase of walking. Heel strike and toe off experience 0.5 N/kg of the ground reaction force, and when the foot is flat, 11 N/kg of the ground reaction force is experienced as seen in Figure 28 (Winter, 1991). The corresponding ground reaction forces for a 77 kg person at each gait cycle phase are:

$$\text{Heel strike: } 0.5\ \frac{\text{N}}{\text{kg}} * 77\ \text{kg} = 38.5\ \text{N}$$

$$\text{Flat foot: } 11\ \frac{\text{N}}{\text{kg}} * 77\ \text{kg} = 847\ \text{N}$$

$$\text{Toe off: } 0.5\ \frac{\text{N}}{\text{kg}} * 77\ \text{kg} = 38.5\ \text{N}$$

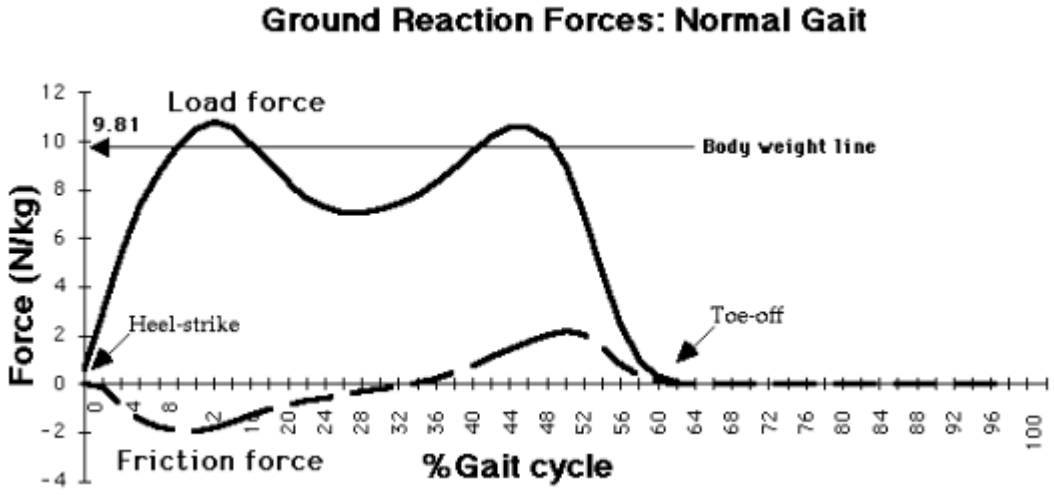

Figure 28 Forces during walking gait cycle (Winter, 1991)

The mass distribution of different body parts has been determined, and the mass of the total leg, thigh, leg, and foot, had been found using the average weight of 77 kg; both can be seen in Figure 29 (Winter, 2009). The mass distributions of the body segments for a 77 kg person were:

$$M = 77\text{kg} * 9.8\ \frac{m}{s^2} = 755\ N$$

$$\text{Total leg: } 0.161 * 755\ N = 122\ N$$

$$\text{Thigh: } 0.100 * 755\ N = 75.5\ N$$

$$\text{Leg: } 0.0465 * 755\ N = 35.1\ N$$

$$\text{Foot: } 0.0145 * 755\ N = 10.9\ N$$

Table 3.1 Anthropometric Data

Segment	Definition	Segment Weight/ Total Body Weight	Center of Mass/ Segment Length		Radius of Gyration/ Segment Length			Density
			Proximal	Distal	C of G	Proximal	Distal	
Hand	Wrist axis/knuckle II middle finger	0.006 M	0.506	0.494 P	0.297	0.587	0.577 M	1.16
Forearm	Elbow axis/ulnar styloid	0.016 M	0.430	0.570 P	0.303	0.526	0.647 M	1.13
Upper arm	Glenohumeral axis/elbow axis	0.028 M	0.436	0.564 P	0.322	0.542	0.645 M	1.07
Forearm and hand	Elbow axis/ulnar styloid	0.022 M	0.682	0.318 P	0.468	0.827	0.565 P	1.14
Total arm	Glenohumeral joint/ulnar styloid	0.050 M	0.530	0.470 P	0.368	0.645	0.596 P	1.11
Foot	Lateral malleolus/head metatarsal II	0.0145 M	0.50	0.50 P	0.475	0.690	0.690 P	1.10
Leg	Femoral condyles/medial malleolus	0.0465 M	0.433	0.567 P	0.302	0.528	0.643 M	1.09
Thigh	Greater trochanter/femoral condyles	0.100 M	0.433	0.567 P	0.323	0.540	0.653 M	1.05
Foot and leg	Femoral condyles/medial malleolus	0.061 M	0.606	0.394 P	0.416	0.735	0.572 P	1.09
Total leg	Greater trochanter/medial malleolus	0.161 M	0.447	0.553 P	0.326	0.560	0.650 P	1.06

Figure 29 Mass distribution for leg (Winter, 2009)

The mass distributions for the different parts of the leg were used to calculate the joint reaction force at the knee for the different stages of the gait cycle. The angle of the leg at heel strike and toe off was found in previous research to be 23° and -8° to the vertical respectively. The acceleration of the leg during walking was assumed to be 1 m/s (Umberger & Martin, 2007).

Based on the average male, the following assumptions about the lengths and weights were used in the calculations and can be seen below (De Leva, 1996).

$$\text{Average height: } 1.76 \text{ m}$$

$$\text{Average length of lower leg: } 0.247 * 1.76 \text{ m} = 0.435 \text{ m}$$

$$\text{Location of center of gravity for lower leg from knee: } 0.434 * 0.435 \text{ m} = 0.189 \text{ m}$$

$$\text{Location of center of gravity for foot from ankle: } 0.50 * 0.075 \text{ m} = 0.038 \text{ m}$$

$$\text{Average weight: } 77 \text{ kg} * 9.81 \frac{\text{m}}{\text{s}^2} = 755 \text{ N}$$

$$\text{Segmental weight of lower leg: } 0.0465 * 755 \text{ N} = 35.1 \text{ N}$$

$$\text{Segmental weight of foot: } 0.0145 * 755 \text{ N} = 10.9 \text{ N}$$

For a 77 kg subject, a force of 931 N was applied through the leg during heel strike as seen in the free body diagram (Figure 30) and calculations.

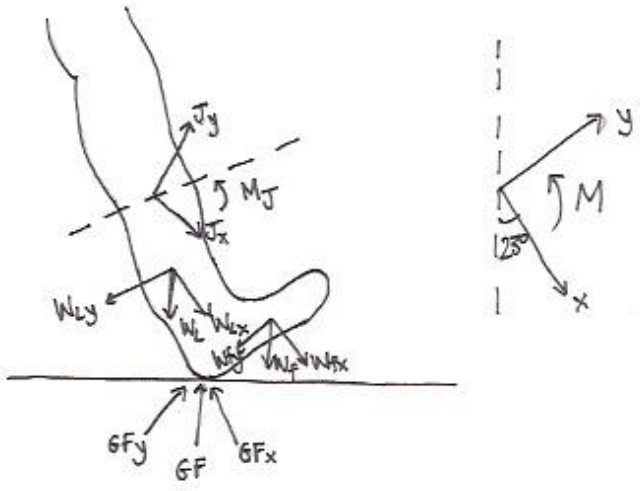

Figure 30 Free body diagram for joint reaction force during heel strike

$$\sum \text{F}_\text{x} = \text{ma}_\text{x} = \text{J}_\text{x} + \text{W}_\text{Lx} + \text{W}_\text{Fx} - \text{GF}_\text{x}$$

$$(77 \text{ kg}) \left(1 \frac{\text{m}}{\text{s}^2}\right) \cos(23) = \text{J}_\text{x} + (35.1 \text{ N}) \cos(23) + (10.9 \text{ N}) \cos(23) - (38.5 \text{ N}) \cos(23)$$

$$J_x = 930.0\ \text{N}$$

$$\sum F_y = ma_y = J_y - W_{Ly} - W_{Fy} + GF_y$$

$$(77\ \text{kg})\left(1\frac{\text{m}}{\text{s}^2}\right)\sin(23) = J_y - (35.1\ \text{N})\sin(23) - (10.9\ \text{N})\sin(23) + (38.5\ \text{N})\sin(23)$$

$$J_y = 33.0\ \text{N}$$

$$J = \sqrt{J_x^2 + J_y^2}$$

$$J = \sqrt{(930.0\ \text{N})^2 + (33.0\ \text{N})^2}$$

$$J = 931\ \text{N}$$

$$\sum M = M_J - W_{Ly}(0.189\ \text{m}) + GF_y(0.435\ \text{m}) - W_{fy}(0.435\ \text{m}) - W_{fx}(0.038\ \text{m}) = 0$$

$$\sum M = M_J - (35.1\ \text{N})\sin(23)\,(0.189\ \text{m}) + (38.5\ \text{N})\sin(23)(0.435\ \text{m}) - (10.9\ \text{N})\sin(23)(0.435\ \text{m}) - (10.9\ \text{N})\sin(23)(0.038\ \text{m}) = 0$$

$$M_J = -1.72\ \text{N}\cdot\text{m}$$

During toe off the subject would experience 69.5 N of force at the end of a walking cycle, and the calculations can be seen below (Figure 31).

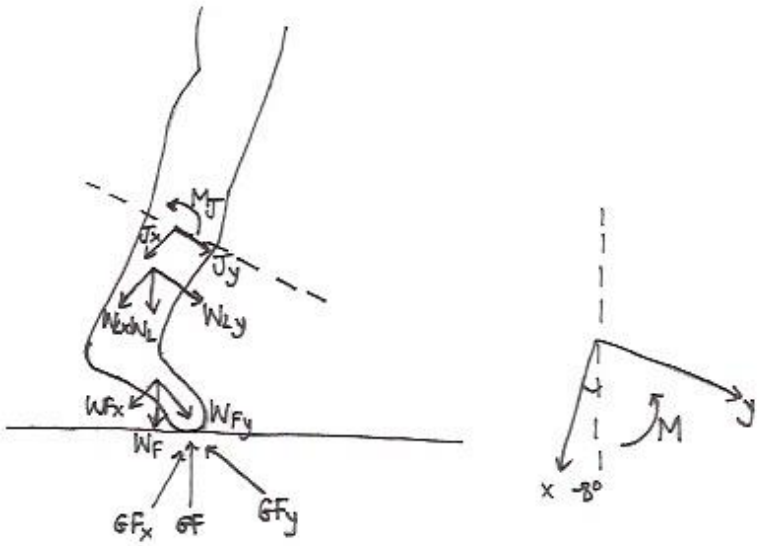

Figure 31 Free body diagram of the joint reaction force during toe off

$$\sum F_x = ma_x = J_x + W_{Lx} + W_{Fx} - GF_x$$

$$(77\text{ kg})\left(1\ \frac{m}{s^2}\right)\cos(-8) = J_x + (35.1\text{ N})\cos(-8) + (10.9\text{ N})\cos(-8) - (38.5\text{ N})\cos(-8)$$

$$J_x = 68.8\text{ N}$$

$$\sum F_y = ma_y = J_y + W_{Ly} + W_{Fy} - GF_y$$

$$(77\text{ kg})\left(1\frac{m}{s^2}\right)\sin(-8) = J_y + (35.1\text{ N})\sin(-8) + (10.9\text{ N})\sin(-8) - (38.5\text{ N})\sin(-8)$$

$$J_y = -9.67\text{ N}$$

$$J = \sqrt{J_x^2 + J_y^2}$$

$$J = \sqrt{(68.8\text{ N})^2 + (-9.67\text{ N})^2}$$

$$J = 69.5\text{ N}$$

$$\sum M = M_J - W_{Ly}(0.189\text{ m}) + W_{fx}(0.038\text{ m}) - W_{fy}(0.435\text{ m}) + GF_x(0.075\text{ m}) - GF_y(0.435\text{ m}) = 0$$

$$\sum M = M_J - (35.1)\sin(-8)(0.189\ \text{m}) + (10.9\ \text{N})\cos(-8)(0.038\ \text{m}) - (10.9\ \text{N})\sin(-8)(0.435\ \text{m}) + (38.5\ \text{N})\cos(-8)(0.075\ \text{m}) - (38.5\ \text{N})\sin(-8)(0.435\ \text{m}) = 0$$

$$M_J = -1.69\ \text{N} \cdot \text{m}$$

When the foot was flat on the ground, the force experienced by the leg was 724 N. The free body diagram (Figure 32) and calculations are shown below.

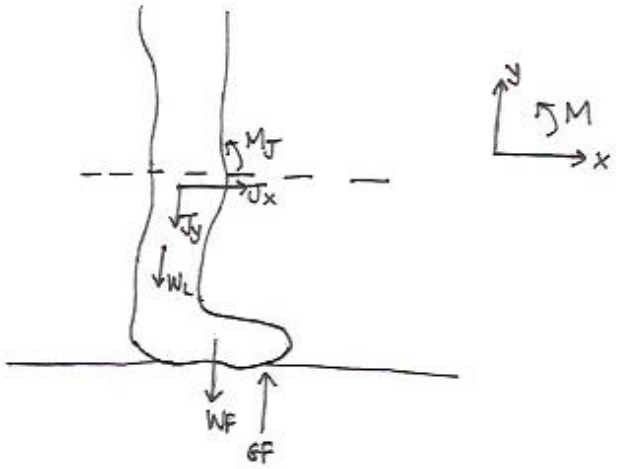

Figure 32 Free body diagram of the joint reaction force when flat footed

$$\sum F_x = ma_x = J_x$$

$$(77\ \text{kg})\left(1\frac{\text{m}}{\text{s}^2}\right) = J_x$$

$$J_x = 77\ \text{N}$$

$$\sum F_y = ma_y = -J_y - W_L - W_F + GF$$

$$(77\ \text{kg})\left(1\frac{\text{m}}{\text{s}^2}\right) = -J_y - 35.1\ \text{N} - 10.9\ \text{N} + 847\ \text{N}$$

$$J_y = 724\ \text{N}$$

$$J = \sqrt{J_x^2 + J_y^2}$$

$$J = \sqrt{(77\ \text{N})^2 + (724\ \text{N})^2}$$

$$J = 728\ \text{N}$$

$$\sum M = -W_f(0.038\ \text{m}) + GF(0.075\ \text{m}) + M_J = 0$$

$$M_J = 63.1\ \text{N} \cdot \text{m}$$

3.3.2 Computer Modeling

After pre-analysis, ANSYS software was used to simulate the load applications for inducing strain on a tibia. A static structural analysis was performed on two types of geometries: a cylinder and a tibia bone. The cylinder model was created in ANSYS as a 380 mm long cylinder with a 2.54 cm (1 in) outer diameter (d_o) and 1 cm inner diameter (d_i) to simulate the SawBone tibia. The medullary cavity was simulated with the 1 cm hole that spanned the entire length for simplification. The tibia model was a SOLIDWORKS file downloaded from 3D Content Central and converted to a parasolid file for ANSYS compatibility (Ardatov, 2006). It was 350 mm long with an approximate 2 cm outer diameter (d_o) and 1 cm medullary cavity inner diameter (d_i) at the center of the shaft. Each model was modified to simulate a fracture in the shaft by cutting the models in half and inserting a 1 mm thick shape to simulate the callus.

For material properties, we assumed the bone was isotropic with the same Young's modulus and Poisson's ratio compared to the reality of bone being anisotropic. Both the cylinder and tibia were assigned properties to simulate a real bone (Young's modulus of 10 GPa), the SawBone (Young's modulus of 1.5 GPa), and the bone analogue made of polyurethane and

epoxy (Young's modulus of 0.4 GPa). The Poisson's ratio was 0.4 for each simulation at 10 GPa, 1.5 GPa, and 0.4 GPa.

The top of the cylinder model (Figure 33) and the tibia model (Figure 34) were fixed to simulate the restricted mobility of the knee, and a compressive force was applied at the bottom face to simulate a load applied during walking. A 400 N compressive force was used in the analysis for each set of material properties. Additionally, a point load was simulated with a 400 N compressive nodal force applied to half of the bottom face for each model.

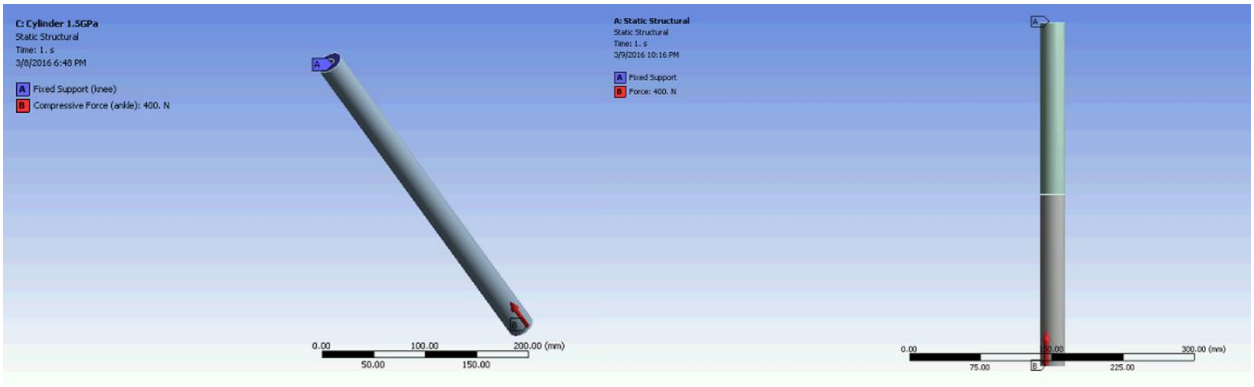

Figure 33 Load application on cylinder model in ANSYS

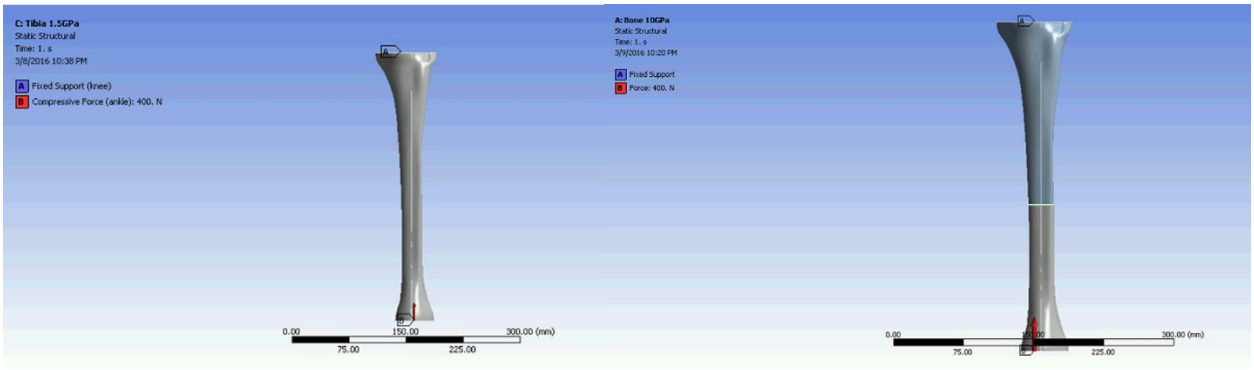

Figure 34 Load application on tibia model in ANSYS

The total deformation, normal stress, and normal elastic strain were analyzed for an unbroken and fracture configuration of each model at all three Young's modulus values. Then, calculations were performed for the cylinder model to validate the ANSYS model results for the material properties prior to using the tibia model.

3.4 Testing

A physical model of the device was tested with both a sample bone analogue and a fit test on a real person. The group created a three step testing process to verify the working condition of the brace. The testing process verified that the brace correctly reduced force, and brace reduced force transmission through the tibia. Each successful test led into the next in a logical progression. Test 1 measured the bone analogue's mechanical properties to compare to cortical bone. Test 2 used an air cylinder to determine how much strain resulted from applied force to the tibia. Test 3 was a walking test to measure the force dampening ability of the boot on a real subject. Finally, Test 4 was a combination of previous tests to test the boot with a fractured bone analogue. With these tests, we confirmed the mechanical properties of the bone, the transmission of force into strain, the force dampening of the boot, and the dampened force transmission into the desired strain. Based on the results of the testing, the functional walking brace was adjusted and retested to optimize healing conditions.

3.4.1 Test 1: Bone Analogue Mechanical Properties Test

This lab test was conducted to confirm the bone analogue mechanical properties were similar to actual bone. The target range for the Young's modulus was 1 to 20 GPa. An Instron 5544 (Figure 35) was used to test the properties of each bone analogue with a three-point bending test. Additionally, this test created the desired transverse fracture break through the shaft on the bone analogues.

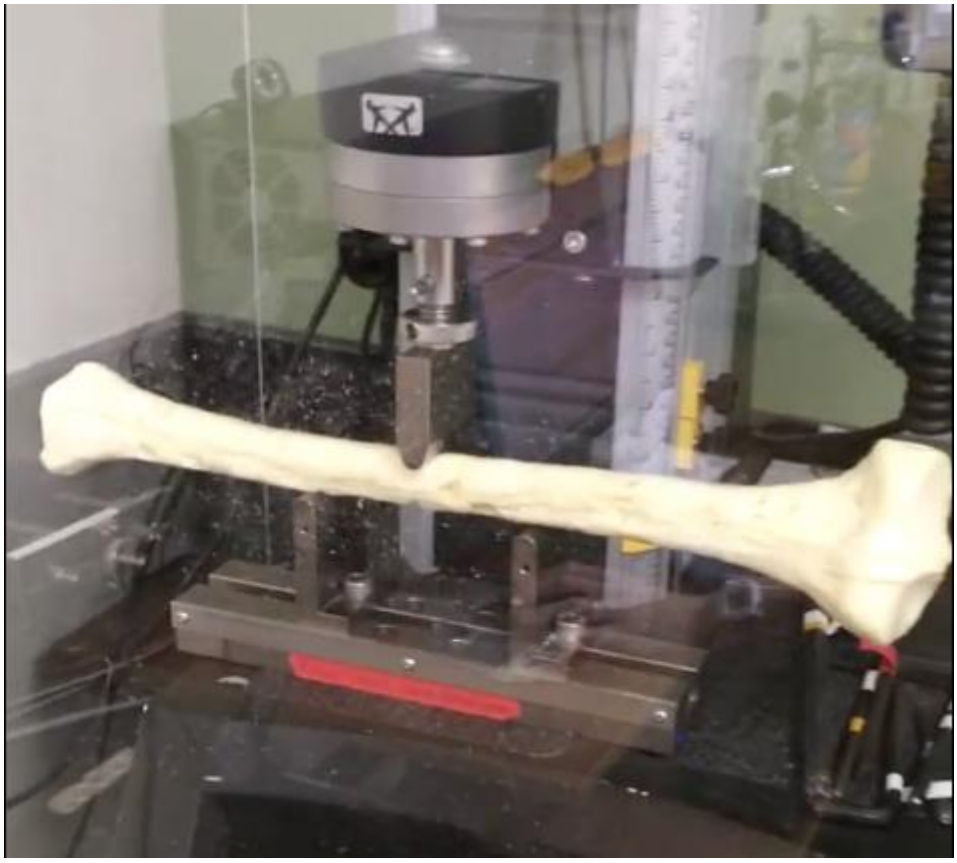

Figure 35 A SawBone set up in the Instron 5544

Test Procedure:

1. Open and log into Bluehill software
2. Calibrate transducer
3. Set physical stoppers on Instron
4. In Bluehill, choose methods and under Instron examples choose flexure examples
5. Using the tabs on the left set the following specifications:
    (a) Set units to SI
    (b) Geometry dimensions- circular
        (i) Enter diameter of sample
        (ii) Enter support span of bottom piece the sample is resting on

(c) Measurements: add time, extension, load, flexure strain (extension), flexure extension, flexure stress to the box of what will be shown when the results are exported

(d) Test control

(i) Test: Control mode 1: extension= rate of 50 mm/min

(ii) End of test

1. Criteria 1: Rate of load: 40%
2. Criteria 2: Extension: 20 mm

(iii) Data

1. Measurement 1: Time: 50 ms

(e) Results- Columns

(i) Maximum slope (Automatic Young's)

1. Add maximum slope to selected results

(ii) Maximum flexure stress

1. Flexure strain (extension)

(iii) Raw data

1. Add flexure strain (extension) and flexure stress

(f) Export

(i) When exporting raw data, add in specimen properties to exported worksheet

6. After inputting the above details, save the test method
7. Return to the Bluehill test screen and click on Test

8. Measure the diameter of the specimen and the support span and input the information into Bluehill
9. Load the specimen into the Instron
10. Place the safety shield in front of the machine
11. Apply a 5 N tare load to the specimen (this is done to ensure accuracy of the measurements given the 2000 N load cell)
12. Run the test
13. The load is applied to the sample at a rate of 50 mm/min
14. When the sample breaks, the Instron will return to the starting position
15. Click “Finish” in Bluehill to save and export the data

3.4.2 Test 2: Axial Compressive Force Test on Bone Analogue

The objective of this test was to prove that an applied force, less than 400 N, on the bone analogues would generate the desired microstrain, 1000 - 2000 microstrain, on a broken bone. To accomplish this goal, the group designed a simple static load compressive test that used a BIMBA SR-174-P-00MC air cylinder to apply a force on the top of the bone.

The test rig (Figure 36) was constructed of Superstrut P-1400-HS and Superstrut A-1200-HS channeled metal framing. Two 24-inch-long feet provided stability for the entire rig, and two vertical bars 30 inches in length provided support for the mounted air cylinder. Single crossbars on the feet and vertical sections provided a platform for the base plate and stability from the entire rig twisting under torsion. A PVC tube was secured on top of the base plate in which the bone was placed during testing. The air cylinder force was transmitted to the bone through a PVC pipe end cap held on top of the bone.

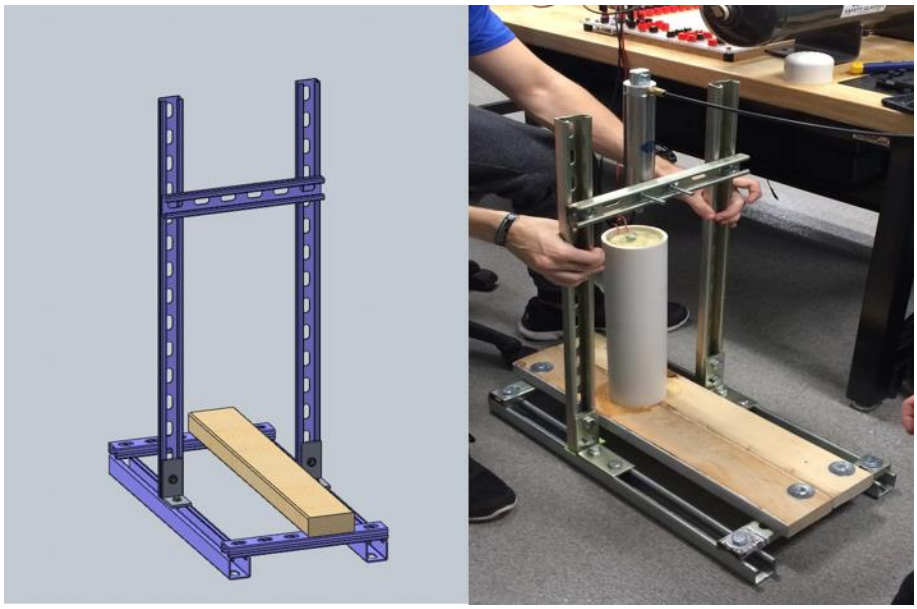

Figure 36 Test rig frame in SOLIDWORKS (left) and constructed (right)

A BIMBA SR-174-P-00MC air cylinder with a 1.5 inch bore piston diameter was used to complete all of the compressive tests. The air cylinder was used to test the bone analogues at 50 N force intervals from 100 N to 400 N. This force range was chosen based on previous calculations that determined under real cortical bone properties 400 N would produce the desired 1000 microstrain. However, the bone analogues had lower material properties so the test was performed for forces below 400 N. The pressure (P) was calculated in Pascals (Pa) for each force (F) and converted to pounds per square inch (psi), according to the below equation:

$$P = \frac{F}{A} = \frac{F}{\pi\left(\frac{d^2}{4}\right)}$$

$$P = \text{gauge pressure (Pa)}$$

$$F = \text{force exerted (N)}$$

$$A = \text{full bore area } (m^2)$$

$$d = \text{full bore piston diameter (m)}$$

In Table 6, the gauge pressures for the air cylinder from 100 N to 400 N forces are presented. At 400 N, the required gauge pressure was calculated to be 50.9 psi.

$$P = \frac{400\ \text{N}}{\pi\left(\frac{(0.0381\ \text{m})^2}{4}\right)} * 0.000145\,\frac{\text{psi}}{\text{Pa}}$$

$$P = \ 50.9\ \text{psi}$$

Table 6: Air Cylinder Pressures

Force (N)	Pressure (psi)
100	12.7
150	19.1
200	25.4
250	31.8
300	38.2
350	44.5
400	50.9

A standard foil strain gauge was attached with Loctite super glue at the artificial bone fracture site (Figure 37) to experimentally measure the strain induced on the bone analogue.

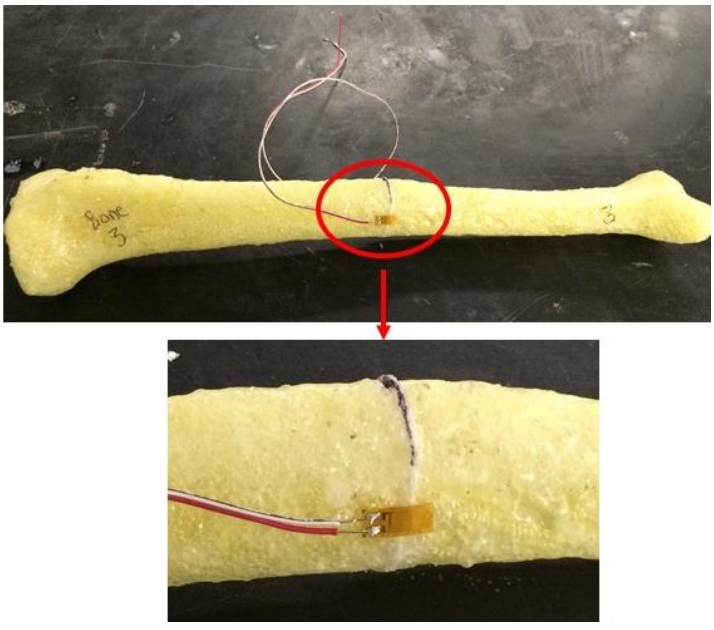

Figure 37 Strain gauge location on bone analogues

Based on our temperature, expected strain, and desired strain gauge size, the Vishay Intertechnology Inc. strain gauge selection table recommended a general dynamic linear strain gauge. We chose to use a CEA linear strain gauge with a ±1500 microstrain strain level, 120 Ohm gauge resistance, and 2.14 gauge factor ("Strain Gage Selection," 2014).

A LabVIEW data acquisition program was used to record the calibrated microstrain. The following test procedure was followed for testing each polyurethane and epoxy bone analogue and the SawBone. Multiple tests were performed for the SawBone to determine repeatability.

Test Procedure:

1. Place bone analogue into PVC tube on test rig
2. Attach strain gauge wires to DAQ box setup
3. Attach air cylinder to air tank using a t-valve
4. Use LabVIEW data acquisition program to calibrate strain gauge using three shunt resistors (10 kOhm, 22 kOhm, 90 kOhm) to obtain a slope and intercept value
5. Fill air tank to 12.7 psi to simulate a 100 N force
6. Start recording LabVIEW data acquisition program to obtain microstrain prior to load application
7. While holding the PVC end cap below the air cylinder, activate air cylinder
8. Continue recording data in LabVIEW for microstrain after load application
9. Retract air cylinder
10. Stop recording data in LabVIEW
11. Analyze data and calculate microstrain:

    microStrain = Average microStrain After Loading - Average microStrain Before Loading
12. Repeat steps 5-11 for each remaining pressure (150 N to 400 N)

3.4.3 Test 3: Functional Walking Brace Force Test

The purpose of this test was to prove the functional walking brace would reduce walking force on the tibia to a specific load by adjusting the gap between the foot and the insole of the boot. We accomplished this task by attaching force sensors to the bottom of the subject's foot to measure the force transmission through the foot and thus the tibia. Based on a comparison of price and largest surface area, 25.4 mm, with other force sensors, the Tekscan Flexiforce A401 Sensors (Figure 38) were chosen.

Figure 38 FlexiForce A401 force sensor ("FlexiForce A401," 2014)

Test Procedure:

1. Attach three Tekscan Flexiforce A401 Sensors on the ball (Sensor 1), outside (Sensor 2), and heel (Sensor 3) of the test subject's foot as seen in Figure 39.

Figure 39 Force sensor locations on foot (bottom view)

2. Construct the manufacturer recommended op-amp circuit (Figure 40), by using a 20 kOhm reference resistor (R_F), a -1.5V excitation voltage (V_T), and 10 V power to the op-amp. We adjusted the sensitivity of our force sensors by changing the reference resistor value within the recommended 1 kOhm to 100 kOhm range.

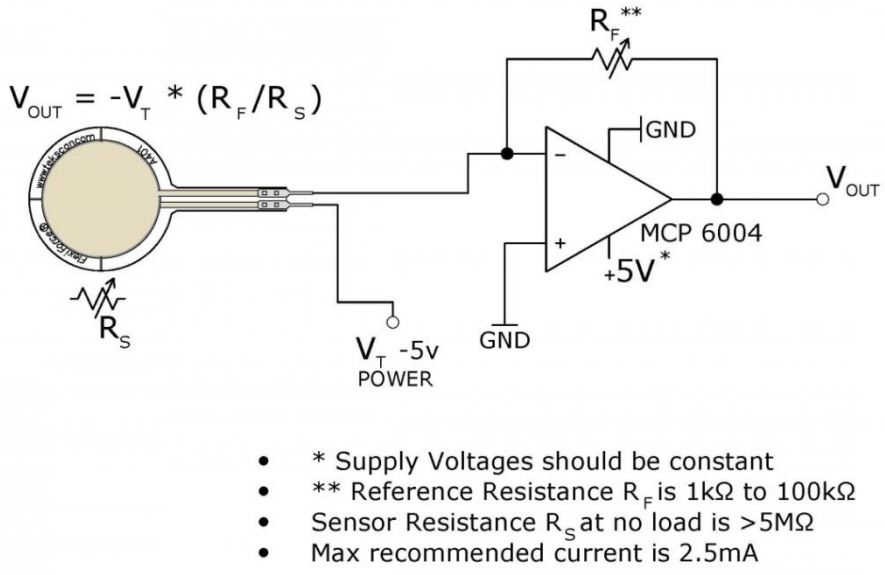

Figure 40 Circuit diagram for force sensor ("FlexiForce A401," 2014)

Insert the force sensor wires into the three locations identified on the breadboard circuit in Figure 41. Connect the 10 V power, 1.5 V force sensor excitation voltage, ground, and each sensor output to the Data Acquisition (DAQ) box.

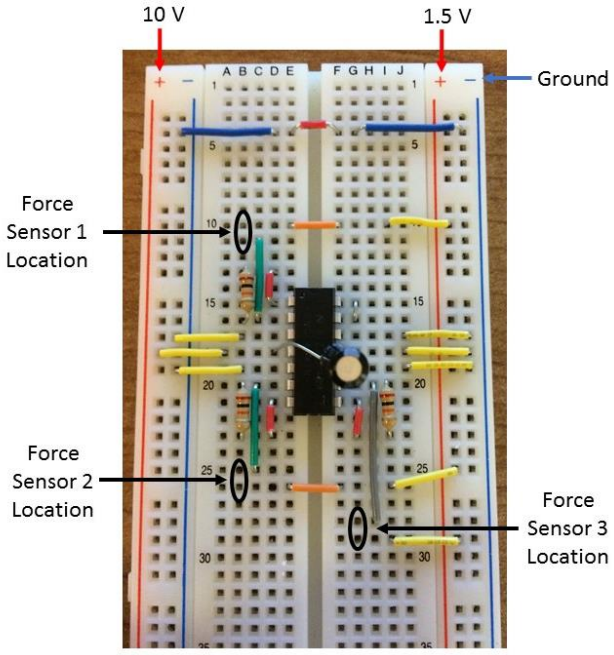

Figure 41 Breadboard circuit for force sensor set up

3. Place known weight on each sensor (15, 25, and 40 lbs), and record voltage output for each sensor.
4. Generate graph to curve fit data in Excel using a liner fit to obtain the line equation, see Figure 42 for Force Sensor 1 curve fit data example.

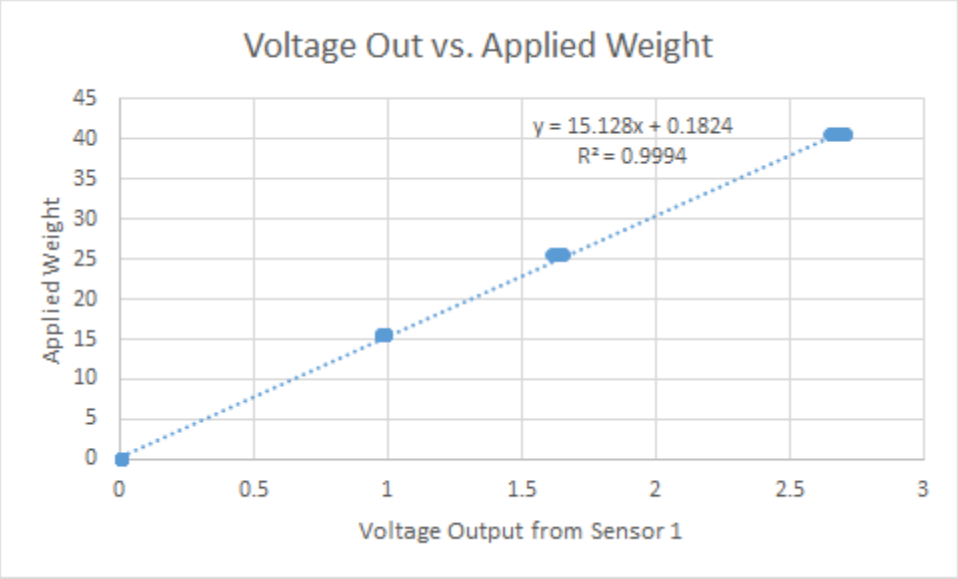

Figure 42 Calibration data and equation for Force Sensor 1

5. Generate data by having the subject walk a short distance with the functional walking brace on.
6. Data was recorded as voltage, and converted to pressure in psi using the calibration curve of each sensor, with an area of 1 in^2.
7. Convert psi to pound force (lbf) by multiplying the force sensor output by the area of specific region of foot.
8. Multiple by pound force (lbf) to Newton (N) conversion factor (4.44822).
9. Graph data for visualization and comparison.

3.4.4 Test 4: Cumulative Device Validation Test

Test 4 was a cumulative test to prove that the device prototype was effective in applying the correct strain through a tibia surrounded by the muscle and tissues within a human leg. It combined Test 2, the compressive force test for bones, and Test 3, the walking force test for the

device. Since we could not attach a strain gauge to a human tibia in-vivo, an analogue leg was used. The artificial leg was constructed from the following:

- The most representative tibia analogue with an artificial fracture consisting of a $^{1}/_{16}$" flexible polyurethane disk and a strain gauge installed across the callus.
- Epoxy resin coated polyurethane structures to simulate the general structure of the bones in the foot, the patella, and the distal end of the femur.
- Ballistics gel to simulate the muscles and tissues holding all these components together. Ballistics gel, a Knox gelatin based material, intended to mimic the shape of a human leg for load distribution across bottom of foot.

The leg was cast in a plaster mold taken from our human test subject's leg to ensure it fit our prototype. We wrapped the artificial leg in plastic wrap to help it maintain its structure after it was removed from the mold.

To perform the test, we gathered data from both the strain gauge on the fractured tibia inside of our artificial leg, and from force sensors attached to the bottom of the foot while the leg was secured in our device prototype. The prototype and the leg were placed in the air cylinder test rig, which had been modified to accommodate their size. Then, we applied a known force using the air cylinder on top of the artificial leg with the bottom of the boot held steady.

Test Procedure:

1. Prepare leg cast with suspended structures:
    a. Suspend broken SawBone tibia with artificial callus inside leg mold using nails through the outer cast material.
    b. Route wires from strain gauge out through the cast, and cover the strain gauges with hot glue to seal them.

c. Place simulated foot and distal femur (polyurethane) bone structures in the cast in their appropriate positions relative to the cast contours and the suspended tibia.
d. Suspend polyurethane structures within the cast; anchor them off the tibia model using nails. Take care to prevent them from floating in liquid ballistics gel when poured.
e. Use hot glue to seal the seam between the two halves of the plaster cast, and around any nails or wires where they protrude from the plaster cast.

2. Seal around the plaster cast with plastic wrap to prevent liquid ballistics gel from escaping.
3. Mix and prepare the ballistics gel:
    a. Combine water and Knox gelatin powder in a large container. Add 8 oz. of water per each 1 oz. of powder.
    b. Thoroughly mix the gelatin powder and water to break up any clumps of gelatin. Let the mixture chill and hydrate in the refrigerator.
    c. Once the gelatin is chilled and in solid form remove it from the refrigerator, and melt it down in a pan. Stir continually to reduce the amount of air trapped in the gelatin.
    d. Remove the pan from the heat source, and use a funnel to pour it into the leg cast. Proceed slowly, looking for leaks in the cast and sealing any that may occur.
    e. Once filled, carefully place the cast back in the refrigerator. Allow it to chill, undisturbed, for 36 hours.
4. Gently remove the ballistics gel leg analogue from the cast and cut away excess ballistics gel.

5. Using plastic wrap, tightly wrap the ballistics gel leg, taking extra care to stabilize the ankle and the knee. Cut a small hole in the plastic wrap to lead the strain gauge wires away from the model leg as seen in Figure 43.

Figure 43 Ballistics gel leg model with suspended bone structures supported with plastic wrap

6. Using tape, attach the three force sensors to the ballistics gel foot model (Figure 44), in the same spots used in Test 3: the heel, outside of the foot, and ball of the foot.

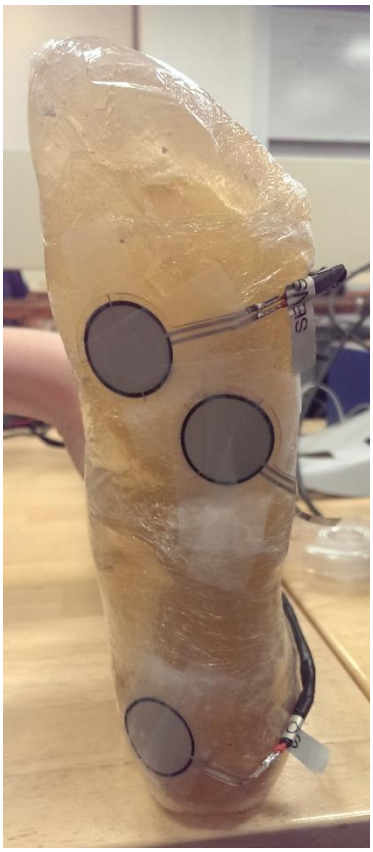

Figure 44 Force sensor placement on ballistics gel leg model

7. Place leg in brace prototype as shown in Figure 45, with the brace adjusted to no gap, so that the leg may be secured while the heel rests upon the bottom of the brace. Take care to secure the ballistics gel leg tightly. Route all wires out the top of the boot.

Figure 45 (a) Placement of leg model in the device over gap measurement padding and (b) a top view of the leg model inside the brace

8. This test was performed at a gap height of 0 mm and 8 mm below the heel, without removing the leg from the brace. This represents our control test, and the 8 mm gap, which was determined to be our optimal gap size. Take off the front PTB plate and lay the boot sideways to adjust the gap size. Place the appropriate amount of padding in the bottom of the boot once it has been adjusted to the specified gap height. Test for each iteration, beginning with no gap.
9. Adjust the Test 2 rig and air cylinder assembly so that the device and ballistics gel leg assembly can fit between the wooden platform, and the air cylinder bolt. This entails first removing the PVC tube used to hold the bone analogues in place, then removing the bolts

through the top metal crosshead on the rig that holds the air cylinder, and bolting it in at the top position on the vertical metal rails. This test rig modification is shown in Figure 46.

10. Fixated the leg with the brace on it vertically between the test rig's wooden platform and air cylinder rod attachment. The PVC air cylinder cap should cover the driven pneumatic component so as to apply a compressive force to the leg/brace assembly when the cylinder is pressurized, as seen in Figure 46.

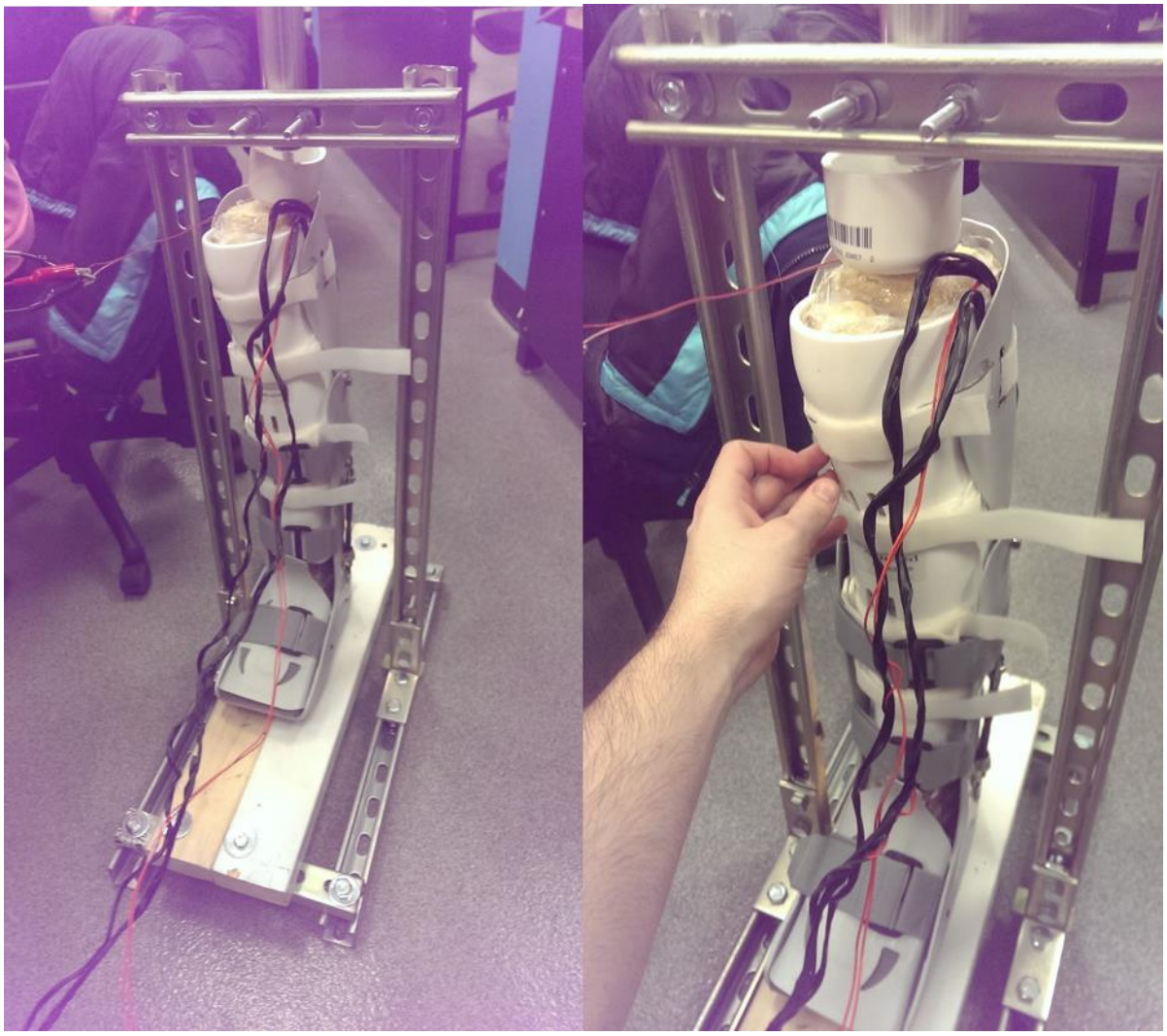

Figure 46 Device positioning in modified test rig

11. Connect the strain gauge wires and the force sensors to the respective circuit boards in the same manner as in Test 2 and 3. Verify that all are calibrated and in proper working order.
12. Attach the air cylinder on the test rig to the air supply.
13. Pressurize the tank to 60 psi while keeping the line to the air cylinder closed.
14. Begin recording data in LabVIEW programs for both the tibia strain gauge and the force sensors.
15. Hold the PVC end cap vertically, and gradually open up the valve to the air cylinder to apply a compressive force to the artificial leg in the prototype.
16. Let the air vent gradually from the cylinder, and release compression on the leg. Check to make sure that the leg model has not deformed, or slipped downward in the boot. If it has moved, reorient it to its proper gap height before the next test.
17. Repeat steps 13-16 two more times.
18. Stop both LabVIEW programs from recording. Save the gathered data, name each set according to the gap size tested and pressure used.
19. Adjust the brace to induce an 8 mm gap, as described in Step 8 of this procedure. Name each test data file according to the gap height and test iteration.

Chapter 4: Results

4.1 ANSYS Analysis

4.1.1 Cylinder Model

The cylinder model was analyzed in ANSYS to provide a simplified model to understand the stresses and strains experienced with a load. The results for total deformation, normal stress, and normal elastic strain were presented for an unbroken model and a fracture model with a callus to understand how the results changed. Additionally, the cylinder model's simple geometry allowed the ANSYS results to be validated through manual calculations.

Unbroken Model

The unbroken cylinder was created with a mesh containing 21,654 nodes and 4,836 elements in ANSYS. It was analyzed based on the three different simplified isotropic Young's modulus values. The experimental ANSYS results for total deformation, normal stress, and normal strain are presented in Table 7. Additionally, the calculated results for each are provided in Table 7 for comparison. These were calculated using the following equations:

$$\text{Total Deformation: } \delta = \frac{FL}{EA}$$

$$\text{Normal Stress: } \sigma = \frac{F}{A}$$

$$\text{Strain: } \varepsilon = \frac{\delta}{l_o}$$

Table 7: Theoretical ANSYS and calculation results for 400N compressive force applied on cylinder model

	Real Bone		**SawBone**		**Polyurethane Bone**	
	Experimental	Calculations	Experimental	Calculations	Experimental	Calculations
Young's Modulus (GPa)	10		1.5		0.4	
Total Deformation (mm)	0.0354	0.0355	0.236	0.237	0.885	0.887
Normal Stress (MPa)	-0.93	-0.93	-0.93	-0.93	-0.93	-0.93
Strain (mm/mm)	$-9.3*10^{-5}$	$-9.3*10^{-4}$	$-6.23*10^{-4}$	$-6.23*10^{-4}$	$-2.33*10^{-3}$	$-2.33*10^{-3}$

A trend identified in the data was that as the model became weaker with a lower Young's modulus, the total deformation and strain increased. Weaker bones, such as the polyurethane bone model at 0.4 GPa, were more susceptible to deformation and the resulting strain increased. Another trend was that the normal stress did not change across the three data sets because it was dependent on the model's area not mechanical properties.

As an example, the ANSYS result and validation for normal elastic strain for the SawBone at 1.5 GPa are provided below.

$$\varepsilon = \frac{\delta}{l_o}$$

$$\varepsilon = \frac{-0.237\ \text{mm}}{380\ \text{mm}} = -0.000623$$

$$\mu\,\text{strain} = \frac{-0.000623}{10^{-6}} = 623$$

In Figure 47, the probe tool was used to identify -0.000623 as the strain value for the majority of the cylinder model. This value was validated by the calculations above for strain that resulted in -0.000623 strain or 623 microstrain.

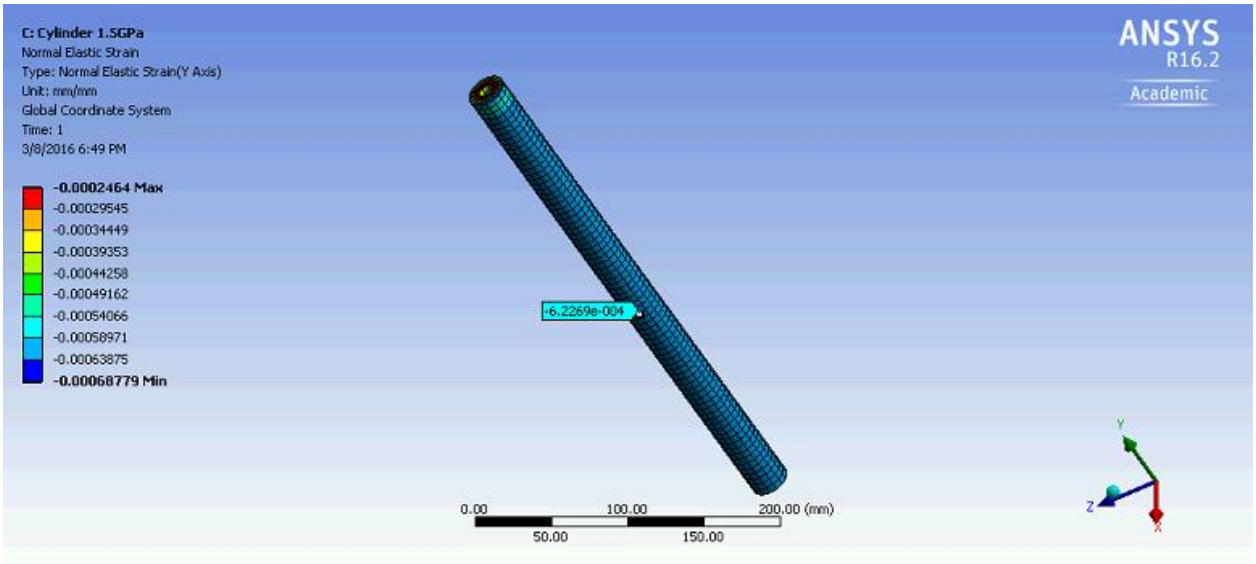

Figure 47 Strain for unbroken cylinder model at 1.5 GPa

Appendix C contains the total deformation and normal stress ANSYS results and validations for the SawBone model. In addition, the ANSYS results for a nodal force on half of the bottom cylinder face are provided.

Fracture Model

The cylinder was then modeled with a fracture to understand how the total deformation, normal stress, and strain results in Table 7 changed with the introduction of a break. A callus was added to the middle of the cylinder and used to simulate responses of broken bones of different strengths. Along with the unbroken cylinder model, these tests were used to obtain a general understanding of the different stresses and strains on a bone material under the loading conditions. These tests further validated the bone properties created in ANSYS for the cortical bone, SawBone, polyurethane bone, and callus material. The mesh for this model contained more

nodes and elements (59,007 nodes and 12,836 elements) to better represent how the model responds to the forces. The 1 mm thick callus had a Young's modulus of 1 GPa for the cortical bone model, which had a modulus of 10 GPa. Since the SawBone and polyurethane bone had Young's moduli an order of magnitude less than the cortical bone, the strength of the callus was adjusted to 0.1 GPa. The cylinder was first tested under conditions of a 400 N compressive load evenly applied to the bottom of the cylinder, with the top of the cylinder fixed. The resulting deformation, normal stress, and strain for each type of bone material, can be seen in Table 8.

Table 8: ANSYS results in the callus for 400N compressive force applied to entire bottom of cylinder

	Cortical Bone	**SawBone**	**Polyurethane Bone**
Deformation (mm)	0.0341	0.245	0.845
Normal Stress (MPa)	-0.977	-0.977	-0.977
Strain (mm/mm)	$-2.27*10^{-5}$	$-3.24*10^{-4}$	$-2.57*10^{-4}$

The deformation and strain increased as the materials became weaker, and the stress remained constant at -0.977 MPa because this parameter depends only on the force and cross sectional area. Compared to the unbroken cylinder model, the normal stress was slightly higher in the broken model. All of the strains were smaller in the broken model, and the deformations in the cortical bone and polyurethane broken cylinder models were also smaller compared to the unbroken cylinder. With the addition of the callus into the model, the maximum strain occurred in the callus and created a stress concentration (Figure 48). Within the models, the maximum strains were typically found in the callus of the model. The stresses and strains in the calluses can be seen in the Figure 48.

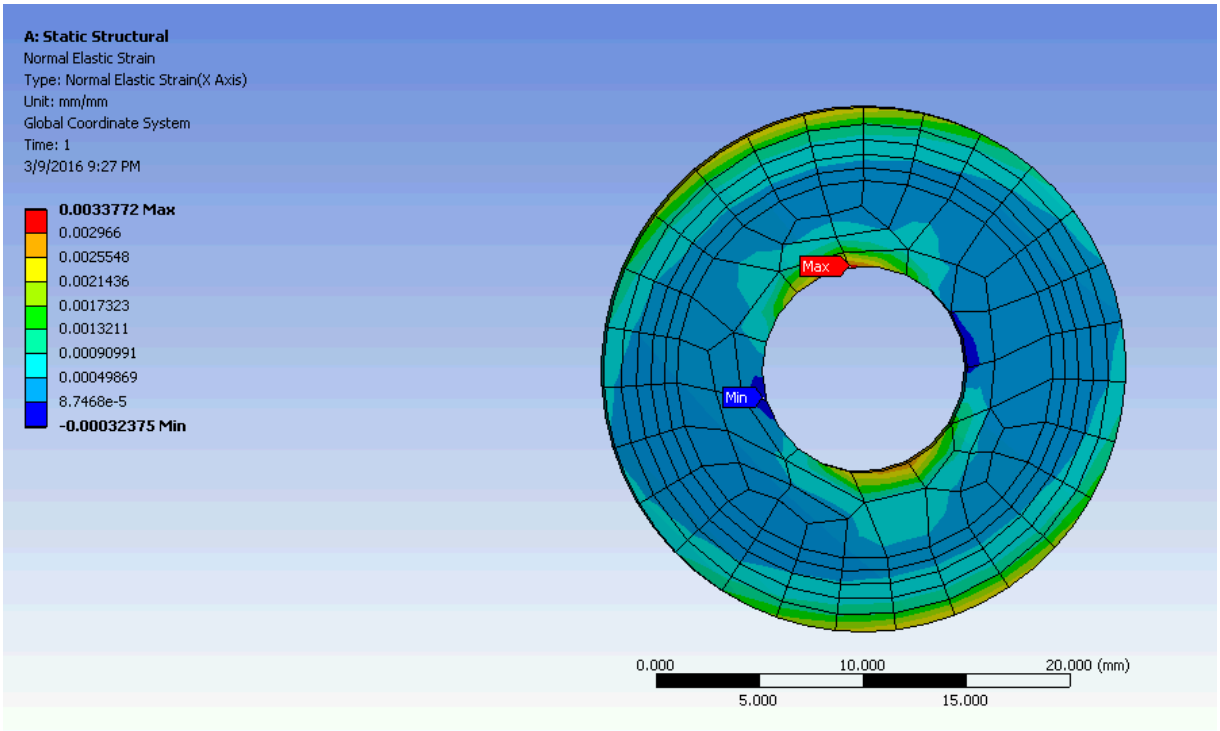

Figure 48 Strains in the callus for the broken cylinder model with the properties of a SawBone

Additional pictures of the stresses and strains in the broken cylinder models can be found in Appendix C. The same tests were run with the force applied through a nodal force to half of the bottom face of the broken cylinder model. The tests yielded similar results to those for the broken model and were also less compared to the nodal force on the unbroken model. The full results from the nodal force test can be found in Appendix C.

4.1.2 Tibia Model

After the calculations from the cylinder model were used to validate the analysis, a SOLIDWORKS tibia bone model was used to visualize the stresses and strains experienced on the actual tibia bone shape.

Unbroken Model

For the unbroken model, we determined the ANSYS results for the total deformation, normal stress, and normal elastic strain for a 400 N compressive force on the entire bottom face. The normal stress and strain were identified at the location of the expected fracture site using the probe tool (Table 9). Based on evaluation of the ANSYS model, these were not the maximum stresses and strain as those occurred either at the medullary cavity or the epiphysis sections of the model. The normal stress at the fracture site was represented by a range that correlated to the color across that portion of the model (seen in Appendix C). As validated in the cylinder model, the normal stress range was the same across all three different Young's moduli.

Table 9: ANSYS results for SawBone model at expected fracture site location for 400 N compressive force

	Cortical Bone	**SawBone**	**Polyurethane Bone**
Deformation (mm)	0.5	3.3	12.4
Normal Stress (MPa)	-0.911 to 0.137	-0.911 to 0.137	-0.911 to 0.137
Strain (mm/mm)	$-2.23*10^{-5}$	$-1.61*10^{-4}$	$-5.98*10^{-4}$

As seen in Figure 49, we were interested in the strain at the fracture site, which was for the SawBone -0.000161 mm/mm or 161 microstrain in the dark blue portion of the model. The larger strains were located at the end of the shafts in the green to red portions of the model.

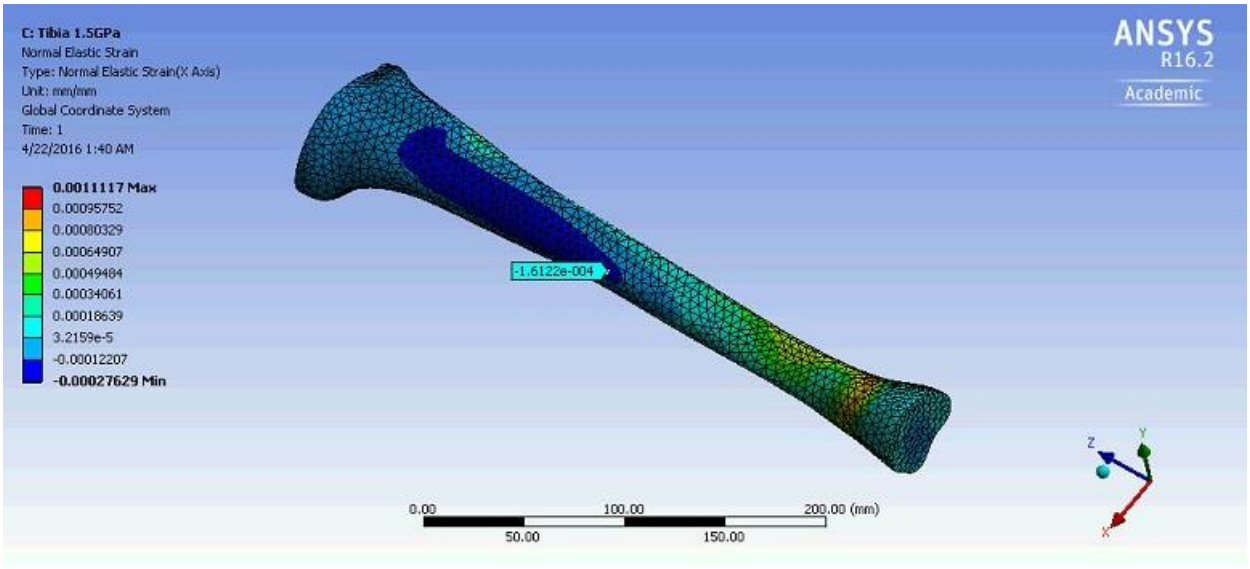

Figure 49 Strain for unbroken tibia model at 1.5 GPa

A nodal force, represented by the pink dots in Figure 50, was applied to half of the bottom face of the tibia model to simulate less than ideal conditions.

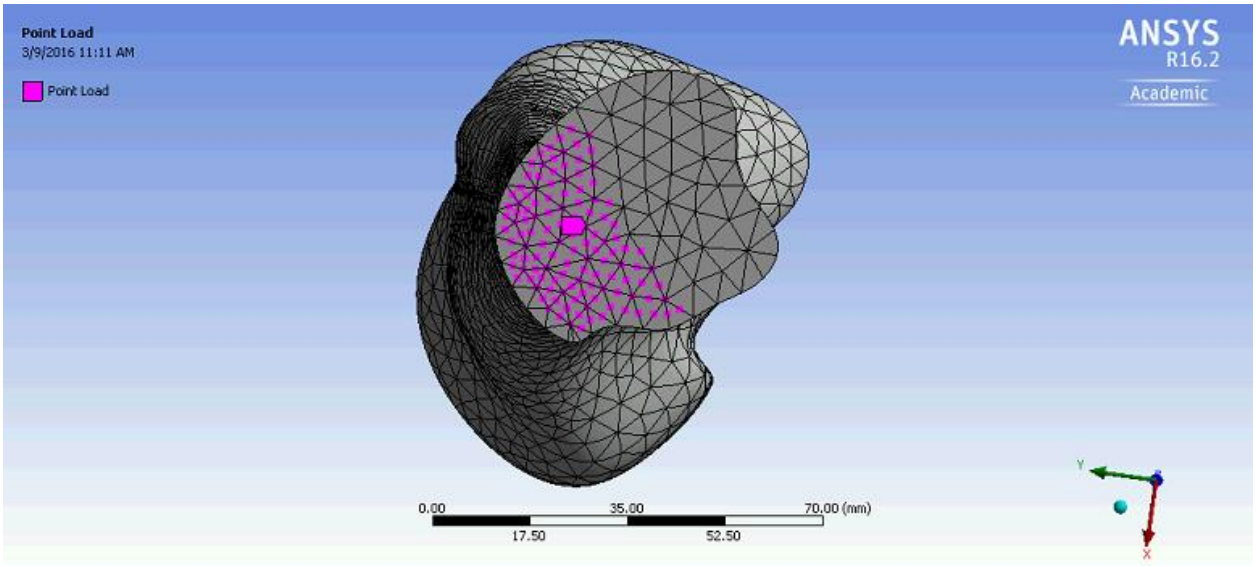

Figure 50 Nodal force on tibia

The ANSYS analysis was performed for the total deformation, normal stress, and strain (Table 10). In comparison to Table 7 results, the off center loading produced a 75% and 81% increase in strain for the SawBone and cortical bone models respectively. ANSYS experienced a solution magnitude error for the polyurethane bone with the nodal force.

Table 10: ANSYS results for SawBone model with 400 N compressive point load

	Cortical Bone	**SawBone**	**Polyurethane Bone**
Deformation (mm)	14.5	96.9	N/A
Normal Stress (MPa)	-1.28 to 2.33	-1.28 to 2.33	N/A
Strain (mm/mm)	-0.00184	-0.0123	N/A

Fracture Model

A 1 mm callus was added to the SOLIDWORKS tibia model to simulate how the broken bone would react to the theoretical 400 N compressive force. The force was first distributed evenly across the bottom face of the model. The deformation and strain increased as the material properties became weaker as seen in Table 11.

Table 11: ANSYS results for 400 N compressive force applied to entire bottom of tibia

	Cortical Bone	**SawBone**	**Polyurethane Bone**
Deformation (mm)	0.504	3.39	12.5
Normal Stress (MPa)	-1.31	-1.37	-1.07
Strain (mm/mm)	$-4.09*10^{-5}$	$-4.09*10^{-4}$	$-1.02*10^{-3}$

Comparatively, the strains in the SawBone broken bone model, -0.000409 mm/mm, were approximately 1.5 times higher than the unbroken bone model, -0.000276 mm/mm. For the unbroken model, the maximum strains occurred in the medullary cavity of the bone. In the broken bone model, the stress and strain concentrations appeared in the callus, which can be seen in Figures 51 and 52.

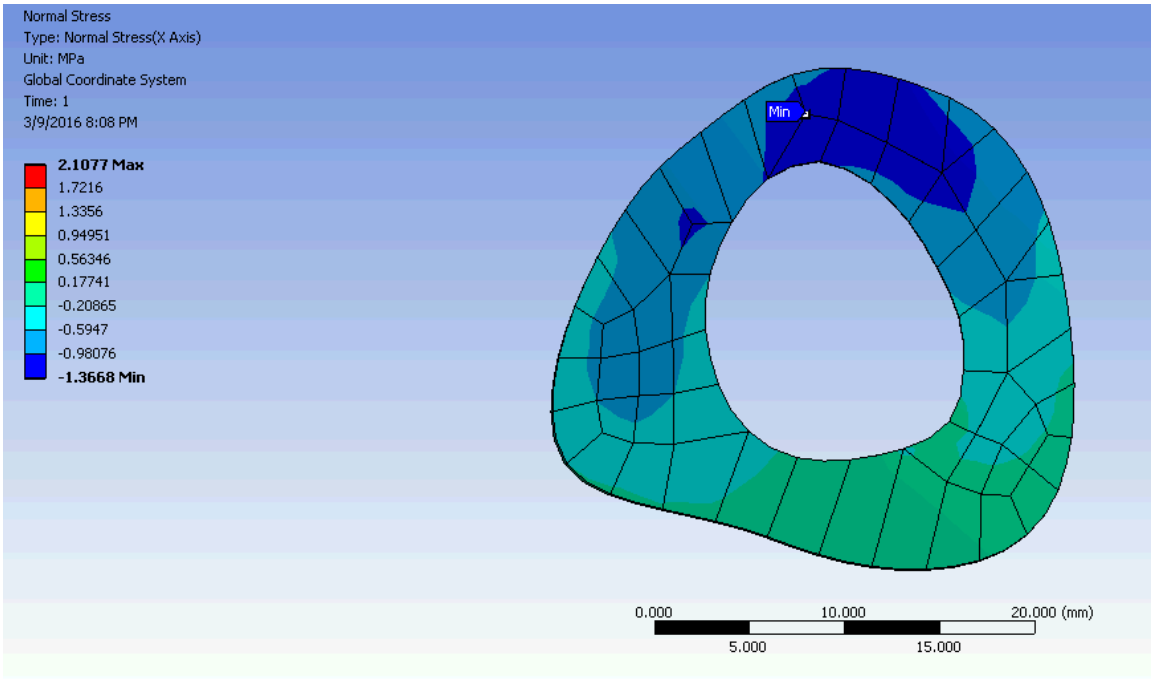

Figure 51 Normal stress in the callus on a 1.5 GPa SawBone model

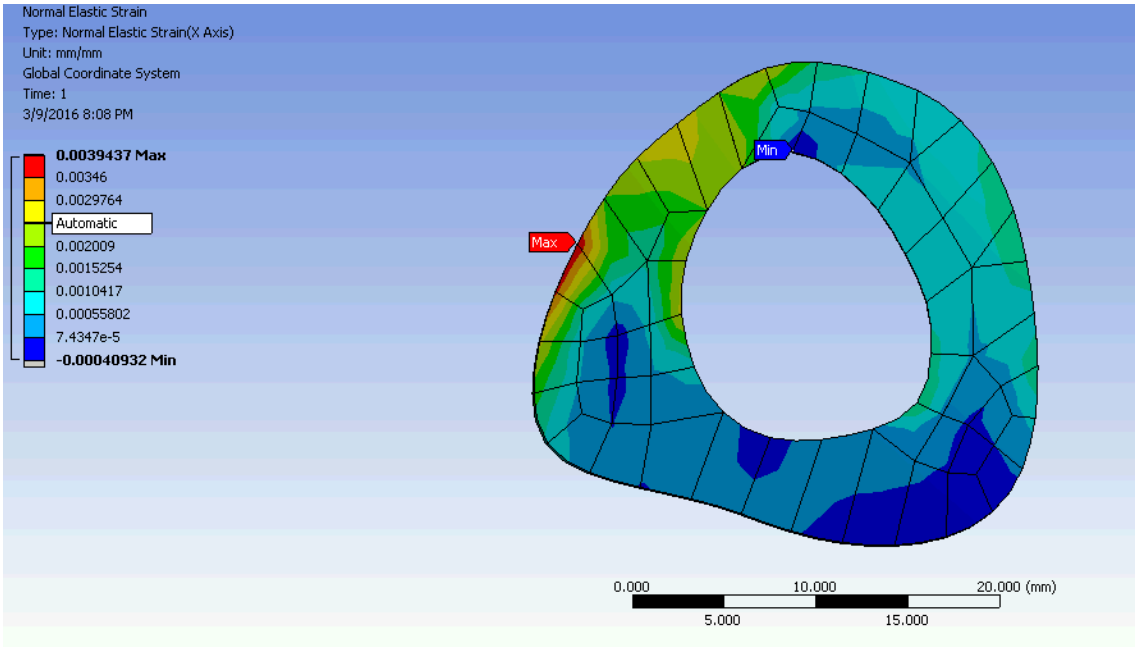

Figure 52 Strains in the callus on a 1.5 GPa SawBone model

The other stresses and strains in the callus for different material properties can be seen in Appendix C.

To simulate a less than ideal scenario, a 400 N compressive force was applied to half of the bottom face of the bone model as seen by the pink dots in Figure 53.

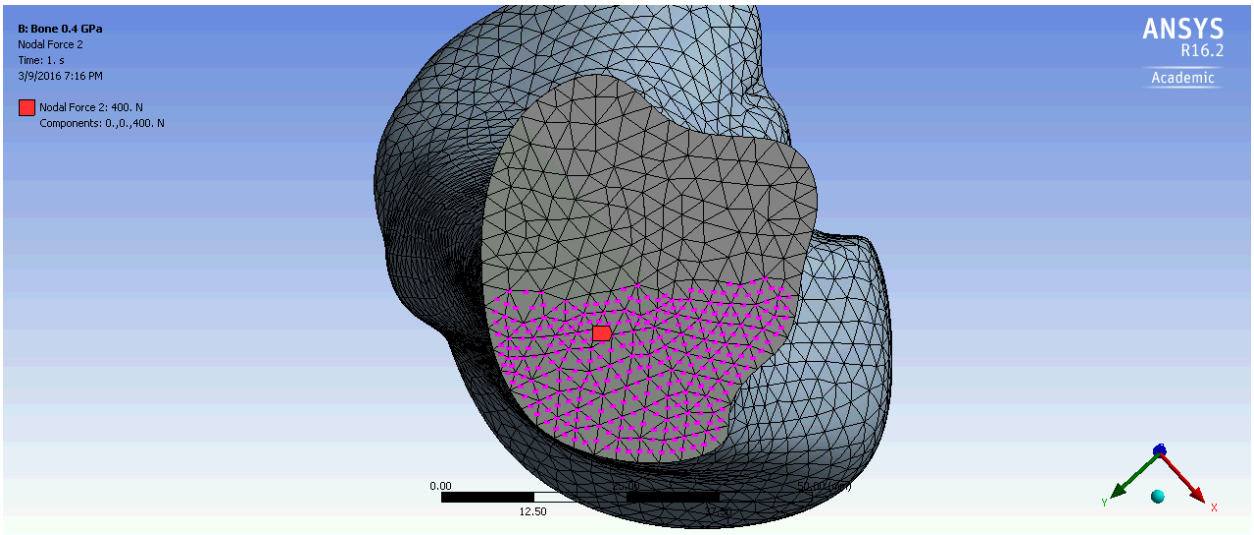

Figure 53 400 N compressive force applied to half the bottom of tibia model

Similar results were found from this scenario. The deformation, normal stress, and strain increased as the bone materials became weaker, as seen in Table 12.

Table 12: ANSYS results for 400 N compressive force applied to half of bottom tibia face

	Cortical Bone	**SawBone**	**Polyurethane Bone**
Deformation (mm)	10.6	3.18	11.9
Normal Stress (MPa)	-1.41	-1.78	-1.51
Strain (mm/mm)	-0.00389	-0.00114	-0.00413

Compared to the forces distributed across the entire bottom face, the strains are a magnitude higher in the cortical and SawBone models and is approximately four times higher for the polyurethane bone (Figure 54). The normal stresses were also about three times higher for this round of testing, -1.78 MPa for the SawBone compared to -0.54 MPa (Figure 55).

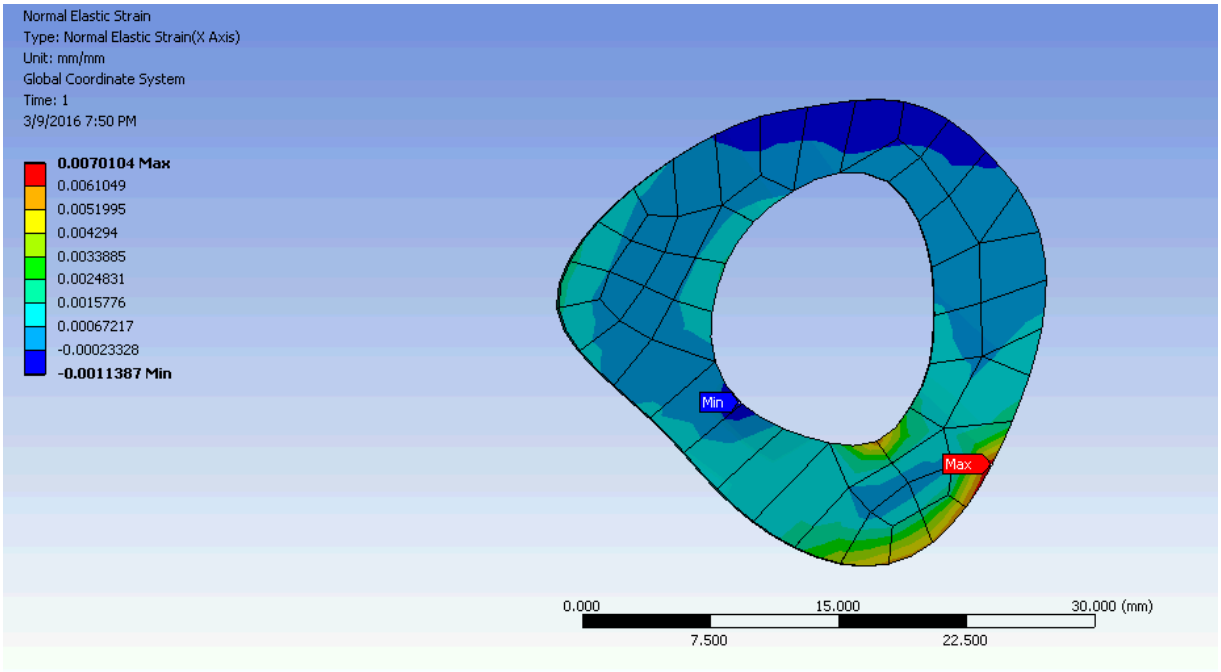

Figure 54 Strains on a SawBone model with a nodal 400 N force

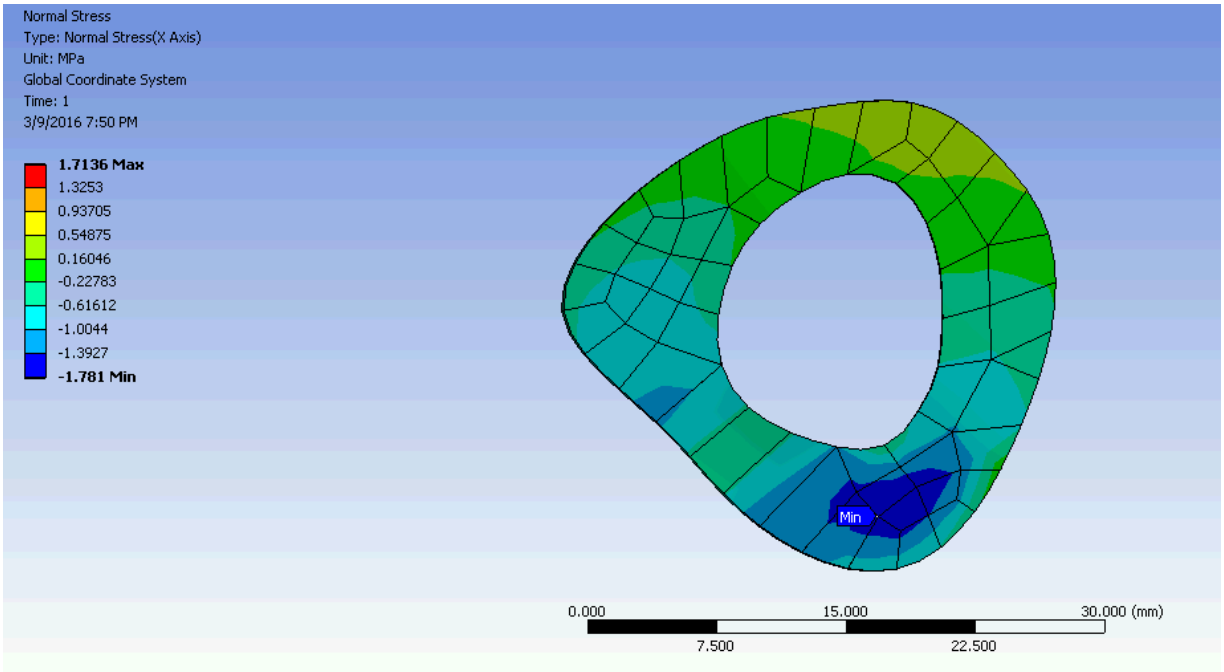

Figure 55 Stresses on a SawBone model with a nodal 400 N force

When the forces were concentrated on part of the bone, the increase in the stresses and strains in a broken bone model was significant. For the brace design, the data emphasized the importance of a stable landing to ensure that the appropriate strains were transmitted through the tibia. Further test results for the stresses and strains in different models can be seen in Appendix C.

4.2 Bone Analogue Mechanical Properties Results

4.2.1 Instron Testing

Eight bones underwent three-point bending tests on the Instron. Four of these bones were made from polyurethane, two of the bones were high-density polyurethane bones, and two bones were SawBones. The forces applied to the bones and the extensions of the bones were extracted from the Bluehill software. Table 13 displays the maximum extension of the bone before failure and the corresponding force applied.

Table 13: Three Point Bending Test Results

	Maximum Extension (mm)	**Load (N)**
Bone 1	8.34	275
Bone 2	2.92	386
Bone 3	15.3	164
Bone 4	12.1	188
High-Density Bone 1	6.04	170
High-Density Bone 2	10.5	280
SawBone 1	11.5	942
SawBone 2	12.5	1260

Using the three-point bending equation, Young's modulus was calculated from the maximum extension and force as seen in the example below for our first polyurethane bone. The

length of the bone was 38 cm, the radius was 1.7 cm, and I is the area moment of inertia for a cylinder.

$$E = \frac{FL^3}{48\delta_{max}I}$$

$$I = \frac{\pi r^4}{4}$$

$$I = \frac{\pi(0.017\ \text{m})^4}{4}$$

$$E = \frac{(275\ \text{N})(0.38\ \text{m})^3}{48(0.0083\ \text{m})\frac{\pi(0.017\text{m})^4}{4}}$$

$$E = 0.574\ \text{GPa}$$

The Young's moduli calculations for all of the bones tested can be seen in Table 14.

Table 14: Young's Moduli Calculations

Bone	Young's Modulus (GPa)
Bone 1	0.57
Bone 2	2.3
Bone 3	0.19
Bone 4	0.27
High Density Polyurethane 1	0.49
High Density Polyurethane 2	0.46
SawBone 1	1.44
SawBone 2	1.77

Four polyurethane bones were created using the method outlined in the methodology. Young's moduli of these bones had a wide range from 0.188 GPa to 2.30 GPa, which were not close to the goal of 10-15 GPa. The results of the three-point bending test confirmed the difficulty in making bones with the same mechanical properties as cortical bone as well as each

other. There were many parameters during the polyurethane bone making process that could not be controlled. In an attempt to control some of these parameters, high density polyurethane bones were experimented with. These types of bones were made by continuing to mix the polyurethane when it began to foam, and therefore preventing the foam from expanding as much as expected. Higher density polyurethane foam was created because less air entered the foam during expansion with the addition of stirring. Instead of pouring the foam into the mold, the group opened the mold and scooped the foam into the mold, making sure every spot was filled before putting the mold together. The higher density polyurethane bones were also tested through three-point bending and presented similar Young's moduli as the original polyurethane bones. Creating the bones was a difficult process to repeat, and the bones showed physical deformation after testing (Figures 56 and 57). These limiting factors led to the decision to no longer make high-density polyurethane bones.

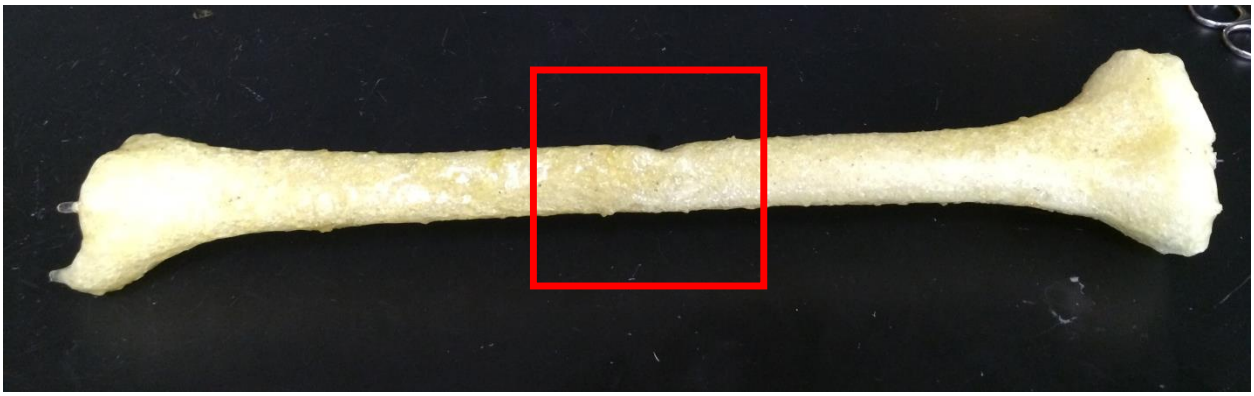

Figure 56 A high-density polyurethane bone after testing

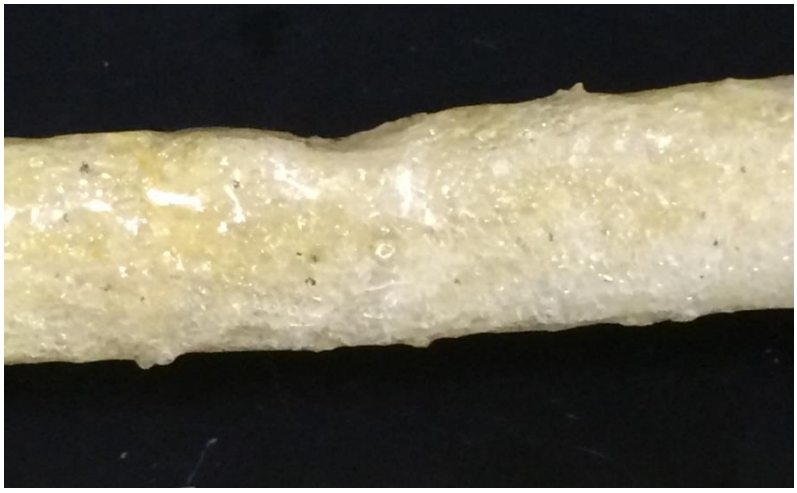

Figure 57 The deformation in the high-density polyurethane bone after testing

After having trouble producing repeatable bones and bones with proper mechanical properties, a two SawBones were tested on the Instron. The bones had Young's moduli of 1.44 GPa and 1.77 GPa, respectively. The SawBones had the best mechanical properties of all the bones tested. As a result, the SawBones were chosen to be tested in the cumulative test.

4.3 Axial Compressive Force Test Results

4.3.1 Polyurethane Bones

Four different polyurethane bones were tested: one unbroken bone and three broken bones (Bone 2, Bone 3, and Bone 4). Bone 1 was not tested due to a lack of structural stability at the distal end. Table 15 contains the microstrain for each analogue bone from 100 N to 400 N at 50 N intervals. The polyurethane bone results were inconsistent between each bone and can be attributed to the inability to create consistent analogues with the polyurethane. The main concern

with the polyurethane bones was that the Young's modulus values were below 1 GPa, not comparable to the callus at 1 GPa or cortical bone at 10 GPa or greater.

Table 15: microStrain results for testing on fake polyurethane and epoxy bones

		Unbroken Bone	Bone 2	Bone 3	Bone 4*
Force (N)	**Pressure (psi)**	**microStrain**	**microStrain**	**microStrain**	**microStrain**
100	**12.7**	407	191	149	244
150	**19.1**	690	357	356	1844
200	**25.4**	1240	409	778	8483
250	**31.8**	1775	352	1187	5879
300	**38.2**	1942	800	1813	72404
350	**44.5**	2338	525	2152	NO READING
400	**50.9**	2360	482	2319	NO READING

*Strain gauge on Bone 4 broke in half after 300 N force was applied.

The linear relationship between strain and force is illustrated in Figure 58. The unbroken bone and Bone 3 had r-squared values of 0.958 and 0.982 respectively. Bone 2 had an r-squared value of 0.7587, with the elimination of 300 N force outlier, indicating the test was limited at low strain values.

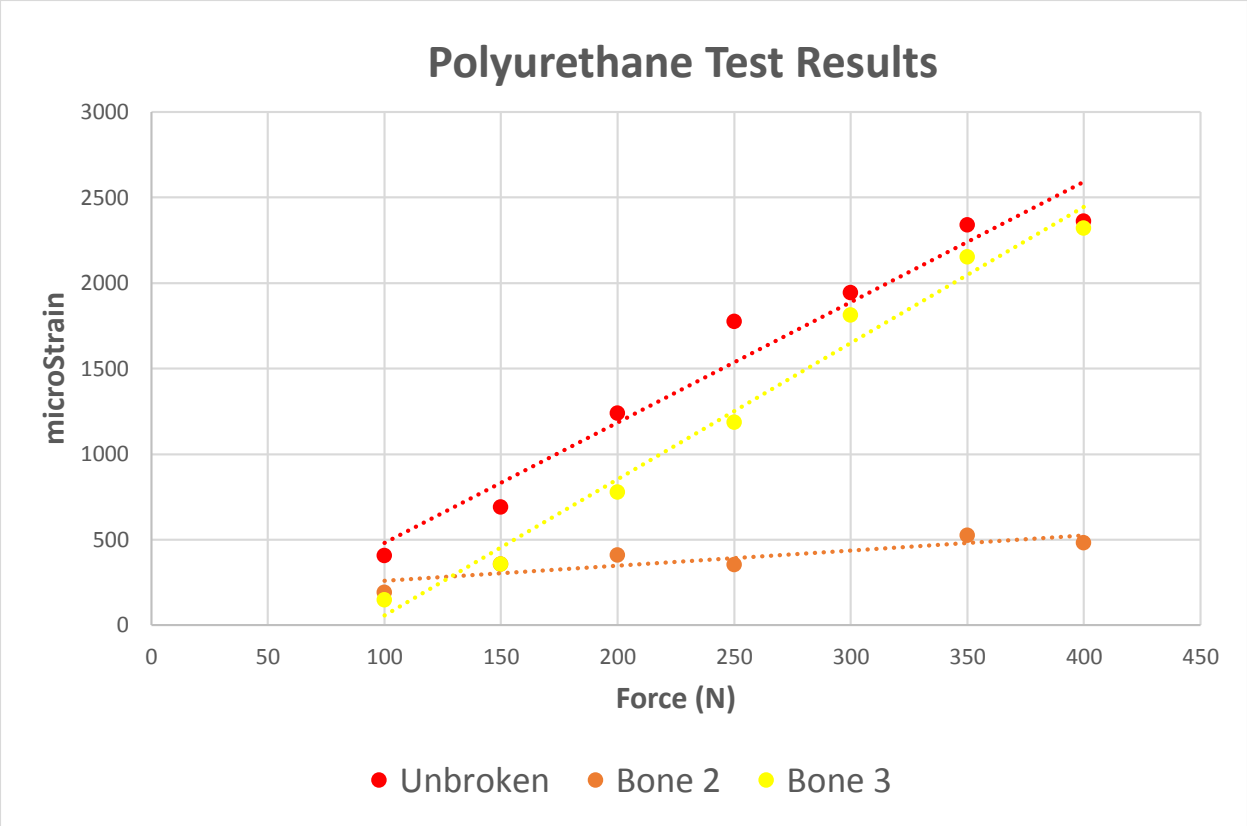

Figure 58 Strain versus force graphed results for polyurethane bones

The stress applied to the bones and the resulting strain readings were graphed to determine Young's modulus for the callus on the broken bones and the Young's modulus for the bone for the unbroken model (Figure 59). The unbroken bone had a Young's modulus of 0.4 GPa. Bones 2 and 3 had Young's moduli of 1 GPa and 0.4 GPa, respectively.

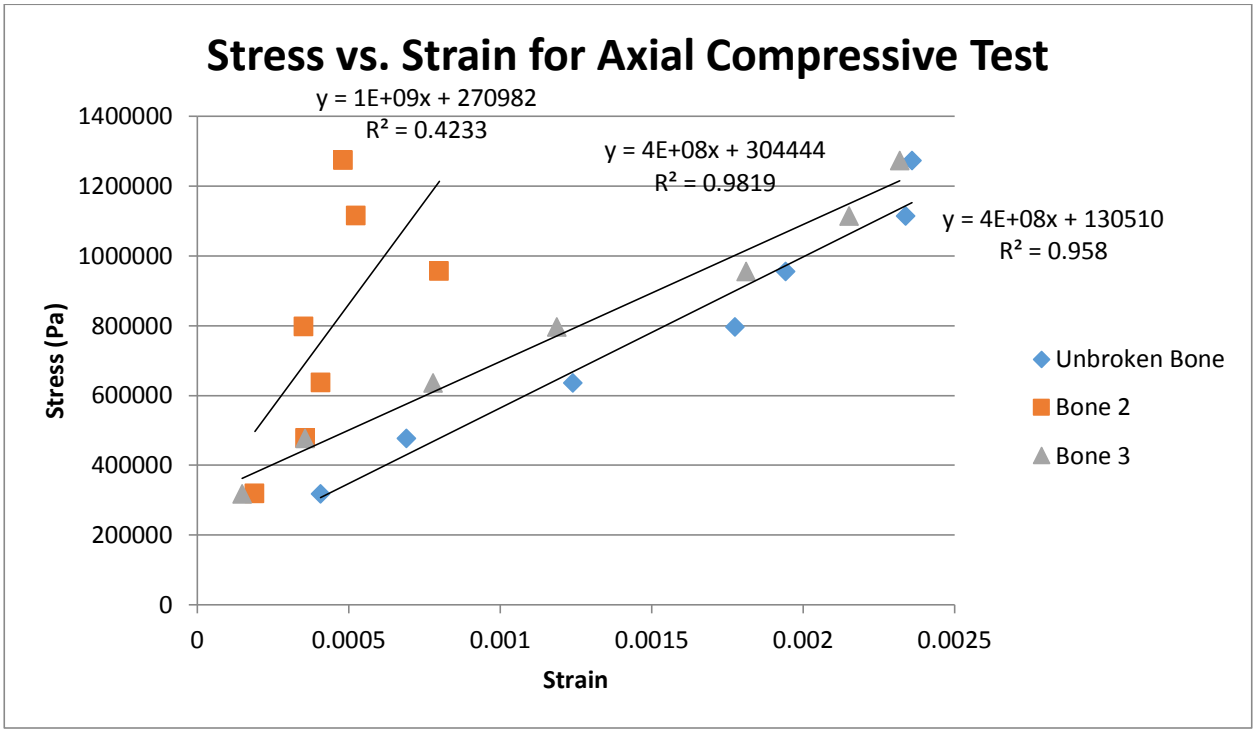

Figure 59 Stress vs. strain graphs for the bones tested

Under the same testing conditions, the polyurethane bones did not produce repeatable results as seen in Table 16. Two tests were run on the unbroken bone and a broken bone (Bone 2) to determine the repeatability of the strain on the polyurethane bones. The unbroken bone had a 47% decrease from test 1 to test 2, while the broken bone had a 13-82% decrease dependent upon the force.

Table 16: microStrain Results for Repeat Test on Unbroken Bone and Bone 2

		Unbroken Bone		Bone 2	
		Test 1	Test 2	Test 1	Test 2
Force (N)	Pressure (psi)	microStrain		microStrain	
100	12.7	777	407	222	191
200	25.4	2403	1240	767	409
300	38.2	3668	1942	1057	800
400	50.9	4433	2360	2724	482

The stresses and strain readings were compared (Figure 60). A linear trend line was fit to each set of data, and the slopes of each line, or Young's moduli, were compared. For the unbroken bone, the Young's moduli were 0.3 and 0.5 GPa for tests one and two. Bone 2 had Young's moduli of 0.4 and 0.1 GPa. The difference in the data sets showed the lack of repeatability of the polyurethane bone

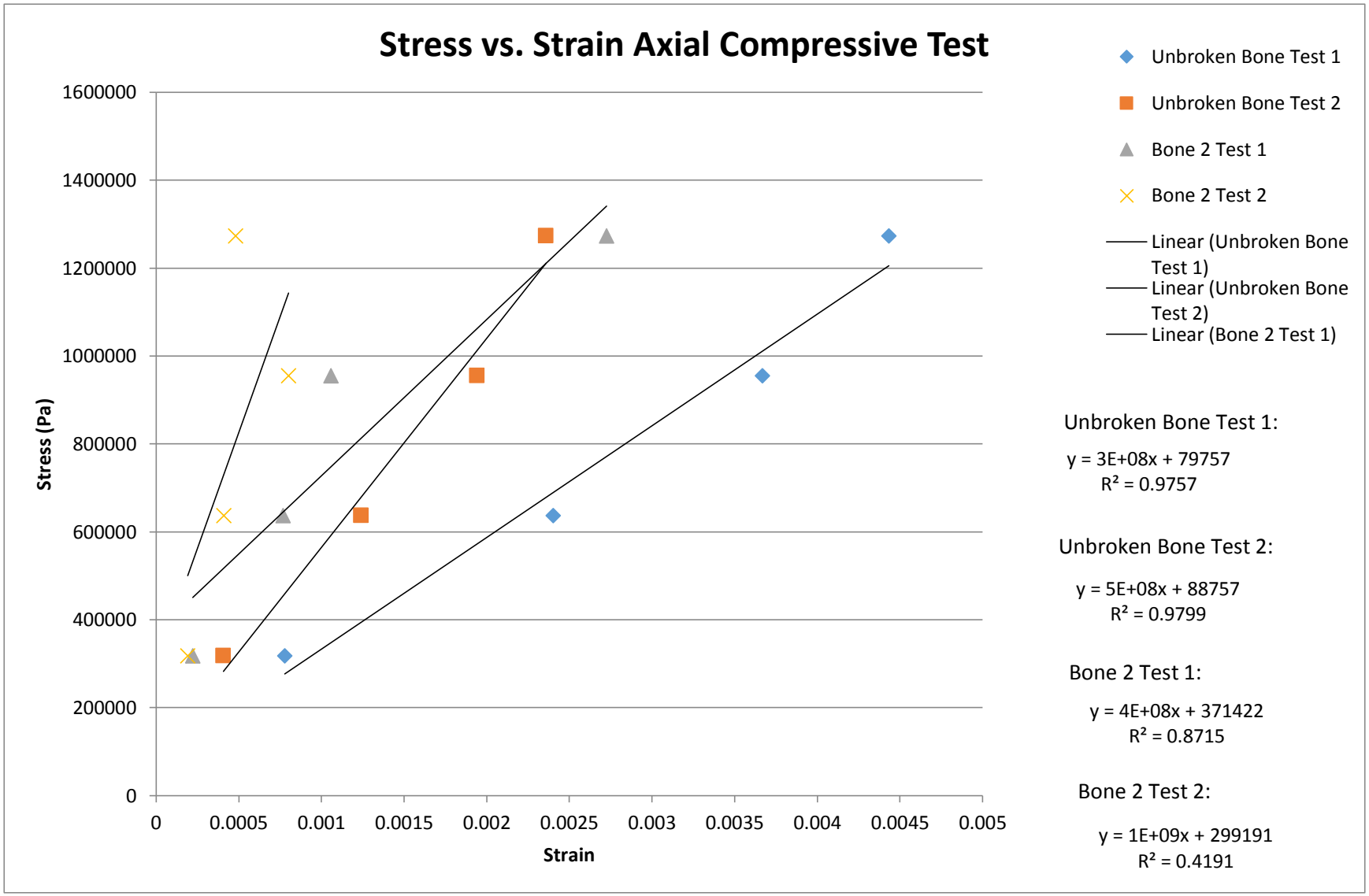

Figure 60 Stress vs. strain graph comparing the data sets for Unbroken Bone and Bone 2

We determined the polyurethane bones should not be used in the analogue leg for the cumulative test because it was not representative of real bone. The decision was based on the weak material properties and potential for a higher modulus in the SawBone. However, the process of testing the weak polyurethane bones helped us learn the importance of material properties in relation to strain measurements. As a result, we also refined our Instron and air cylinder testing procedures.

4.3.2 SawBone

Based on the test results for the polyurethane bones, we performed the testing on the SawBone analogue. The SawBone had a higher Young's modulus at 1.4 GPa from the Instron test. The test was performed three times on the SawBone with the strain and standard deviation at each force indicated in Table 17.

Table 17: microStrain results for multiple tests on SawBone

		Test 1	Test 2	Test 3	
Force (N)	**Pressure (psi)**	**microStrain**			**STD**
100	**12.7**	230	220	210	10
150	**19.1**	710	660	600	50
200	**25.4**	1200	1060	1130	55
250	**31.8**	1690	1640	1650	20
300	**38.2**	2650	2520	2830	120
350	**44.5**	4020	4420	3850	240
400	**50.9**	5420	5150	4790	260

Compared to the polyurethane bones test results, the SawBone's microstrain results were repeatable across multiple tests at each force. In Figure 61, the microstrain results for each test were graphed, and the r-squared values were 0.941 (Test 1), 0.933 (Test 2), and 0.967 (Test3). At

each applied force, the point for each separate test overlaps indicating the repeatability with their standard deviations in Table 17.

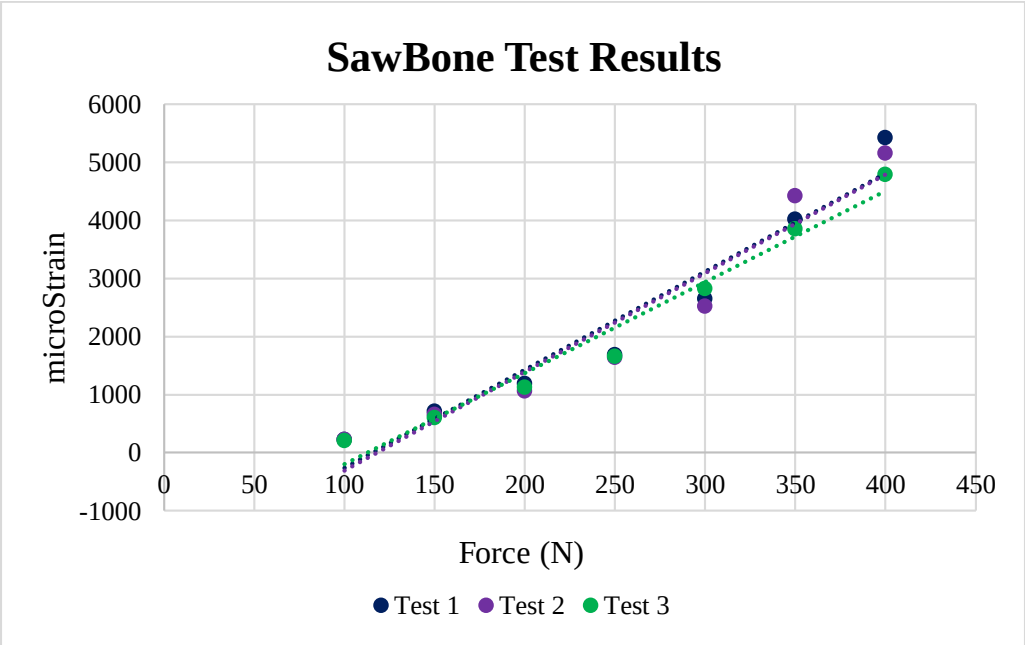

Figure 61 Strain versus force graphed results for SawBone microStrain measurements for multiple tests

The Young's modulus of the callus was determined from the stress versus strain for each test (Figure 62). For the majority of the tests, the Young's moduli across the strain gauge was calculated to be 0.2 GPa. The proximity in the Young's moduli values and stress versus strain curves show the repeatability of the SawBones.

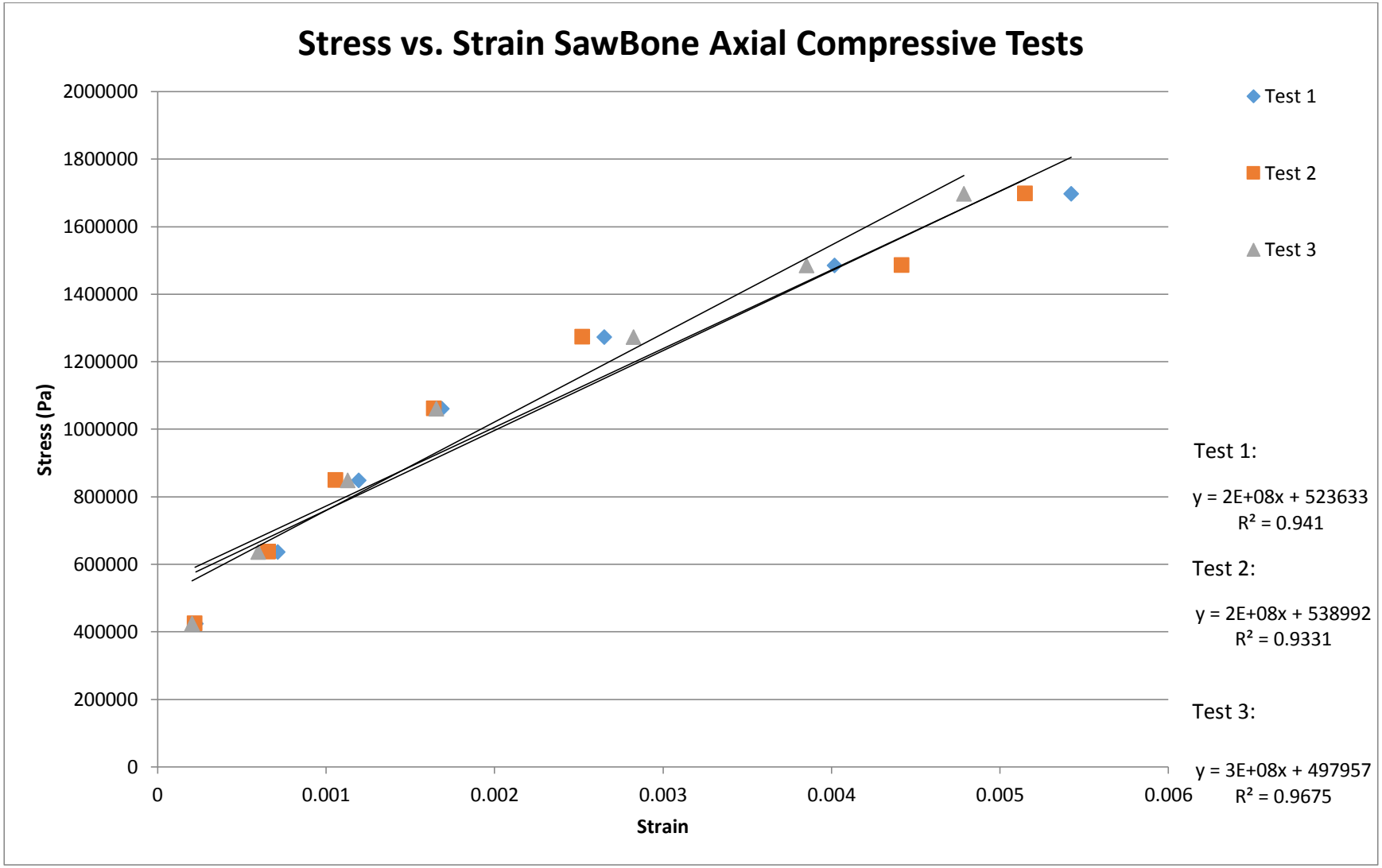

Figure 62 Stress vs. strain curves for three tests on the SawBone

As seen in Figure 63, the strain gauge was attached to both the SawBone and callus indicating that the 0.2 GPa Young's modulus was for the different materials in series.

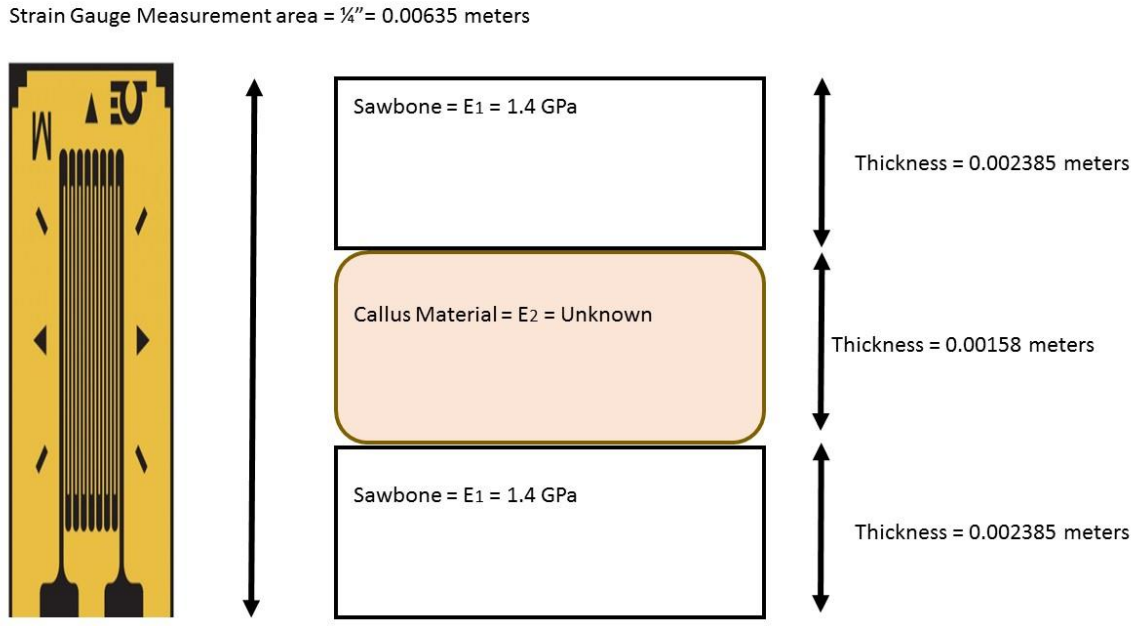

Figure 63 Strain gauge location on analogue bone with SawBone and Callus material

The Young's Modulus for the callus (E_2) was calculated as 0.056 GPa based on the following calculations:

$$E_{Total} = 0.2\ GPa$$

$$E_1 = 1.4\ GPa$$

$$E_2 = ?$$

$$\frac{1}{E_{Total}} = \frac{1}{E_1} + \frac{1}{E_2}$$

$$\frac{1}{0.2\ GPa}(0.00635\ m) = \frac{1}{1.4\ GPa}(0.00476\ m) + \frac{1}{E_2}(0.00158\ m)$$

$$E_2 = 0.056\ GPa$$

The SawBone did not produce the desired 1000 - 2000 microstrain range at the expected 400 N - 800 N applied force. Those values were based on cortical bone at a Young's modulus greater than 10 GPa and a callus at a Young's modulus of 1 GPa, not on the analogue bone material properties with a bone Young's modulus of 1.4 GPa and callus at 0.056 GPa. Based on the test results in Table 16, the actual applied force range for the desired 1000 - 2000 microstrain was 150 N - 300N.

4.4 Functional Walking Brace Force Sensor Results

4.4.1 Varying Gap Sizes

In order to find the optimal gap size, the group conducted force sensor walking tests with the subject barefoot, with the boot at no gap, and with 2 mm to 2 cm gap sizes at 2 mm intervals. This test was performed for design iteration 1 and design iteration 2 with sensors on the ball, heel, and outside of the foot. An additional test was performed with a force sensor located on the arch of the foot to determine if any substantial forces form walking came from this area; the arch proved to contribute minimal forces. We identified the peak forces experienced by the force sensors at each gap size.

Figure 64 illustrates the results at each sensor from the controls to a 3 cm gap size. From this test, we determined that it was unrealistic to use a gap size larger than 12 mm even though it showed a larger force reduction with the increasing gap. The subject's foot was no longer secured with the foot plate; this resulted in discomfort between the ankle and device, and was not stable for walking.

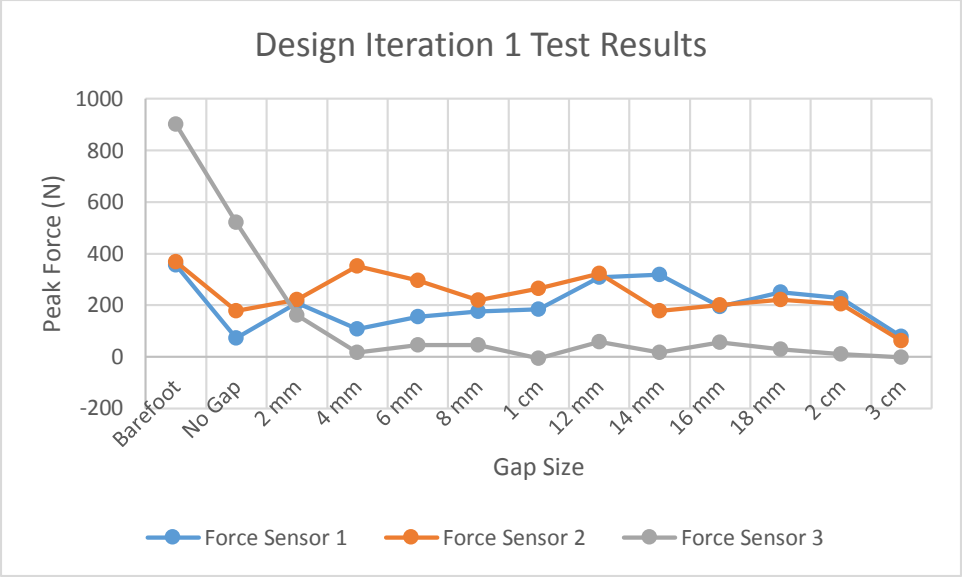

Figure 64 Design iteration 1 force sensor varying gap size results

Based on feedback from the design iteration 1 test, the device was modified as explained in Section 3.1.4.2 to fixate the knee joint. The same test was performed at the narrowed range of 2 mm to 12 mm as seen in Figure 65. The 8 mm gap produced minimal force at the heel and the most consistent force reduction for the sensors at the ball and outside of the foot compared to the other gap sizes.

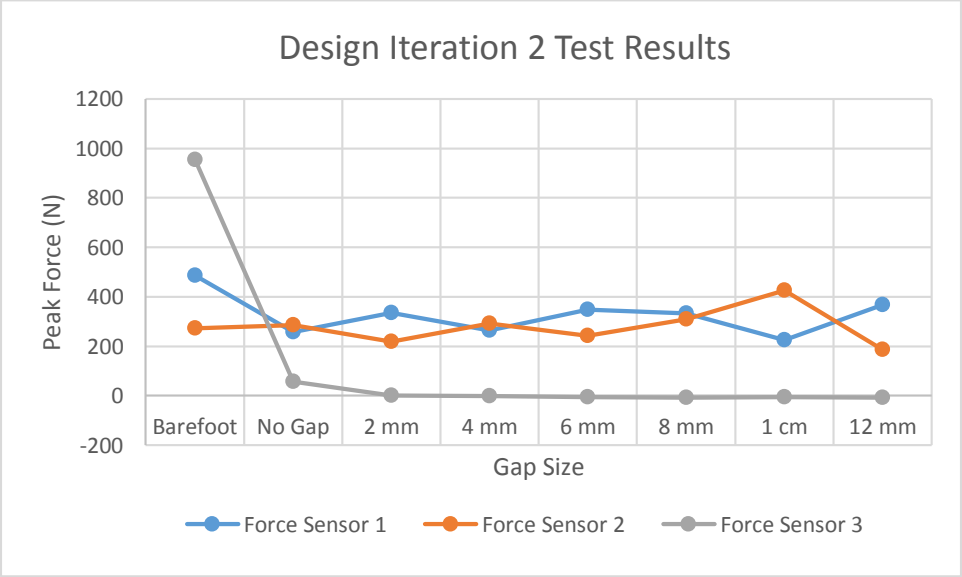

Figure 65 Design iteration 2 force sensor varying gap size results

4.4.2 Optimal Gap Size (8 mm)

Based on the measured force reduction and user feedback, the 8 mm gap size was determined to be the optimal gap beneath the heel. A gap greater than 1 cm below the heel created discomfort for the user characterized by hardware on the brace contacting the ankle and inability to insert the foot plate due to the increase in gap size. In Section 4.4.1 results, 8 mm had consistent force reduction for the force sensors on the ball and outside of the foot.

Additional testing was conducted at the 8 mm gap to determine the force measurements during different scenarios. Table 18 includes the peak force results for six different everyday activities: two normal steps, two slow steps, walking in place, impact step, step down, and four normal steps. As explained in Section 3.4.3, the tests were performed without the foam insert. The gap underneath the heel was periodically assessed to make sure the leg did not slip down in the boot. However, the 8 mm gap remained the most consistent and did not require adjustment throughout the various movements.

Table 18: Everyday Activities Force Sensor Results at 8 mm Gap

Everyday Activities Repetitive Testing			
	Sensor 1 (Ball)	**Sensor 2 (Outside)**	**Sensor 3 (Heel)**
Gap Size = 8 mm	**Peak Force (N)**		
2 Normal Steps			
Test 1	449	212	-7.2
Test 2*	121	85	-7.2
Test 3	228	262	-7.2
2 Slower Steps			
Test 4	396	268	-5.5
Test 5	452	364	-7.1
Test 6	340	208	-2.3
Walking in Place			

Test 7	163	208	-0.7
Test 8	175	221	1.3
Test 9	171	182	4.0
Impact Step			
Test 10	275	181	-7.8
Test 11	97	271	-5.7
Test 12	204	194	-3.0
Step Down			
Test 13	200	238	-9.7
Test 14	178	245	-7.6
Test 15	345	168	-9.6
4 Normal Steps			
Test 16	230	211	2.0
Test 17	407	294	2.2
Test 18	389	213	7.2

*Abnormal results for Test 2 (2 Steps) that could have been caused by a manual error in recording the data

The force versus time graphs for each scenario were analyzed to determine the peak force range based on motion. When necessary, outlier peak forces in the data were eliminated based on a visual inspection of the graphs. Figure 66 illustrates the force results for a standard test, two normal steps. As discussed above, the first peak generated the force from the unloading on the braced leg at the start of walking while subsequent peaks were experienced during walking on the brace for the two steps. The force sensor on the ball of the foot (Force Sensor 1) had a peak force of 228 N during unloading while the sensor located on the outside of the foot (Force Sensor 2) had a peak force of 261.6 during the last step. Overall, the graph shows that the force on the heel (Force Sensor 3) was a constant negative value correlating to a 0 N force on the foot.

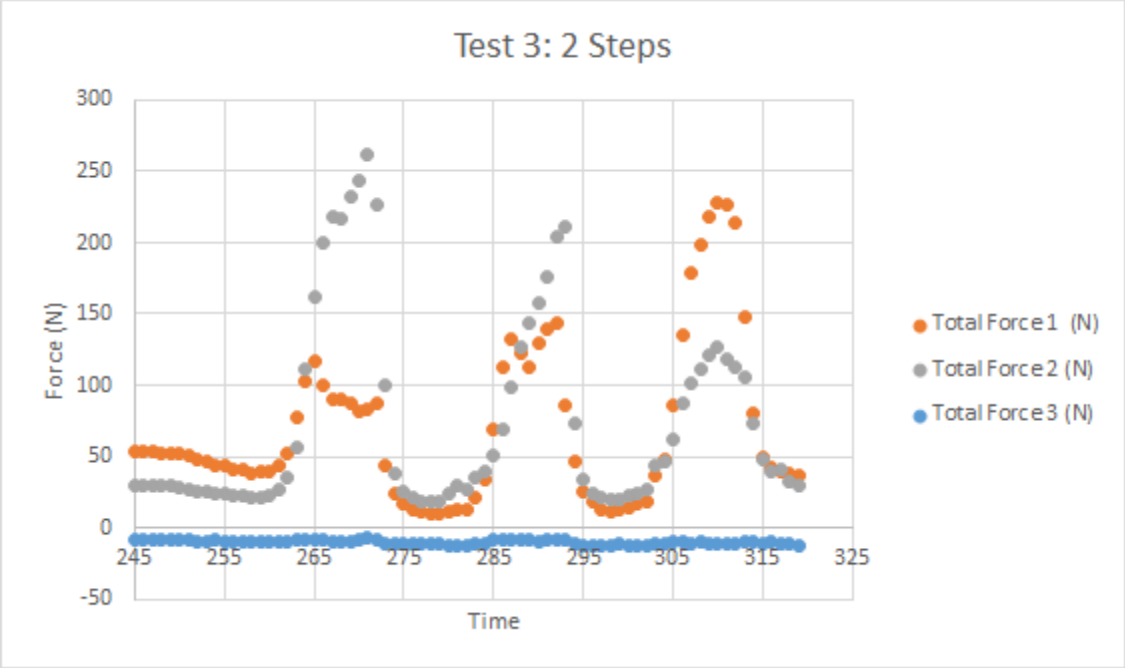

Figure 66 Test results for two normal steps at optimal gap size

In comparison, the results for a step down from a block onto the braced foot produced a different graph (Figure 67). Force Sensor 1 and Force Sensor 2 generated an initial spike when the unbraced leg stepped down. Then, the force decreased when the boot was not in contact with the block or ground. The peak forces occurred at the braced leg's contact with the ground reaching a 177.1 N force at the ball and 245.1 N on the outside of the foot. The force at the heel was consistently negative with a peak of only -7.61 N, which we assumed to correlate to zero force through the heel. This assumption was based on the inability for there to be a negative force from walking, indicating a voltage drift equal to approximately -7 N during testing.

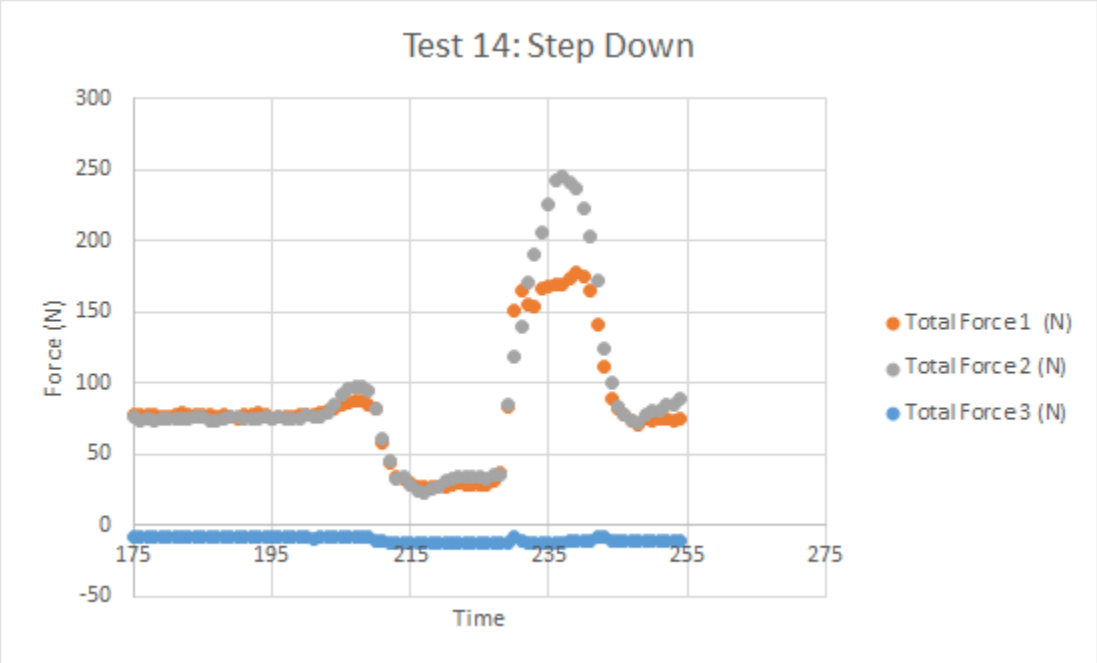

Figure 67 Test results from step down at optimal gap size

These everyday activities for someone restrained by the boot were tested to determine to what extent the device would be able to dampen forces. The highest force experienced, across all three sensor locations, was on the ball of the foot during normal walking at 452 N. Each force sensor experienced a consistent range of forces below the upper limit of 452 N for all different activities recorded in Table 18. The ball of the foot experienced a range of 120 – 452 N. The outside of the foot experienced an outlying maximum force of 369 N during slow walking, but typically the loads were 181 – 294 N range. The force sensor at the heel experienced a maximum force of 7.2 N during the four normal steps scenario.

For all the scenarios, the heel force was dampened when compared to the control test results. The control tests of no walking boot and walking boot with no gap had forces from 723 – 945 N and 57.4 – 522 N respectively. Each scenario experienced peak forces within the ranges indicated and had consistent force dampening at the heel location. The dampened forces created by the 8 mm gap size were then used to determine the strain experienced at the fracture site.

4.4.3 Verifying Calculations

Using free body diagrams and the peak forces from the force sensor readings, the forces and moment at the knee as well as the strain at the callus were calculated. The force sensor readings were taken from the ideal boot setting, an 8 mm gap. The free body diagram and equations can be seen below (Figure 68). We assumed the forces taken up by the calf muscles and bending moment created by the boot could be neglected based on inability to measure and calculate.

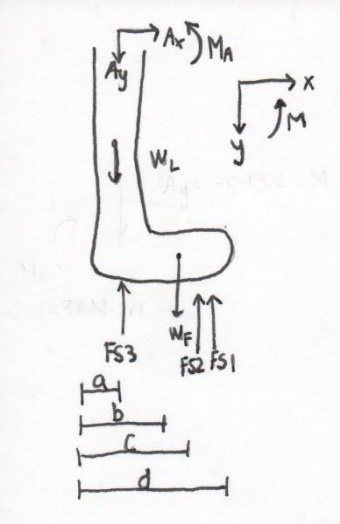

Figure 68 FBD for force sensor results at 8 mm gap

The assumptions about the mass and the variables seen in the free body diagram are listed below (De Leva, 1996):

$$\text{Mass: } 58.5 \text{ kg}$$

$$\text{Body weight: } 577.22 \text{ N}$$

$$\text{Weight of foot: } (0.0145)(577.22 \text{ N}) = 8.369 \text{ N}$$

$$\text{Weight of leg: } (0.0465)(577.22 \text{ N}) = 26.84 \text{ N}$$

$$a = 3.175 \text{ cm}$$

$$b = 12.065 \text{ cm}$$

$$c = 14.065 \text{ cm}$$

$$d = 16.51 \text{ cm}$$

$$FS1 = 445.5 \text{ N}$$

$$FS2 = 106.1 \text{ N}$$

$$FS3 = -8.69 \text{ N}$$

$$\text{Acceleration: } 0.5 \frac{m}{s^2}$$

The forces in the X and Y direction at the knee were 29.5 and 516 N respectively. The resulting moment at the knee was -70.8 N·m. The calculations for these forces and moment can be seen below (González-Torres et al., 2010):

$$\sum F_x = A_x = ma$$

$$A_x = (58.9 \text{ kg})(0.5 \frac{m}{s^2})$$

$$A_x = 29.5 \text{ N}$$

$$\sum F_y = A_y + W_L + W_F - FS1 - FS2 - FS3 = ma$$

$$A_y + (26.8 \text{ N}) + (8.37 \text{ N}) - (446.0 \text{ N}) - (106 \text{ N}) - (0 \text{ N}) = (58.9 \text{ kg}) \left(0.5 \frac{m}{s^2}\right)$$

$$A_y = 546 \text{ N}$$

$$\sum M = -(8.37 \text{ N})(0.0889 \text{ m}) + (106 \text{ N})(0.114 \text{ m}) + (446 \text{ N})(0.133 \text{ m}) + M_A = 0$$

$$M_A = -70.8 \text{ N} \cdot \text{m}$$

$$\sigma = \frac{F_y}{A}$$

$$\sigma = \frac{546\ \text{N}}{\pi((0.01\text{m})^2 - (0.005\ \text{m})^2)}$$

$$\sigma = 0.00232\ \text{GPa}$$

$$\varepsilon = \frac{\sigma}{E}$$

$$\varepsilon_{Bone} = \frac{0.00232\ \text{GPa}}{10\ \text{GPa}}$$

$$\varepsilon_{Bone} = 232\mu\text{strain}$$

$$\varepsilon_{Callus} = \frac{0.00232\ \text{GPa}}{1\ \text{GPa}}$$

$$\varepsilon_{Callus} = 2320\ \mu\text{strain}$$ E from lit?

To determine how much the forces and strains were reduced, a control test of barefoot walking was performed. The variables and assumptions from the previous example were the same, except the force sensor readings were 487, 273, and 954 N for sensors one, two, and three. The barefoot walking produced a stress of 0.00725 GPa and a strain of 7250 microstrain at the callus. The calculations can be seen below:

$$\sum F_x = A_x = ma$$

$$A_x = (58.9\ \text{kg})(0.5\frac{\text{m}}{\text{s}})$$

$$A_x = 29.5\ \text{N}$$

$$\sum F_y = A_y + W_L + W_F - FS1 - FS2 - FS3 = ma$$

$$A_y + (26.8\ \text{N}) + (8.37\ \text{N}) - (487\ \text{N}) - (273\ \text{N}) - (954\ \text{N}) = (58.9\ \text{kg})\left(0.5\frac{\text{m}}{\text{s}}\right)$$

$$A_y = 1708\ \text{N}$$

$$\sum M = -(8.37\ \text{N})(0.0889\ \text{m}) + (273\ \text{N})(0.114\ \text{m}) + (487\ \text{N})(0.133\ \text{m}) + M_A = 0$$

$$M_A = -95.1\ \text{N} \cdot \text{m}$$

$$\sigma = \frac{F_y}{A}$$

$$\sigma = \frac{1708\ \text{N}}{\pi((0.01\ \text{m})^2 - (0.005\ \text{m})^2)}$$

$$\sigma = 0.00725\ \text{GPa}$$

$$\varepsilon = \frac{E}{\sigma}$$

$$\varepsilon_{Bone} = \frac{0.0072\ \text{GPa}}{10\ \text{GPa}}$$

$$\varepsilon_{Bone} = 725\ \mu\text{strain}$$

$$\varepsilon_{Callus} = \frac{0.00725\ \text{GPa}}{1\ \text{GPa}}$$

$$\varepsilon_{Callus} = 7250\ \mu\text{strain}$$

For the 8 mm gap, the bending stress was found to be in tension at 0.038 GPa and calculated using the equation below. The area moment of inertia (I) of the tibia was found in previous literature as 18,470 mm^4 (Milgrom, Gildaia, Simkin, Rand, Kedem, Kashtan, Stein, & Gomori, 1989):

$$\sigma = \frac{Mc}{I}$$

$$\sigma = \frac{(-70.8\ \mathrm{N \cdot m})(0.01\ \mathrm{m})}{1.87 * 10^{-8}\ \mathrm{m}^4}$$

$$\sigma = -0.038\ \mathrm{GPa}$$

Based on the principle of superposition, we determined the combined loading for the compressive normal stress (σ_N) and in tension bending stress (σ_B).

$$\sigma_{\text{combined loading}} = \sigma_B - \sigma_N$$

$$\sigma_{\text{combined loading}} = 0.0383\ \mathrm{GPa} - 0.00232\ \mathrm{GPa}$$

$$\sigma_{\text{combined loading}} = 0.015\mathrm{GPa}$$

$$\varepsilon_{\text{Bone}} = \frac{0.015\ \mathrm{GPa}}{10\ \mathrm{GPa}}$$

$$\varepsilon_{\text{Bone}} = 1503\ \mu\text{strain}$$

$$\varepsilon_{\text{Callus}} = \frac{0.015\ \mathrm{GPa}}{1\ \mathrm{GPa}}$$

$$\varepsilon_{\text{Callus}} = 15032\ \mu\text{strain}$$

Compared to our normal strain of 2320 GPA, the combined loading's strain was a magnitude larger. This can be attributed to our simplified free body diagram that did not include a presumed bending moment applied by the device on the leg. The device's bending moment would be reasonable equal and opposite to the moment applied on the leg (M_A). We were unable to calculate or measure the forces and moment from the brace on the leg. Therefore, the strain from the combined loading would be the maximum strain without considering the counteracting moment of the device or calf muscle.

4.5 Cumulative Device Validation Results

The cumulative test aimed to provide supporting data that the device would dampen the force and strain for a fractured tibia. However, the group was limited by the leg analogue's fragility and lack of structural stability. The gelatin leg physically deformed and deteriorated as testing progressed. We were able to perform two tests to record the force and strain, a control at no gap and the optimal gap at 8 mm, with a 60 psi air cylinder pressure. The 60 psi pressure corresponded to a 472 N force. Table 19 indicates that the three force sensors placed on the leg analogue did not record actual data with the same peak forces at both gap sizes.

Table 19: Force sensor results at 472 N force for no gap and optimal gap

	Sensor 1	**Sensor 2**	**Sensor 3**
Gap Size (mm)	**Peak Force (N)**		
0 mm (No Gap)	8.87	7.01	-12.3
8 mm (Optimal Gap)	8.87	7.01	-12.3

Table 20 contains the strain measurements at the fracture site for a 0 mm gap and 8 mm gap. The strain had an 82% reduction from 951 microstrain at no gap to 169 microstrain at an 8 mm gap. The strain measurements from the axial compressive test (Section 4.3.2) indicate that the force was dampened to a 100 - 150 N range. However, we were unable to determine the accuracy of these results due to the unrepeatability of the test.

Table 20: Strain gauge results at 472 N force for no gap and optimal gap

Gap Size (mm)	**microStrain**
0 mm (No Gap)	951
8 mm (Optimal Gap)	169

Chapter 5: Conclusion and Recommendations

Fracture healing takes an extended period of time to heal and typically requires an invasive procedure to completely heal the bone. Research has shown that small, controlled strain applied to the callus at the fracture site can reduce the amount of time needed to heal the break. The group designed a non-invasive stress application device to be used to quicken the healing process.

This device was constructed as a combination of two brace devices currently on the market, AirCast walking boot and PTB brace. If the combination device was to be manufactured as a product it would be identified by the FDA as a limb orthosis, which are Class I devices exempt from premarket notification (Food and Drugs, 2015). To apply our proof of concept to a manufactural device, we recommend assessing the design to reduce the bulkiness and eliminate unnecessary Velcro. The AirCast back component should be lengthened to reach the back of the knee and replace the popliteal component added in our design. Additionally, the amount of straps securing the devices could be consolidated or replaced with wider straps. However, this concept of a gap beneath the heel can be applied to a different device design to promote optimal healing at the fracture site.

A three step evaluation process was used to prove that the device would successfully reduce the strain at a fracture site. The analogue bones were first tested to determine their Young's modulus; the broken bones were then put back together with a small callus made of polyurethane foam. The strains at the fracture sites for varying forces were determined through an axial compressive test on the bones. The device was then tested to determine the forces experienced on different parts of the foot while in the device. The group was limited in our

inability to test the device on bone analogues with mechanical properties of real bone or an actual tibia fracture. For further testing, we recommend testing on an analogue with stronger materials as an alternative to real bone. Then, the testing should progress to actual bone, animal or human, before potential in-vivo testing with a cadaver or human subject with a tibia fracture. Additionally, we would recommend looking at the impact of bending stress on the strain by testing with strain gauges located on either side of the bone at the fracture site. This would allow more precise measurements of strain application at the fracture site and a better understanding of the devices ability to induce healing conditions.

As seen in the results the group tested a variety of gap sizes across different boot and insole designs. The best designs contained 6 mm, 8 mm, and 1 cm gaps with no padding underneath the foot. These configurations provided the greatest reduction of force transmission through the tibia, while still allowing relatively easy and natural walking. The group determined the 8 mm gap size to be the ideal gap size for the device. The device was able to dampen the ground reaction force down to a force that created a strain value conducive to bone fracture healing. The group conducted a barefoot control test which yielded a 1700 N force and 7250 microstrain at the tibia, and the device combined with the ideal 8 mm gap dampened the force down to 516 N with a 2320 microstrain at the tibia. This demonstrates that our device can provide about a 70% reduction in force transmission through the tibia and strain at fracture site, while still allowing limited mobility.

Work Cited

AO Foundation. (2014). *AO/OTA fracture and dislocation classification.* [Brochure]. Switzerland: Author.

Alimerzaloo, F., Kashani, R. V., Saeedi, H., Farzi, M., & Fallahian, N. (2013). Patellar tendon bearing brace: Combined effect of heel clearance and ankle status on foot plantar pressure. *Prosthetics and orthotics international*, 0309364613486916.

Ardatov, N. (2006, July 14). bone. Retrieved January 19, 2016, from http://www.3dcontentcentral.com/download-model.aspx?catalogid=171

Beltsios, M., Savvidou, O., Kovanis, J., Alexandropoulos, P., & Papagelopoulos, P. (2009). External fixation as a primary and definitive treatment for tibial diaphyseal fractures. *Strategies in Trauma and Limb Reconstruction*, *4*(2), 81–87.

Bizzarro, J., & Regazzoni, P. (n.d.). Principles of Fracture Fixation. Retrieved October 8, 2015, from 4 Principles of fracture fixation_Handout (1).pdf

Bono, C. M., & Einhorn, T. A. (2005). Overview of osteoporosis: pathophysiology and determinants of bone strength. In *The Aging Spine* (pp. 8-14). Springer Berlin Heidelberg.

Bouxsein, M. L. (2003). Bone quality: where do we go from here?. *Osteoporosis international*, *14*(5), 118-127.

Broken Leg in Depth AKA: Tibia & Fibula Fracture. (n.d.). Retrieved October 15, 2015.

Brophy, R. (2011). Effect of Short-Duration Low-Magnitude Cyclic Loading Versus Immobilization on Tendon-Bone Healing After ACL Reconstruction in a Rat Model. *The Journal of Bone and Joint Surgery (American) J Bone Joint Surg Am*, 381-381.

Chapter 6: Bones and Skeletal Tissues. (n.d.). Reteived September 5, 2015, from http://classes.midlandstech.edu/carterp/Courses/bio210/chap06/lecture1.html

Cherian, J. J., Bhave, A., Kapadia, B. H., Starr, R., McElroy, M. J., & Mont, M. A. (2015). Strength and Functional Improvement Using Pneumatic Brace with Extension Assist for End-Stage Knee Osteoarthritis: A Prospective, Randomized trial. *The Journal of arthroplasty*, *30*(5), 747-753.

Claes, L. E., Heigele, C. A., Neidlinger-Wilke, C., Kaspar, D., Seidl, W., Margevicius, K. J., & Augat, P. (1998). Effects of mechanical factors on the fracture healing process. *Clinical orthopaedics and related research*, *355*, S132-S147.

De Leva, P. (1996). Adjustments to Zatsiorsky-Seluyanov's segment inertia parameters. *Journal of biomechanics*, *29*(9), 1223-1230.

Demmer, P. (2012, May 5). Fracture management with limited resources (C. Colton, Ed.). Retrieved October 11, 2015.

Doblaré, M., Garcıa, J. M., & Gómez, M. J. (2004). Modelling bone tissue fracture and healing: a review. *Engineering Fracture Mechanics*, *71*(13), 1809-1840.

Egol, K. A., Kubiak, E. N., Fulkerson, E., Kummer, F. J., & Koval, K. J. (2004). Biomechanics of locked plates and screws. *Journal of orthopaedic trauma*, *18*(8), 488-493.

FlexiForce A401 Sensor. (2014, November 13). Retrieved December 10, 2015, from https://www.tekscan.com/products-solutions/force-sensors/a401

Food and Drugs, 21 C.F.R. pt. 1 (2015).

Fragomen, A. T., & Rozbruch, S. R. (2007). The mechanics of external fixation. *HSS Journal*, *3*(1), 13-29.

Fritton, S. P., McLeod, K. J., & Rubin, C. T. (2000). Quantifying the strain history of bone: spatial uniformity and self-similarity of low-magnitude strains. *Journal of biomechanics*, *33*(3), 317-325.

Game Changers: Stats, Stories and What Communities Are Doing to Protect Young Athletes. (2013, August 1). Retrieved September 7, 2015.

Gillet, P., & Cescotto, S. (n.d.). *Mechanics of bones*. Lecture.

González-Torres, L. A., Gómez-Benito, M. J., Doblaré, M., & García-Aznar, J. M. (2010). Influence of the frequency of the external mechanical stimulus on bone healing: a computational study. *Medical engineering & physics*, *32*(4), 363-371.

Hayda, R. (2008). *Principles of External Fixation* [PowerPoint slides]. Retrieved from http://ota.org/media/29260/G11-Ex-Fix-Principles-JTG-rev-2-4-10.ppt

Joslin, C. C., Eastaugh-Waring, S. J., Hardy, J. R. W., & Cunningham, J. L. (2008). Weight bearing after tibial fracture as a guide to healing. *Clinical biomechanics*, *23*(3), 329-333.

Kenwright, J., Richardson, J. B., Cunningham, J. L., White, S. H., Goodship, A. E., Adams, M. A., Magnussen, P. A. & Newman, J. H. (1991). Axial movement and tibial fractures. A controlled randomised trial of treatment. *Journal of Bone & Joint Surgery, British Volume*, 73(4), 654-659.

Khodadadyan-Klostermann, C., Seebach, M., Taylor, W., Duda, G., & Haas, N. (2004). Distribution of bone mineral density with age and gender in the proximal tibia. *Clinical Biomechanics*, *19*(4), 370-376.

Lassus, J., Tulikoura, I., Konttinen, Y. T., Salo, J., & Santavirta, S. (2002). Bone stress injuries of the lower extremity. *Acta Orthopaedica*, 73(3), 359-368.

Mallik, A. R., Covall, D. J., & Whitelaw, G. P. (1992). Internal versus external fixation of bicondylar tibial plateau fractures. *Orthopaedic Review*, 21(12), 1433-1436.

Malunion and Nonunion of Fracture. (n.d.). Retrieved September 5, 2015 from http://www.mdguidelines.com/malunion-and-nonunion-of-fracture

Marsh, D. R., & Li, G. (1999). The biology of fracture healing: optimizing outcome. *British medical bulletin*, *55*(4), 856-869.

Matheson, G., Clement, D., Mckenzie, D., Taunton, J., Lloyd-Smith, D., & Macintyre, J. (1987). Stress fractures in athletes: A study of 320 cases. *The American Journal of Sports Medicine*.

Mavčič, B., & Antolič, V. (2012). Optimal mechanical environment of the healing bone fracture/osteotomy. *International Orthopaedics (SICOT)*, *36*(4), 689-695.

Milgrom, C., Gildadi, M., Simkin, A., Rand, N., Kedem, R., Kashtan, H., ... & Gomori, M. (1989). The area moment of inertia of the tibia: a risk factor for stress fractures. *Journal of biomechanics*, *22*(11-12), 1243-1248.

National Hospital Ambulatory Medical Care Survey: 2010 Emergency Department Summary Tables. (2010). Retrieved October 12, 2015, from http://www.cdc.gov/nchs/data/ahcd/nhamcs_emergency/2010_ed_web_tables.pdf

Nieves, J., Formica, C., Ruffing, J., Zion, M., Garrett, P., Lindsay, R., & Cosman, F. (2004). Males Have Larger Skeletal Size and Bone Mass Than Females, Despite Comparable Body Size. *J Bone Miner Res Journal of Bone and Mineral Research, 20*(3), 529-535.

Nigg, B. M., & Herzog, W. (Eds.). (2007). *Biomechanics of the musculo-skeletal system*. Wiley.

Nunamaker, D. M., Rhinelander, F. W., & Heppenstall, R. B. (1985). Delayed union, nonunion, and malunion. *Textbook of Small Animal Orthopaedics. Philadelphia, PA, Lippincott*, 511-518.

Nyary, T., & Scammell, B. E. (2015). Principles of bone and joint injuries and their healing. Surgery (Oxford), 33(1), 7-14.

Procedure for Making a Silicone Molds. (1997). Retrieved October 13, 2015, from http://www.cs.cmu.edu/~rapidproto/manufacturing/molds/silicone.html

Roshian-Ghias, A., Terrier, A., Bourban, P., & Pioletti, D. (2010). In Vivo cyclic loading as a potent stimulatory signal for bone formation inside tissue engineering scaffolds. *European Cells and Materials, 19*, 41-49.

Sarmiento, A., Gersten, L., Sobol, P., Shankwiler, J., & Vangsness, C. (1989). Tibial Shaft Fractures Treated With Functional Braces: Experience with 780 fractures. *The Bone and Joint Journal*, *71-B*(4), 602-609.

Sarmiento, A., & Latta, L. L. (1999). Functional fracture bracing. *Journal of the American Academy of Orthopaedic Surgeons*, *7*(1), 66-75.

Schiessl, H., Willnecker, J., & Niemeyer, G. T. (1999). Muscle cross sectional area and bone cross sectional area in the human lower leg measured with peripheral computed tomography. *Musculoskeletal interactions*, *2*, 47-52.

Seeley, R., Stephens, T., & Tate, P. (2006). *Anatomy & Physiology* (7th ed.). Dubuque, IA: McGraw-Hill.

Strain Gage Selection: Criteria, Procedures, Recommendations. (2014). Retrieved October 14, 2015, from http://www.vishaypg.com/docs/11055/tn505.pdf

Systems Theory and Automatic Control. (n.d.). Retrieved September 5, 2015 from http://ifatwww.et.uni-magdeburg.de/syst/systembio/research

Tanaha, H. Nagata, K. Goto, T Hoshiko., H & Inoue, A. (1999). The effect of the patellar tendon-bearing cast on loading. *The Journal of Bone and Joint surgery*, 228-232.

Tibia. (2015). Retrieved September 7, 2015, from http://www.britannica.com/science/tibia

Tibia (Shinbone) Shaft Fractures. (2013). Retrieved September 7, 2015, from http://orthoinfo.aaos.org/topic.cfm?topic=A00522

Toivanen, J., Honkonen, S., Koivisto, A., & Järvinen, M. (2001). Treatment of low-energy tibial shaft fractures: Plaster cast compared with intramedullary nailing. *International Orthopaedics (SICOT) International Orthopaedics,* 110-113.

Turner, C. H. (1998). Three rules for bone adaptation to mechanical stimuli. *Bone*, *23*(5), 399-407.

Umberger, B. R., & Martin, P. E. (2007). Mechanical power and efficiency of level walking with different stride rates. *Journal of Experimental Biology*, 210(18), 3255-3265.

Vicenti, G., Pesce, V., Tartaglia, N., Abate, A., Mori, C. M., & Moretti, B. (2014). Micromotion in the fracture healing of closed distal metaphyseal tibial fractures: A multicentre prospective study. *Injury*, *45*, S27-S35.

Vijayakumar, V., Marks, L., Bremmer-Smith, A., Hardy, J., & Gardner, T. (2006). Load transmission through a healing tibial fracture. *Clinical Biomechanics*, *21*(1), 49-53.

Whedon, G. (2014). Physiology of bone. Retrieved October 3, 2015, from http://www.britannica.com/science/bone-anatomy/Physiology-of-bone

Willems, N. M., Langenbach, G. E., Everts, V., & Zentner, A. (2014). The microstructural and biomechanical development of the condylar bone: a review. *The European Journal of Orthodontics*, *36*(4), 479-485.

Winter, D. A. (1991). *Biomechanics and motor control of human gait: Normal, elderly, and pathological.* Waterloo, Ont.: University of Waterloo Press.

Winter, D. (2009). *Biomechanics and motor control of human movement* (4th ed.). Hoboken, N.J.: Wiley.

Appendix A: Design Matrix Categories

The descriptions of the design matrix categories are as follows:

Cost: 1 corresponds to a high cost and 5 corresponds to a low cost to build the prototype

Force Control: 1 corresponds to no control over the magnitude of the force applied and 5 corresponds to complete control over the force applied

Adjustable to Patient: 1 corresponds to a device that is the same for everyone and 5 corresponds to a device that can be customizable to a person

Manufacturability: 1 corresponds to a complex construction of the device and 5 corresponds to a simple construction

Strain Rate Control: 1 corresponds to no control over the strain rate and 5 corresponds to complete control over the strain rate

Time to Implementation: 1 corresponds to an implementation at the end of the healing process and 5 corresponds to immediate implementation after injury

User Experience: 1 corresponds to a high maintenance device and 5 corresponds to little maintenance needed for the device

Mobility: 1 corresponds to no movement while wearing the device and 5 corresponds to regular daily activity while wearing the device

Invasive: 1 corresponds to a device that would require a surgery to implant the device and 5 corresponds to a device that is completely outside the body.

Appendix B: Bone Por-a-Mold Procedure

Materials:

2ft PVC Pipe, ~4” diameter

1 PVC End-Caps

Por-a-Mold (2 part silicone mixture)

Duct tape for external mold halves

Nails to fixate bone within the PVC tube

Procedure:

1. Prep Foam Tibia Bone:
    a. Spray outer surface with clear spray paint to seal surface
    b. Fill center canal with hot glue

2. Preparing PVC Pipe and Cape:
    a. Cut PVC pipe in half on long axis
    b. Drill a pilot hole in the PVC end-cap
    c. Force a nail with slightly larger diameter than pilot hole through the end cap

d. Attach the PVC end cap to the PVC tube halves

e. Secure the 2 PVC tube halves together with duct tape and hot glue to seal holes

f. Use nails and holes found in the tibia model to hold it in place inside PVC pipe

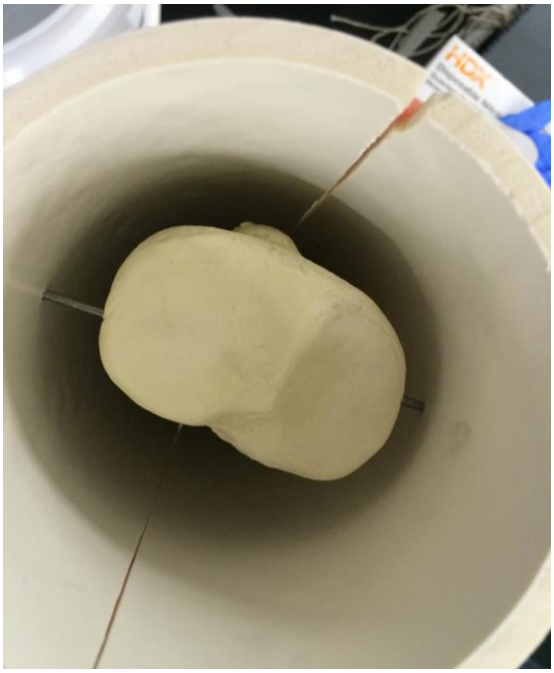

g. Seal remaining holes with duct tape and glue around the nails and bottom end-cap to ensure a water-tight bond

3. Mix Por-a-Mold (according to instructions)
    a. Pour a 1:1 ratio of each part of the Por-a-Mold

b. Mix components together within the working time of Por-a-Mold


c. Pour mixture into the PVC pipe until it is above the top of the tibia model


4. Remove Mold From PVC Pipe:
    a. Allow mold to cure in vertical position for required cure time

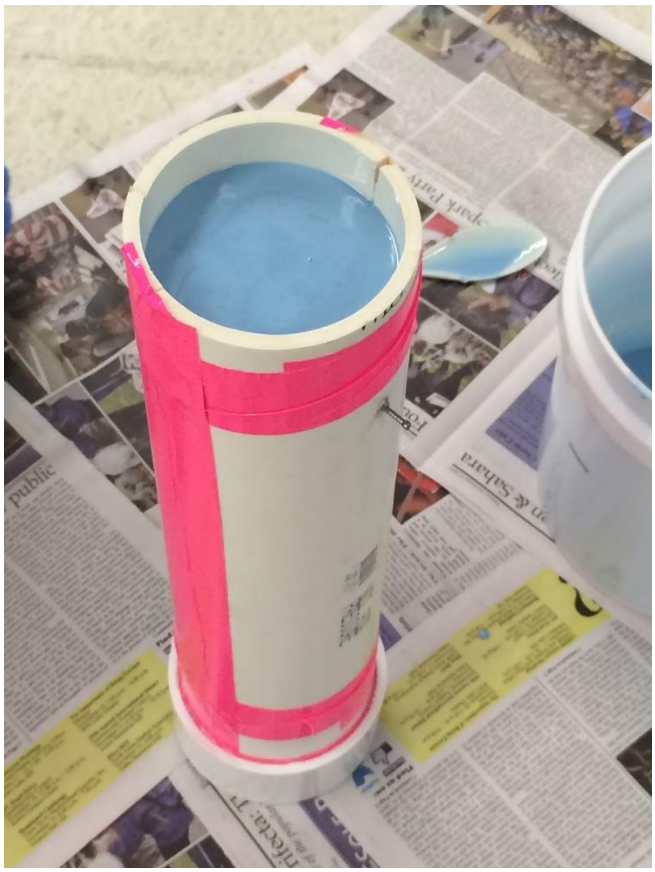

b. Remove silicone mold from PVC pipe by carefully removing bottom end cap, then undo duct tape around the PVC pipe halves, and pull them apart freeing mold
c. Use a hand saw to carefully cut the silicon mold in half avoiding the tibia model
d. Pry mold halves apart and remove tibia model
e. Examine the mold cavity to determine if it is acceptable to create a bone analogue

Appendix C: Additional ANSYS Analysis

Unbroken Cylinder Model (SawBone)

Total Deformation:

$$\delta = \frac{FL}{EA}$$

$$A = \pi(r_o^2 - r_i^2) = \pi((12.7\ \text{mm})^2 - (5\ \text{mm})^2) = 428.2\ \text{mm}^2$$

$$\delta = \frac{(400\ \text{N}) * (380\ \text{mm})}{(1{,}500\ \text{MPa}) * (428.2\ \text{mm}^2)}$$

$$\delta = 0.237\ \text{mm}$$

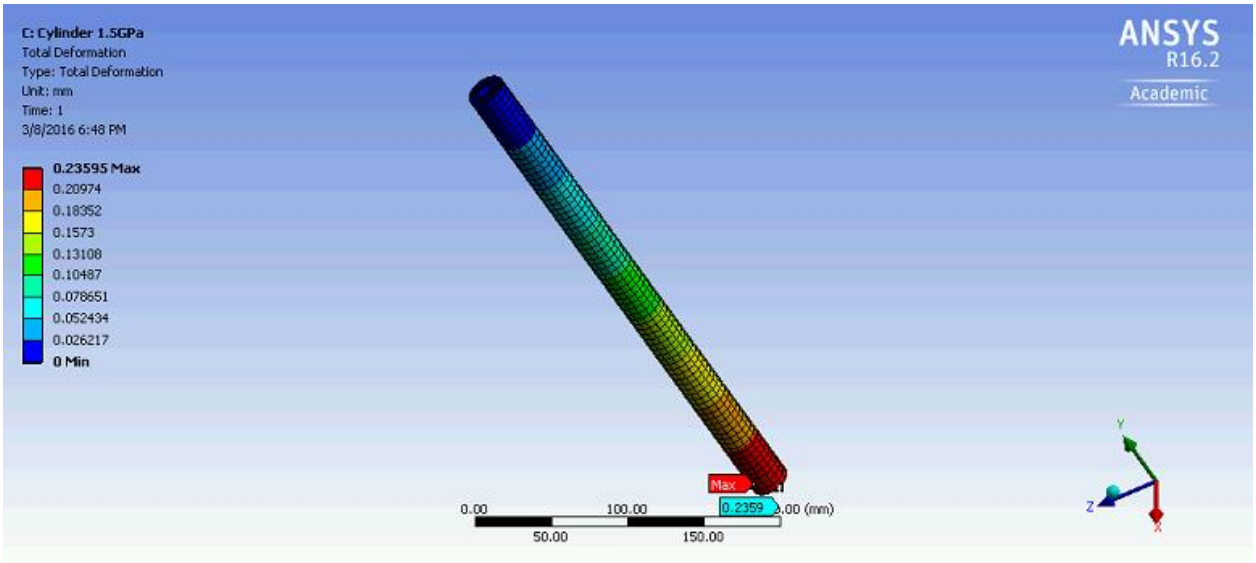

Normal Stress:

$$\sigma = \frac{F}{A}$$

$$\sigma = \frac{-400\ \text{N}}{428.2\ \text{mm}^2}$$

$$\sigma = -0.93\ \text{MPa}$$

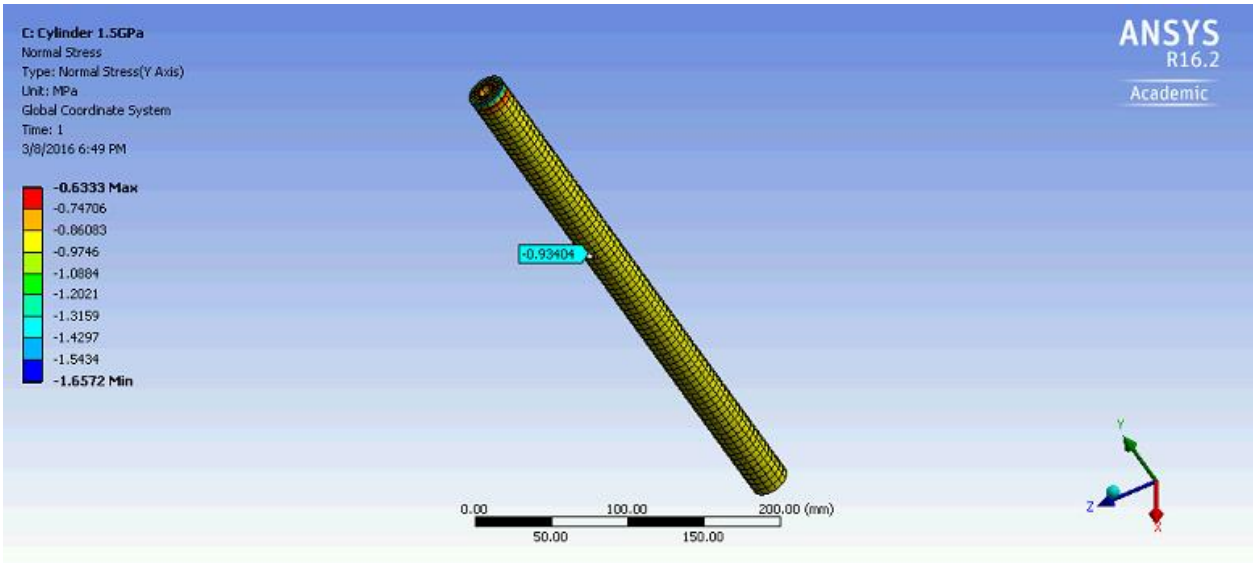

Nodal Force:

Additionally, the SawBone model was analyzed with a 400 N compressive nodal force to simulate a point load, as seen in the figure below.

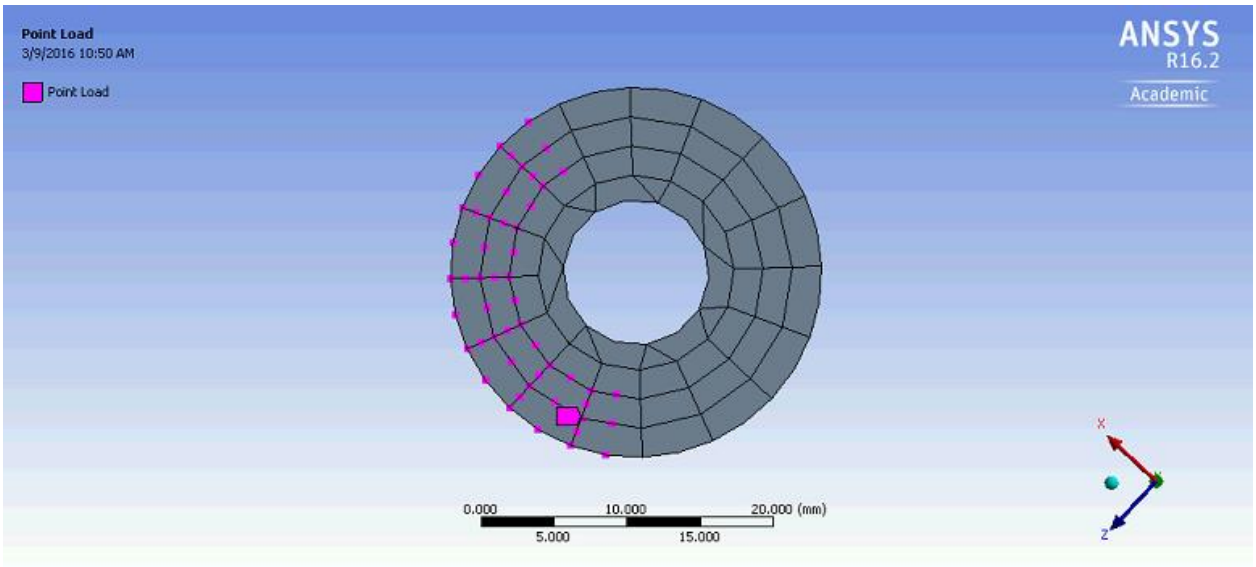

It had a maximum total deformation of 7.83 mm, a normal stress range of 1.26 MPa to -6.38 MPa and a strain range of 0.000754 mm/mm to -0.00424 mm/mm.

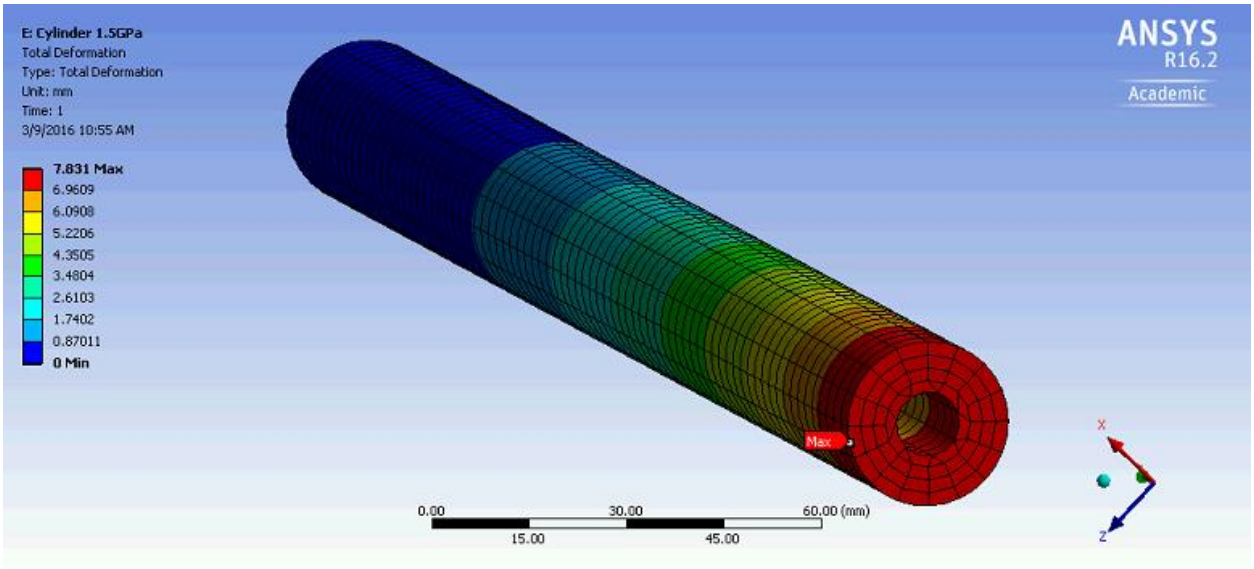
E: Cylinder 1.5GPa
Total Deformation
Type: Total Deformation
Unit: mm
Time: 1
3/9/2016 10:55 AM
7.831 Max
6.9609
6.0908
5.2206
4.3505
3.4804
2.6103
1.7402
0.87011
0 Min
ANSYS
R16.2
Academic
Max
0.00
30.00
60.00 (mm)
15.00
45.00
X
Z

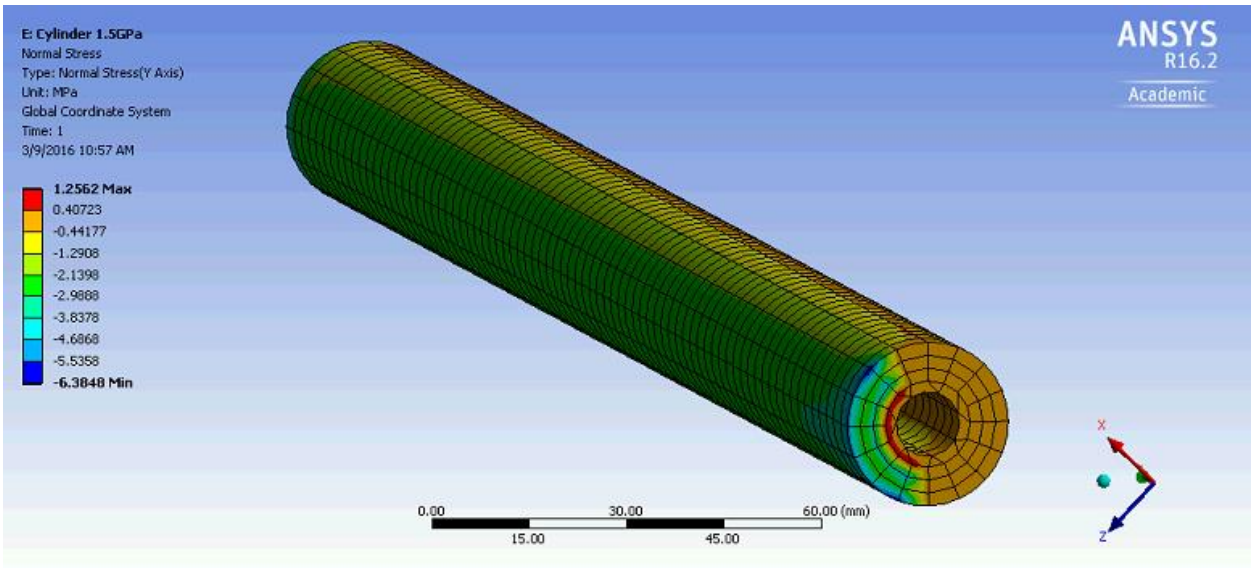
E: Cylinder 1.5GPa
Normal Stress
Type: Normal Stress(Y Axis)
Unit: MPa
Global Coordinate System
Time: 1
3/9/2016 10:57 AM
1.2562 Max
0.40723
-0.44177
-1.2908
-2.1398
-2.9888
-3.8378
-4.6868
-5.5358
-6.3848 Min
ANSYS
R16.2
Academic
0.00
30.00
60.00 (mm)
15.00
45.00
X
Z

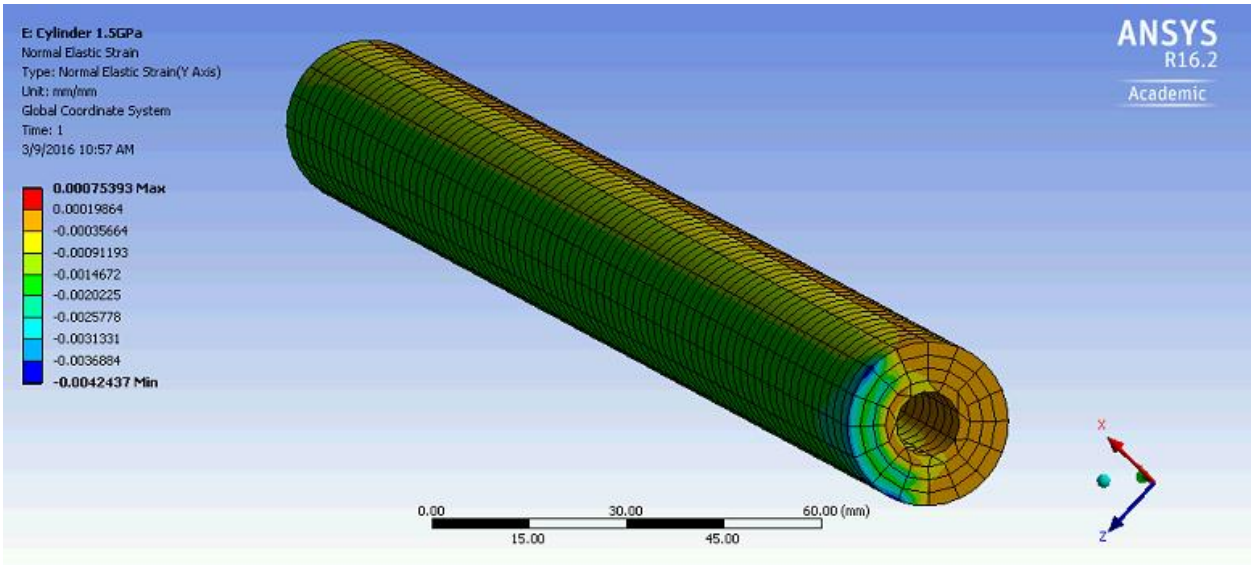
E: Cylinder 1.5GPa
Normal Elastic Strain
Type: Normal Elastic Strain(Y Axis)
Unit: mm/mm
Global Coordinate System
Time: 1
3/9/2016 10:57 AM
0.00075393 Max
0.00019864
-0.00035664
-0.00091193
-0.0014672
-0.0020225
-0.0025778
-0.0031331
-0.0036884
-0.0042437 Min
ANSYS
R16.2
Academic
0.00
30.00
60.00 (mm)
15.00
45.00
X
Z

Broken Cylinder Model

The stresses and strains found in the callus for the 400 N compressive load applied to the entire bottom face can be seen below.

	Cortical Bone (10 GPa)
Callus Strains	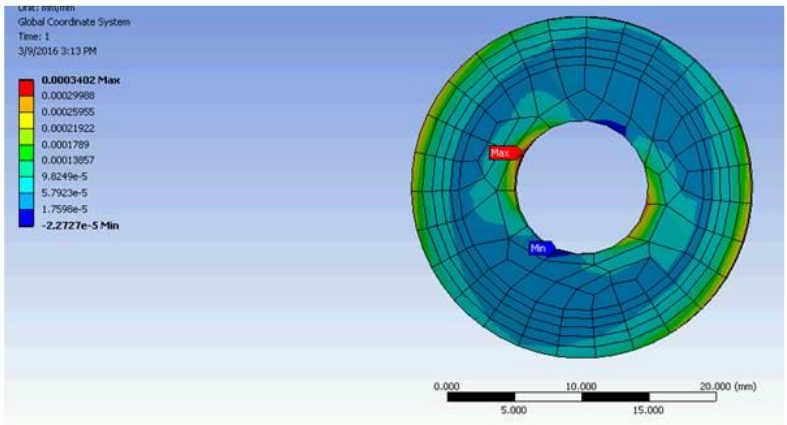
Callus Stresses	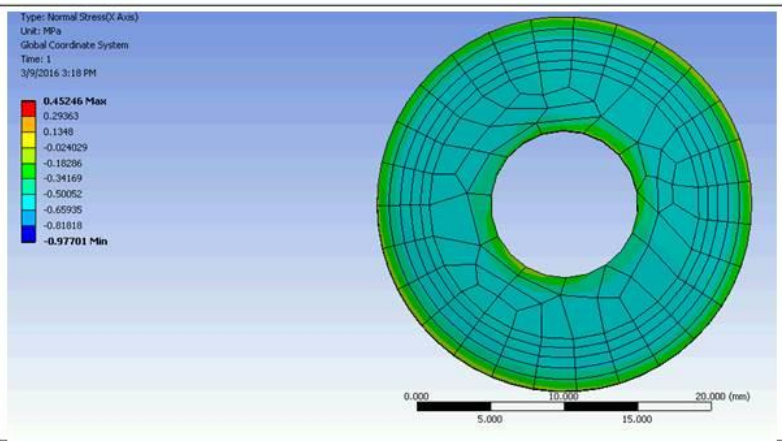

	SawBone (1.5 GPa)
Callus Strains	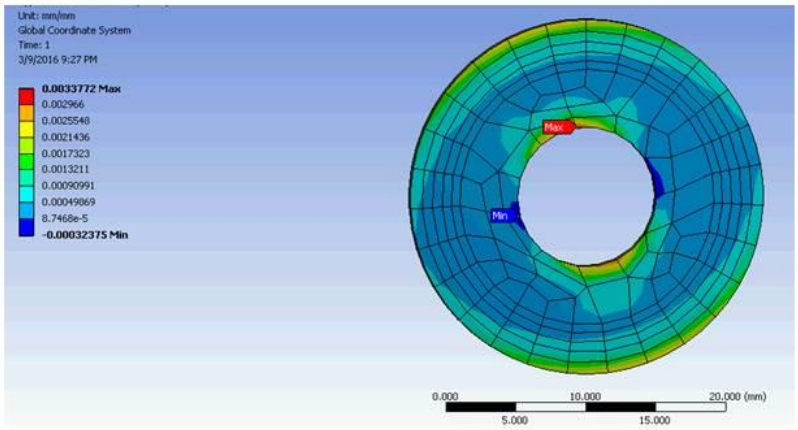
Callus Stresses	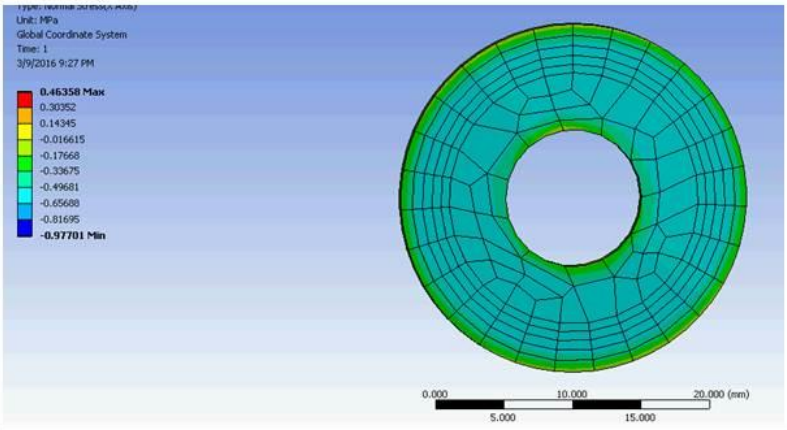

	Polyurethane (0.4 GPa)
Callus Strains	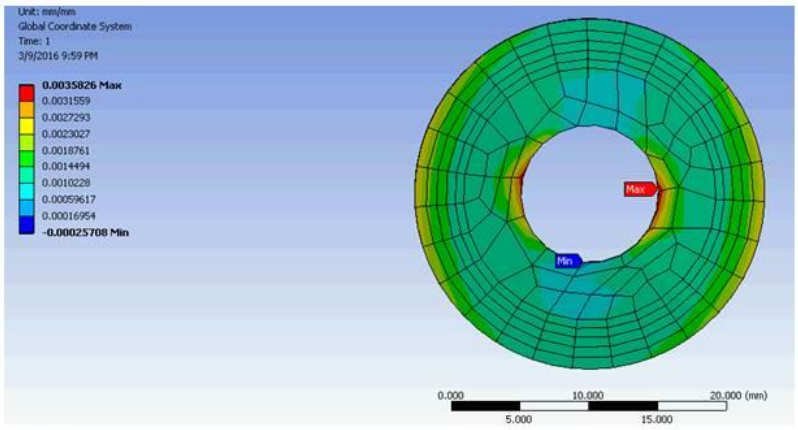
Callus Stresses	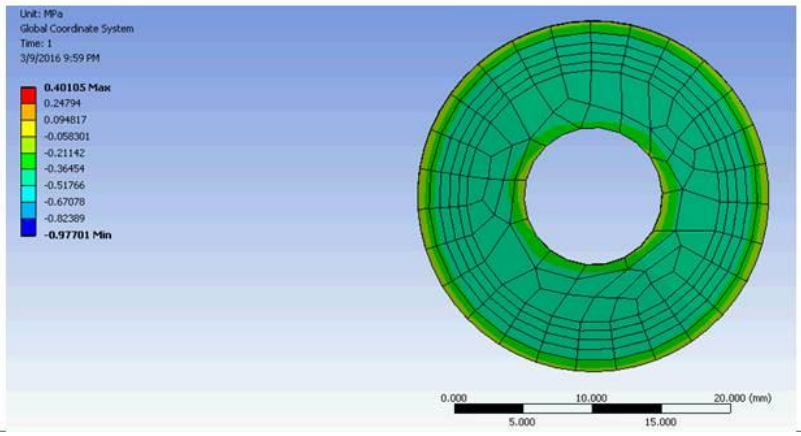

The maximum and minimum strain values were all found in the callus, while the maximum compressive stresses were found in different parts of the bone. The maximum stresses occur in the bone directly adjacent to the callus, while the minimum stresses occur at the fixed support.

Nodal Force:

The same simulations were run on the cylinder model using a 400 N compressive force applied to half of the bottom face of the cylinder.

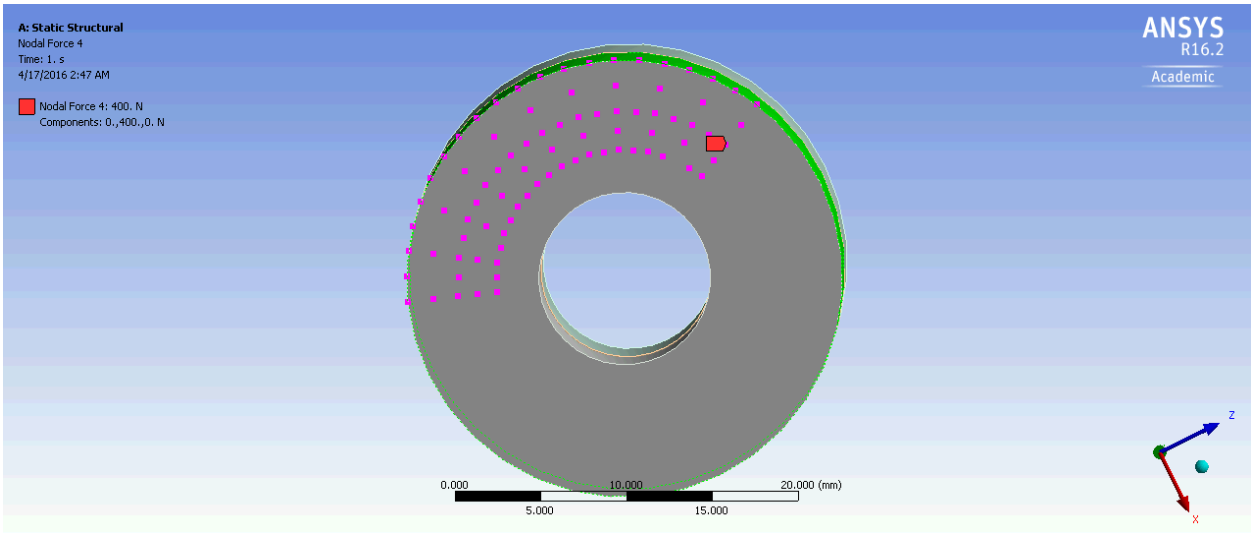

The resulting deformation, normal stress, and strain for each type of bone material, can be seen in the table below.

	Cortical Bone	**SawBone**	**Polyurethane Bone**
Deformation (mm)	1.02	7.31	25.2
Normal Stress (MPa)	-2.36	-2.36	-2.36
Strain (mm/mm)	-0.00033	-0.00328	-0.00342

As in the previous model, the maximum strains were found in the callus of the material and can be seen for each type of bone in the figures below.

	Cortical Bone (10 GPa)
Callus Strains	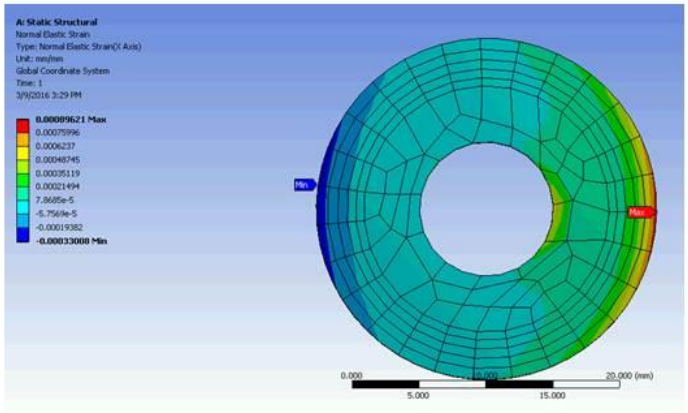
Callus Stresses	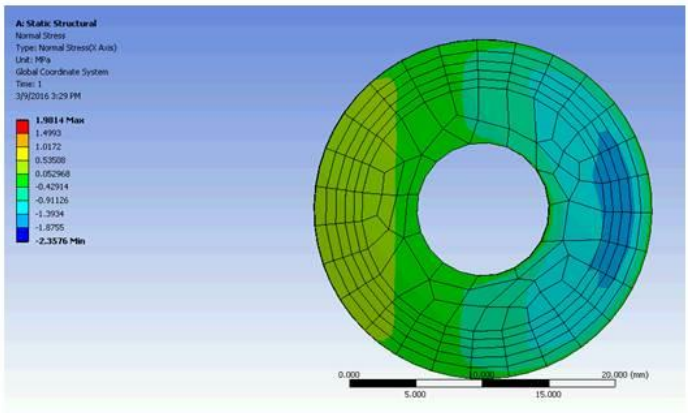

	SawBone (1.5 GPa)
Callus Strains	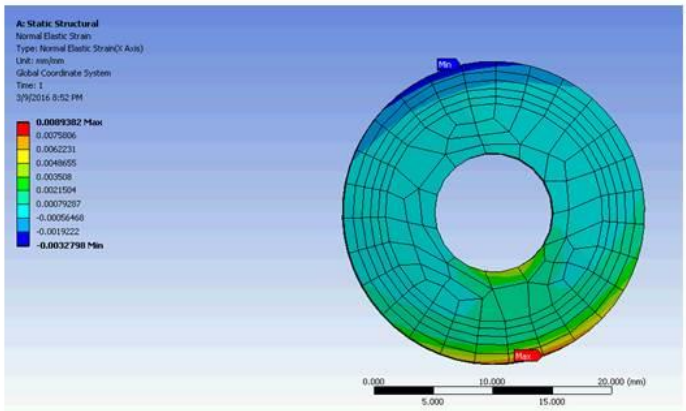
Callus Stresses	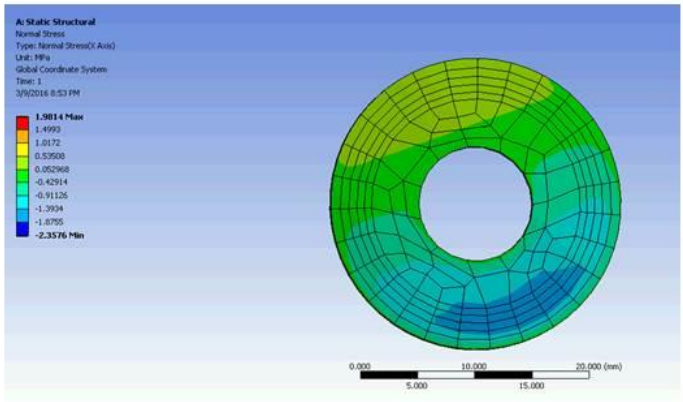

	Polyurethane (0.4 GPa)
Callus Strains	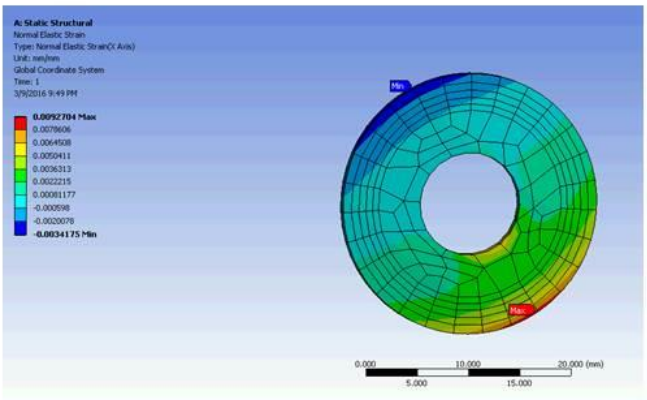
Callus Stresses	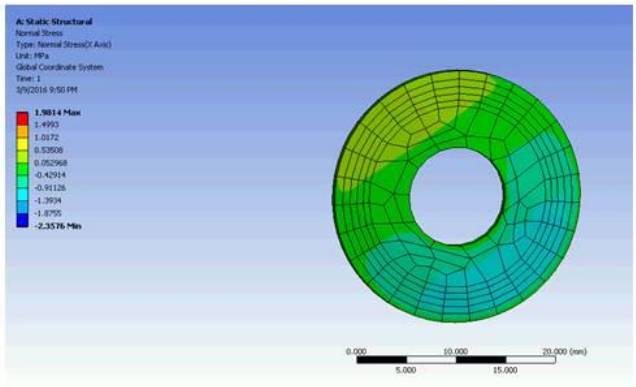

The maximum and minimum stresses were found in other locations in the cylinder model, as seen below. The maximum stress occurred at the point of the force, and the minimum occurred at the fixed support.

Unbroken Tibia Model (SawBone)

Total Deformation:

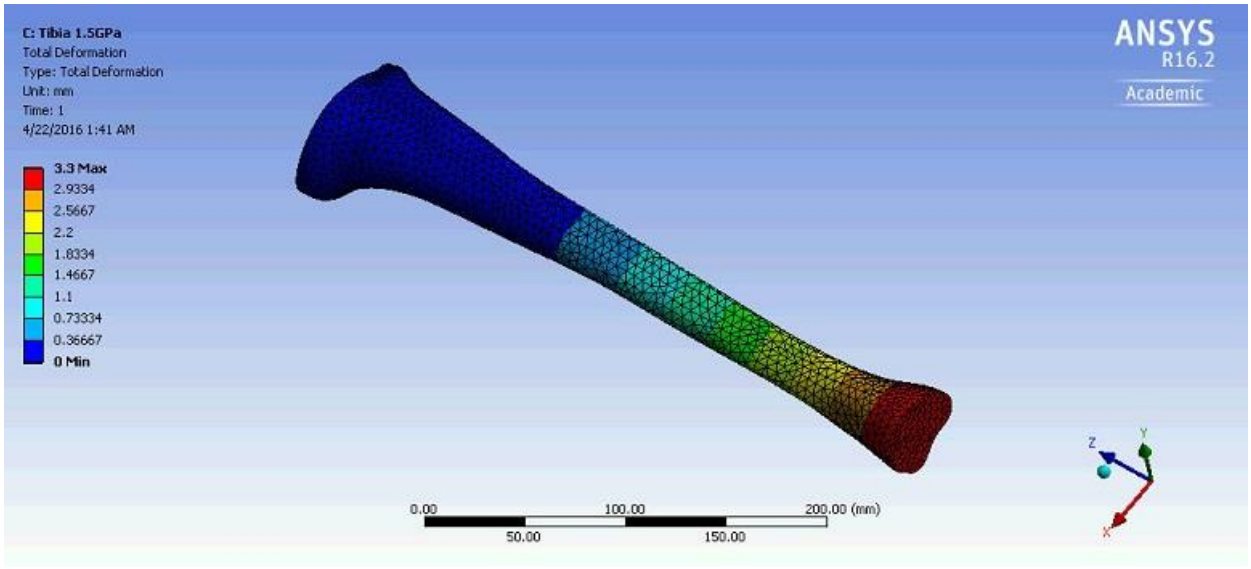

Normal Stress:

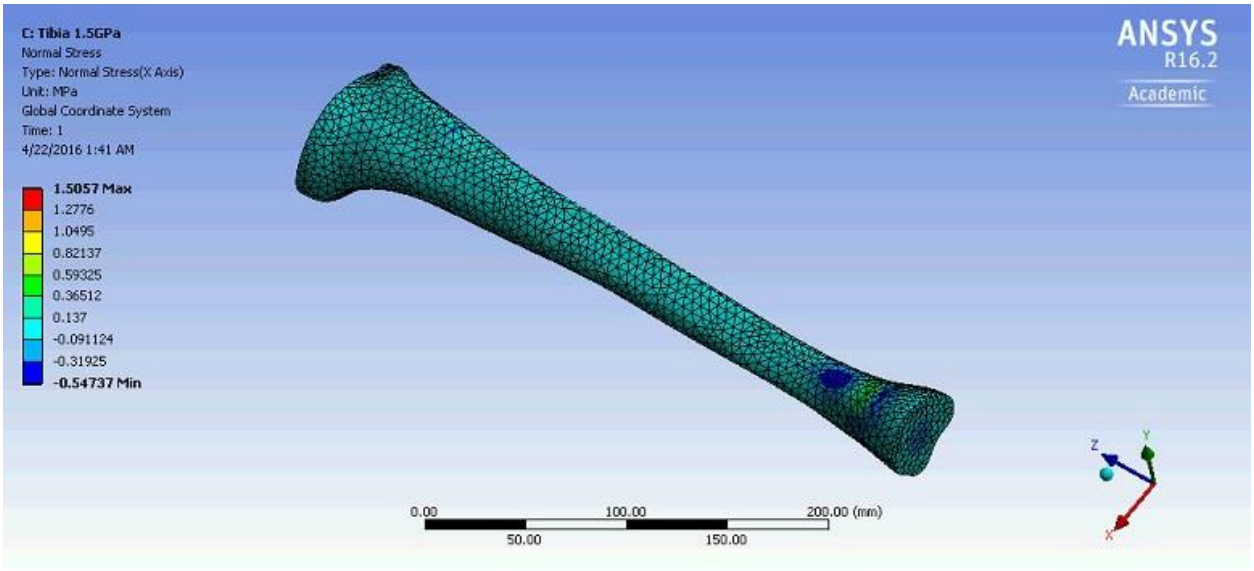

Nodal Force:

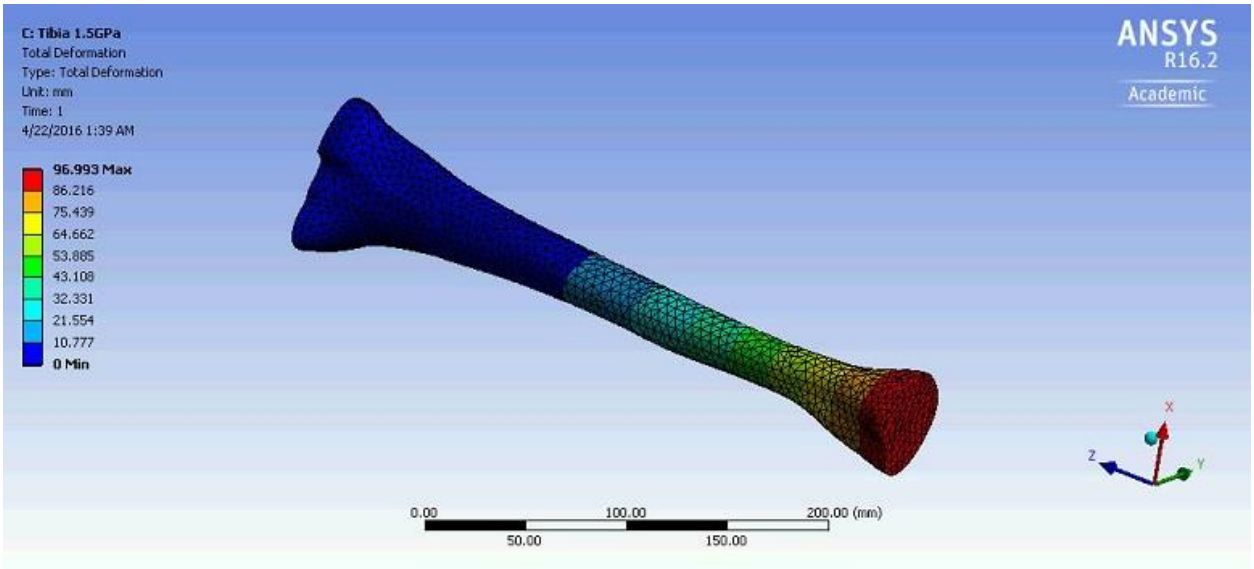

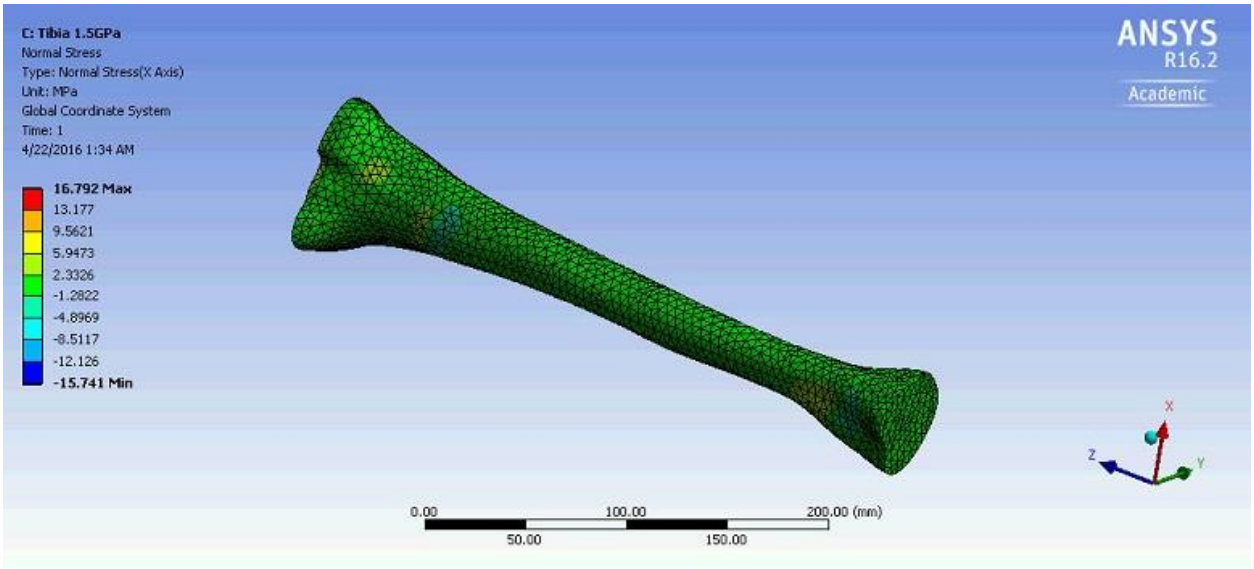

Broken Tibia Model

The stresses and strain in the calluses for the different bone materials can be seen below. The maximum and minimum strains were found in the callus in each scenario, and the largest stress from the compressive force was also found in the callus.

	Cortical Bone (10 GPa)
Callus Strains	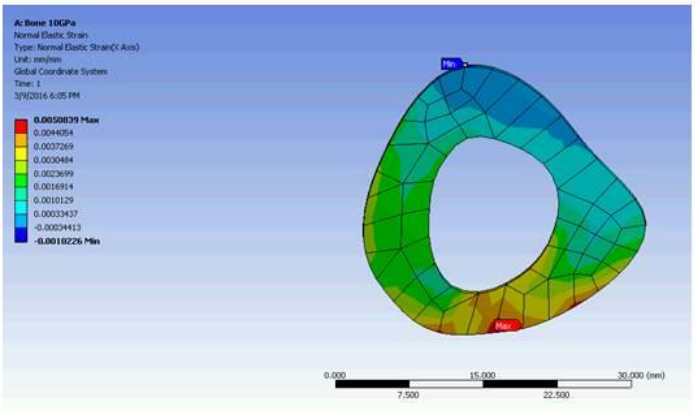
Callus Stresses	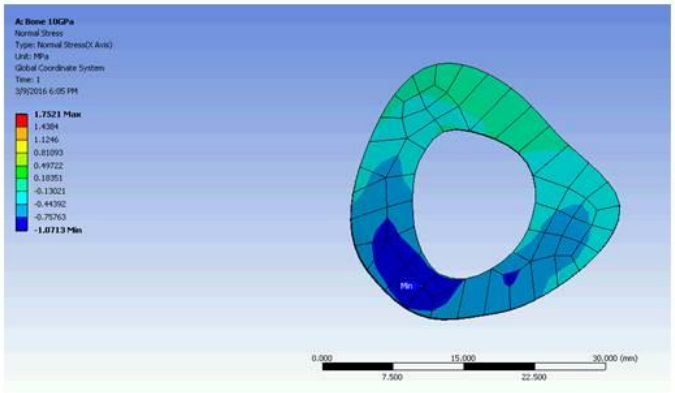

	Polyurethane (0.4 GPa)
Callus Strains	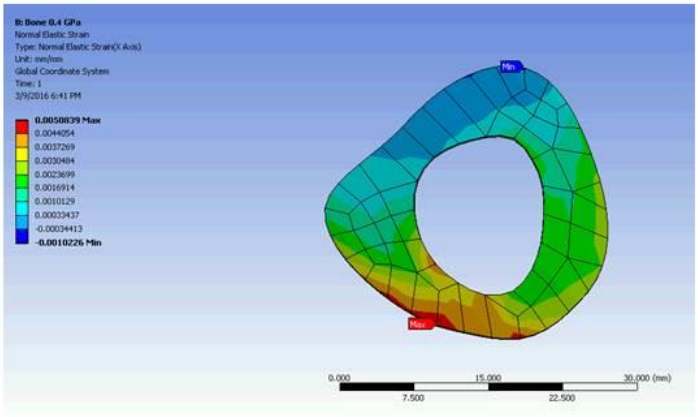
Callus Stresses	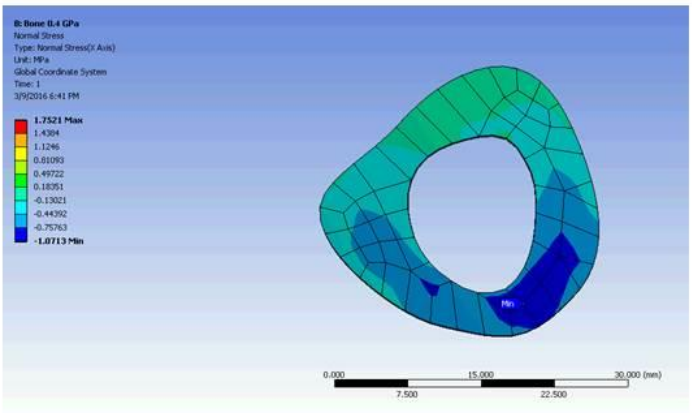

Nodal Force:

For the less than ideal condition of a nodal force applied to half of the bottom of the tibia, the normal stresses and strains for the cortical and polyurethane bone models can be seen below.

	Cortical Bone (10 GPa)
Callus Strains	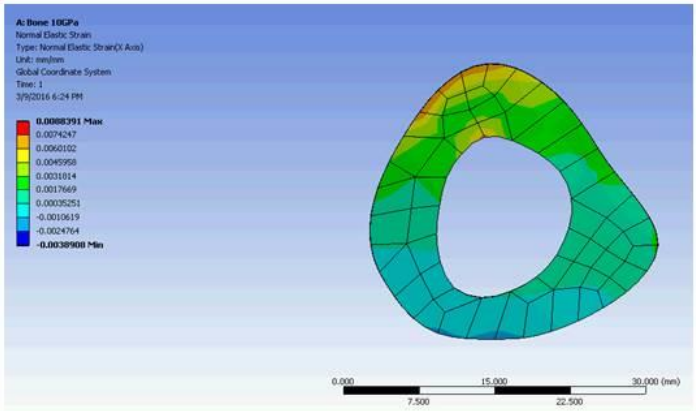
Callus Stresses	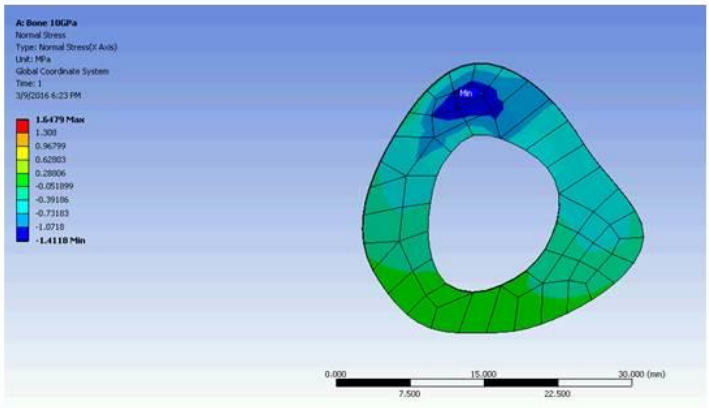

Appendix D: Accuracy & Errors

Test 1: Instron Testing Error and Accuracy

An Instron 5544 machine was used for the three-point bending tests. The Instron had a 2000 N load cell and an accuracy reading of 0.25% or 5 N. A tare load of 5 N was applied to the bones before beginning the test to increase the accuracy of the reading.

Test 2: Strain Gauge Error and Accuracy

A sample of data was recorded to determine the accuracy of the test's strain measurement versus time. A bell curve was created using the calibrated strains, the normal distribution, the average, and the standard deviation. Based on analysis of the data in Excel, the strain range was identified as 189 to 194 microstrain. This 5 microstrain of irremovable error in this range indicated about 3% error on all measurements using this system.

$$\% \text{ Error} = \frac{194 - 189}{192} * 100 = 2.7\ \% = \ \pm 3\%$$

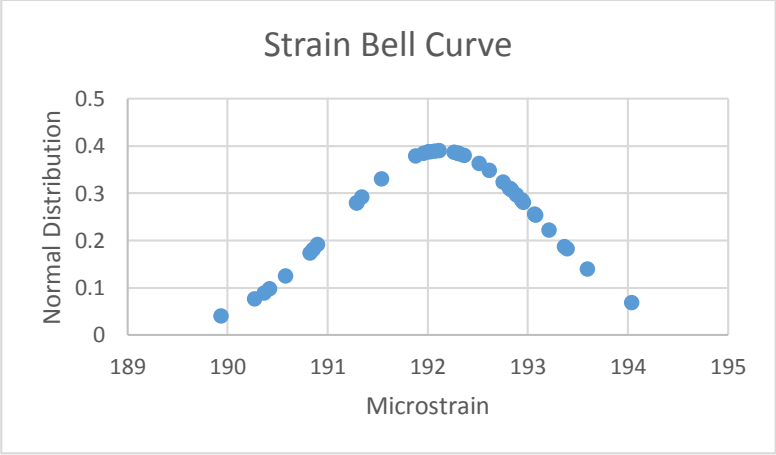

Axial Compressive Test Error Curve

Test 3: Force Sensor Error and Accuracy

In order to calculate the error margin of the force sensor test the group decided to gather data at a static load and calculate the variance of the measurements. A 5 lb weight was placed on each sensor with a 493 data points were collected during the measurement. A count graph was created, by counting how many times each number in the data set appeared. We were able see that for Force Sensor 1, 95.1% of all data lies within a certain range. We then calculated the range divided by the average and could then calculate the percent error of the measurements. The maximum error for a single sensor was ±4.7% and the minimum ±3.8% error. Figure 79 (Force Sensor 1), Figure 80 (Force Sensor 2), and Figure 81 (Force Sensor 3) illustrated how 0.0001 volt steps were used for each bins. Overall, five decimal places were deemed the limit of our DAQ box precision.

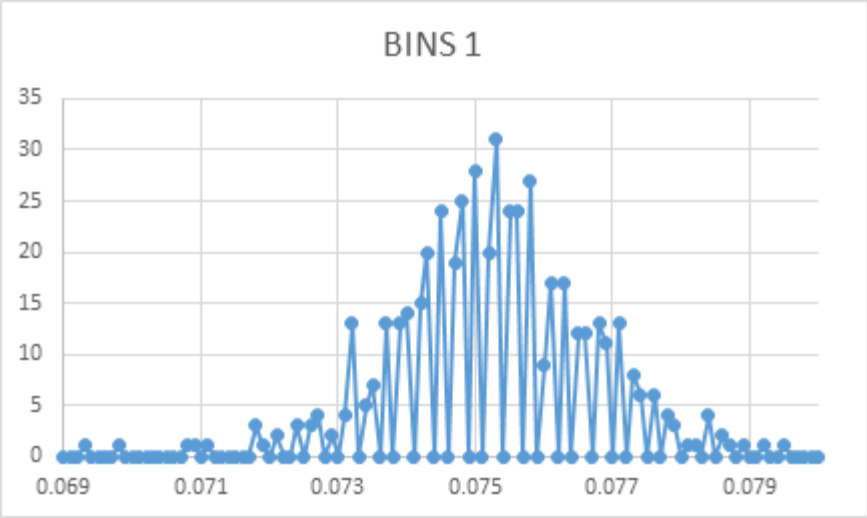

Sensor 1 with 469 points at ±4.7% error

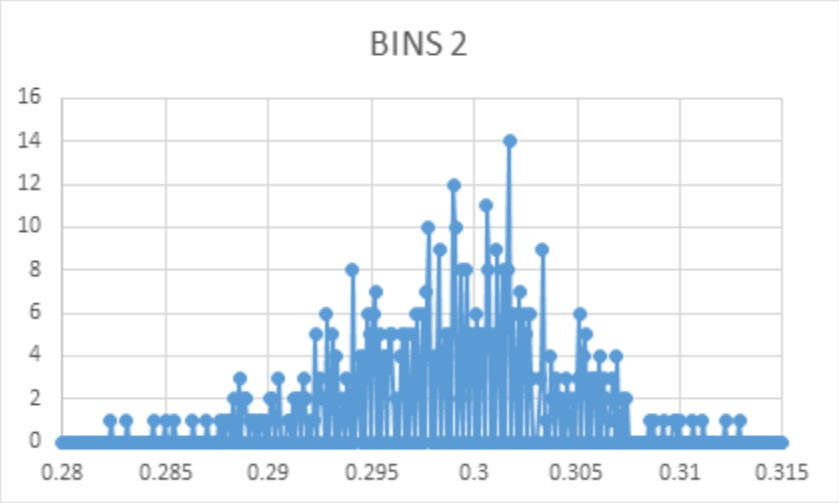

Sensor 2 with 434 points at ±4.5% error

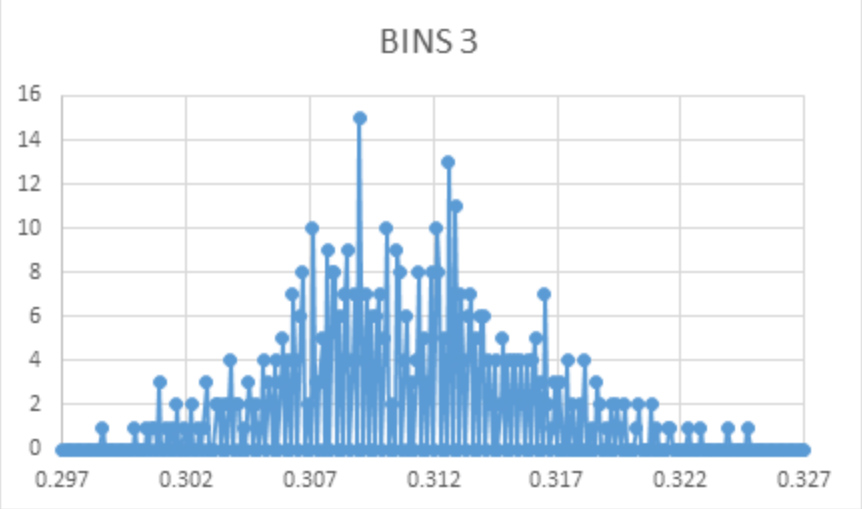

Sensor 3 with 439 points at ±3.8% error